A Comparative Study of Vortex Identification Methods on the Wall Mounted Hump Simulations Using SU2

by

Ramin TALEBAN

THESIS PRESENTED TO ÉCOLE DE TECHNOLOGIE SUPÉRIEURE
IN PARTIAL FULFILLMENT FOR A MASTER'S DEGREE
WITH THESIS IN MECHANICAL ENGINEERING
M.A.Sc.

MONTREAL, AUGUST 14, 2023

ÉCOLE DE TECHNOLOGIE SUPÉRIEURE
UNIVERSITÉ DU QUÉBEC

BOARD OF EXAMINERS

THIS THESIS HAS BEEN EVALUATED

BY THE FOLLOWING BOARD OF EXAMINERS

Mr. François Morency, Thesis supervisor
Department of Mechanical Engineering, École de Technologie Supérieure

Ms. Marlène Sanjosé, Thesis Co-Supervisor
Department of Mechanical Engineering, École de Technologie Supérieure

Mr. Patrice Seers, Chair, Board of Examiners
Department of Mechanical Engineering, École de Technologie Supérieure

Mr. Patrick Germain, Member of the Jury
Department of Mechanical Engineering, École de Technologie Supérieure

THIS THESIS WAS PRESENTED AND DEFENDED

IN THE PRESENCE OF A BOARD OF EXAMINERS AND THE PUBLIC

ON "JULY 31, 2023"

AT ÉCOLE DE TECHNOLOGIE SUPÉRIEURE

ACKNOWLEDGEMENTS

I want to start by sincerely thanking my research director Prof. François Morency and my co-director Prof. Marlène Sanjosé, for their encouragement, patience, vast expertise, enthusiasm, and continuous support during this study.

I would like to thank École de technologie supérieure and the beautiful city of Montreal for this great opportunity. I extend my sincere gratitude to the jury members who consented to review this work, in addition to my research director and co-director.

Additionally, I would like to thank the Digital Research Alliance of Canada (formerly Compute Canada) for providing the materials and computational resources for the simulations. I also want to express my gratitude to the Calcul Quebec team for the excellent training and assistance during my program.

Last but not least, I want to express my gratitude to my parents, my brother, and my friends for being there for me and for helping me throughout my life and my study abroad.

Une étude comparative des méthodes d'identification des vortex sur les simulations Wall Mounted Hump à l'aide de SU2

Ramin TALEBAN

RÉSUMÉ

Au cours des deux dernières décennies, l'impact de l'accumulation de glace sur l'aérodynamique du vol a été longuement étudié. Ces recherches visent à prédire quand un avion décroche en raison de ses caractéristiques aérodynamiques modifiées par la glace. L'accrétion de glace sur une aile d'avion peut modifier le champ d'écoulement, entraînant la formation de plus de tourbillons. La formation de tourbillons due à la séparation des écoulements peut entraîner une apparition précoce du décrochage, un problème de sécurité critique dans les opérations aériennes. Il est donc crucial de comprendre les structures d'écoulement comme les tourbillons.

L'un des cas d'essai qui a suscité beaucoup d'attention est la Wall Mounted Hump (WMH). On peut interpréter ce cas de test comme l'écoulement sur un profil aérodynamique glacé. L'écoulement se sépare de la paroi en franchissant la bosse, représentant la glace, et forme des structures tourbillonnaires. Les objectifs secondaires de cette recherche consistent à réaliser des simulations stationnaires et instationnaires sur la Wall Mounted Hump (WMH). Ces simulations seront utilisées pour l'objectif principal, qui est de quantifier le nombre de tourbillons dans les sections critiques après la bosse pour une analyse plus approfondie. Plus précisément, trois méthodologies d'identification de vortex sont utilisées pour localiser les tourbillonnaires après la bosse. Une comparaison complète du critère Q, du critère λ_2 et des méthodes de force tourbillonnante est entreprise pour évaluer leur efficacité à caractériser le nombre de tourbillons dans différentes sections en aval de la bosse. Une revue approfondie de la littérature est menée sur le WMH, le solveur SU2 et les techniques d'identification des vortex. L'effet de la résolution de la grille et de la longueur de l'envergure sur les coefficients aérodynamiques à travers des simulations stationnaire et instationnaires est étudié.

Cette recherche améliore notre compréhension des effets de la résolution de la grille sur les coefficients aérodynamiques et l'aptitude des différentes techniques d'identification des tourbillons pour l'analyse de scénarios d'écoulement complexes dans les applications aéronautiques. Comprendre ces phénomènes d'écoulement complexes peut conduire à des pratiques de conception améliorées dans l'ingénierie aéronautique, améliorant les performances aérodynamiques et l'efficacité énergétique des aéronefs et autres véhicules aérospatiaux. De plus, les simulations peuvent être améliorées pour prévenir certains dangers liés à la nature des structures tourbillonnaires.

Mots-clés: CFD, Wall Mounted Hump, Givrage, SU2, Spalart Allmaras, Reynolds Averaged Navier Stokes, Delayed Detached Eddy Simulations, Étude de grille, Tourbillons

A Comparative Study of Vortex Identification Methods on the Wall Mounted Hump Simulations Using SU2

Ramin TALEBAN

ABSTRACT

In the last two decades, the researches on the impact of ice accumulation on the aerodynamics of flight has been prevalent. The complex geometry of an iced aircraft wing poses difficulties for engineers in predicting when an airplane may stall due to aerodynamic degradation. Ice accretion on an aircraft wing can alter the flow field, leading to the formation of more vortices. The formation of vortices due to flow separation can lead to an early onset of stall, a critical safety issue in aircraft operations. Thus, understanding flow structures like vortices is crucial.

One test case that received considerable attention and was high-referenced is the Wall Mounted Hump (WMH). This test case can be interpreted as the flow over an iced airfoil, where the flow separates from the wall upon crossing the hump, symbolizing the ice, and forms vortex structures. As secondary objectives of this research we will carry out steady and unsteady simulations on the WMH and quantify the number of vortices in critical sections following the hump for further analysis. The main objective is to use three vortex identification methodologies to identify potential vortex locations after the hump. A comprehensive comparison between the Q-criterion, λ_2 criterion, and Swirling Strength methods is undertaken to assess their effectiveness in characterizing the number of vortices in different sections downstream of the hump. Literature review is conducted on the WMH, the SU2 solver, and vortex identification techniques. The influence of grid resolution and spanwise length on aerodynamic coefficients through steady and unsteady simulations are examined.

This research enhances our understanding of the effects of grid resolution on aerodynamic coefficients and the suitability of different vortex identification techniques for analyzing complex flow scenarios in aeronautical applications. Understanding these complex flow phenomena can lead to improved design practices in aeronautical engineering, enhancing aerodynamic performance and fuel efficiency of aircrafts, and other aerospace vehicles. Furthermore, simulations can be improved to prevent hazards associated with the nature of vortex structures.

Keywords: CFD, Wall Mounted Hump, Icing, SU2, Spalart Allmaras, Reynolds Averaged Navier Stokes, Enhance Delayed Detached Eddy Simulations, Grid study, Vortex

TABLE OF CONTENTS

Page

LIST OF TABLES

LIST OF FIGURES

LIST OF ABBREVIATIONS

WMH	Wall Mounted Hump
CFD	Computational Fluid Dynamics
SU2	Stanford University Unstructured
NASA	The National Aeronautics and Space Administration
2D	Two Dimensional
3D	Three Dimensional
RANS	Reynolds Averaged Navier Stokes
DES	Detached Eddy Simulations
DDES	Delayed Detached Eddy Simulations
EDDES	Enhanced Delayed Detached Eddy Simulations
LES	Large Eddy Simulations
LB-LES	Lattice-Boltzmann Large Eddy Simulations
WM-LES	Wall Modelled Large Eddy Simulations
WR-LES	Wall Resolved Large Eddy Simulations
DNS	Direct Numercial Simulations
SA	Spalart Allmaras turbulence model
Neg-SA	Negative Spalart Allmaras turbulence model
CFL	Courant–Friedrichs–Lewy condition
CPU	Central Processing Unit

KH	Kelvin-Helmholtz instability.
MAE	Mean Absolute Error
RMSE	Root Mean Square Error
GCI	Grid Convergence Index
PDE	Partial Differential Equations
VTM	Vortex Tilting Measure

LIST OF SYMBOLS AND UNITS OF MEASUREMENTS

ρ	Density
U_∞	Bulk velocity
M_∞	Mach number
Re	Reynolds number
c	Chord length
K	Kelvin
C_p	Pressure coefficient
C_f	Skin friction coefficient
ν	Viscosity
Γ	Circulation
Q	Q-Criterion
u_r	Radial Velocity component
u_θ	Tangential velocity component
u_a	Advective velocity of the flow
Ω	Control volume
S	Surface
P	Pressure
R	Gas constant
T	Favre-Averaged temperature

γ	Specific heat ratio
μ	Dynamic viscosity
μ_t	Turbulent viscosity

INTRODUCTION

The design and analysis of products in the aerospace industry as well as in the surface transportation sectors, such as cars, trucks, and boats, relies on simulations in CFD and also testing (Spalart,P. Venkatakrishnan, 2016). The aircraft design process has changed significantly due to the rapid advancement of CFD technologies over the past few decades. As a result of the continuous use of CFD, wind tunnel time for aircraft development programs and experimental rig testing in programs for developing gas turbine engines and the development time of new concepts has been reduced (Slotnick *et al.*, 2014).

Flow separation has been the subject of many studies, both numerically and experimentally. It is crucial for many applications, including airfoils, diffusers, and vehicle aerodynamics. In most circumstances, separation results in a significant loss in performance. However, a precise prediction of separated flow is challenging (Borgmann, Pande, Little & Woszidlo, 2017), because as explicitly stated by Prandtl (1935), increased pressure, and more importantly an adverse pressure gradient, are the prerequisites for flow separation off the wall in the streamwise direction. In separated flows, due to viscosity, the velocity is minimal near and zero at the wall. In the downstream direction, pressure and friction are overcame by the minimal quantity of momentum and energy along the surface body. The fluid flows in the opposite direction further downstream. This reversing flow breaks down in lower velocity vortices.

The effects of attached flow acceleration can be observed in many viscous-body flows. This acceleration phenomenon often results in downstream flow separation depending on changes in the flow path curvature or shape (Kalsi & Tucker, 2016). As an example, the engine intake can cause the flow to accelerate followed by a sudden decrease in velocity that can separate, leading to a deformed and unstable flow at the fan front. This aerodynamic problem is usually linked to fans and blades fatigue. Therefore, when building engine intakes and labyrinth seals, turbine

blades, and nozzles, it is essential to comprehend and precisely predict accelerated flow features and separation sizes (Oriji & Tucker, 2013).

Another example where the flow field can be impacted is the shape of the wing surface that is altered by ice accumulation on the leading edge of aircraft wing, which changes the flow field. This phenomenon causes the drag to increase and affects the wing pressure distribution and aerodynamic performance. Additionally, Ice accretion on leading edge results in the formation of a separation, wing vibration, early stall, and ultimately loss of the aircraft control (Fatahian, Salarian, Eshagh Nimvari & Khaleghinia, 2020).

To gain a more profound understanding of how this ice accumulation phenomenon impacts the flow field and overall aircraft performance, a variety of numerical models have been developed and implemented. Among them, the Reynolds-Averaged Navier-Stokes (RANS) model stands out due to its common use in the industry and relatively low computational cost. The Reynolds-Averaged Navier-Stokes (RANS) model, derived from the Navier-Stokes Equations (NSE) using a method called Reynolds averaging, has been used to numerically solve these partial differential equations (PDE) that describe the motion of viscous fluids (Blazek, J., 2015). Because of its acceptability and low computational cost, RANS is frequently utilized in industry design (Lee & Kwon, 2019; Li, Zhang & Bai, 2020). This method, however, is unable to capture instantaneous flow structures. Additionally, it performs poorly when simulating massively separated flow (Hao, Wei & Shengye, 2021). Although Large Eddy Simulations (LES) approaches have shown to be effective in a variety of complicated flows, the high computational cost prevents them from being used in real-world flows, although being less than a full Direct Numerical Simulations (DNS) (Iyer & Malik, 2016). Therefore, hybrid models (RANS/LES) have been suggested to benefit from the precision of LES and simplicity of RANS. The first model, Detached Eddy Simulation (DES), developed by Spalart, Jou, Strelets & Allmaras

(1997a), successfully improved estimations when applied to several study flow configurations, specially in separated flows (Spalart *et al.*, 2006).

As technology and understanding of flow dynamics continue to develop, principal organizations and research entities are not only focusing on existing methods but also envisioning the future of computational fluid dynamics (CFD). NASA's CFD Vision 2030 Study, published in 2014, serves as a beacon in this regard, outlining the progressive road map and anticipated technology readiness levels in the field. NASA published the CFD Vision 2030 Study in 2014, as a report describing the state of CFD written by professionals in business, government, and academia in the aerospace industry (Slotnick *et al.*, 2014). Figure 0.1 shows the areas of research and technologies that need to be realized by 2030, which are a component of the CFD Vision 2030 workshop. Each timeline is coloured according to its Technology Readiness Level (TRL), which is divided into three levels: low (red), medium (yellow), and high (green). The TRL scale is intended to show the anticipated general state of each technological readiness at a given period. We can observe a high expectancy that hybrid RANS/LES will reach a TRL by 2030.

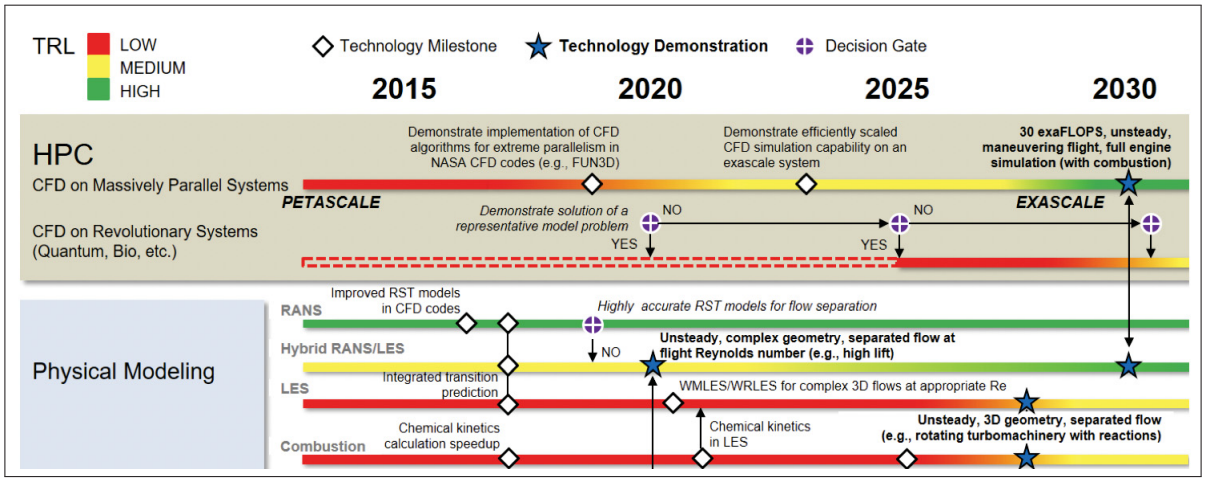

Figure 0.1 A part of road to technology, taken from Slotnick *et al.* (2014)

As many publications have noted, including Shur, Spalart, Strelets & Travin (2015), Guseva *et al.* (2017), and Iyer & Malik (2016), and as we will also go into depth in this thesis, the "gray area issue" in hybrid approaches is where the flow simulation goes from the RANS model to the LES model. This obstacle has been investigated by many researchers in the last decade. One of the proposed ideas is to use an adaptive length scale in volume of interest (Shur *et al.*, 2015) that we will use.

Understanding vortices can help us understand the flow for further improvements of CFD, as this understanding can lead to more accurate simulations of fluid flow behaviour, particularly in complex and turbulent boundary layer scenarios and the design of aerodynamics in vehicles. Because the behaviour of vortices directly impacts the aerodynamic efficiency and vehicle stability (for example the impact of counter-rotating vortices on a delta wing), influencing factors such as drag, lift, and fuel efficiency. A fluid structure with a circular or swirling motion is known as a vortex. As a result, vorticity serves as the primary quantity used to define the flow structure and the skeleton of the flow field (Hong *et al.*, 2008). Vortices produced by flow separation often breakdown in smaller vortices at high Reynolds number, offering crucial insight into overall flow behaviour, such as fluid dynamic drag or propelling efficiency (Krueger, Hahsler, Olinick, Williams & Zharfa, 2019). For the investigation of the physical mechanism of the complicated flow field, the precise extraction of the vortex and the breakdown location of these vortices are therefore crucial. The three categories of current conventional vortex feature extraction approaches include local, global, and hybrid methods. Local methods use the physical characteristics of the flow field to derive various attributes. The careful selection of appropriate thresholds is necessary for these approaches in practical applications to produce reliable findings. Therefore, a quantitative study on a well-known and experimented test case can provide helpful ideas. The importance of vortex detection, the distribution of vortices after the flow separation and the critical importance of accurately characterizing and counting these complex flow phenomena for aeronautical applications will be reviewed. Therefore, the work

undertaken in this thesis contributes to our understanding of flow separation and the number of vortices with current local identification methods.

The primary focus of this thesis is to do a quantitative analysis of the number of vortices in the Wall Mounted Hump (WMH) channel. The first sub-objective is to investigate the RANS simulations with a specific focus on the influence of grid resolution on the results. More specifically, this involves quantifying the discrepancies in the results as the mesh becomes finer. Through this process, we aim to understand the relationship between the level of detail in the computational mesh and the accuracy of the simulation results. This examination will provide valuable insights into optimizing mesh resolution for EDDES simulations. The second sub-objective addresses the so-called grey area issue related to EDDES simulations. This issue is prevalent in hybrid RANS/LES approaches and is associated with the transition region between the RANS and LES models. Identifying the potential causes and proposing solutions to this issue will help to improve the accuracy and reliability of hybrid RANS/LES simulations. These analyses aim to count and evaluate the number of vortices formed in critical locations after the flow passes over the hump. By understanding the behaviour and distribution of these vortices, we can gain a deeper insight into the complexities of flow separation and its effects on aerodynamics, particularly in scenarios that mimic ice accumulation on aircraft wings. These objectives contribute to advancing our understanding of complex flow phenomena, similar to the one encounter behind an ice shape in a more general way, evaluating the accuracy of computational fluid dynamics simulations and briefly contributing to safer and more efficient design of aeronautical protection devices and operation procedures that prevent the associated dangers.

In alignment with our primary objective to shed light on the latest techniques in vortex identification, our research offers several new insights into the WMH test case. We have used the open-source software SU2 for the WMH for the first time, showcasing how well SU2 can

handle complex flow patterns, especially in the steady simulations. Additionally, we are the first to run the unsteady EDDES simulations for the WMH using this software, further highlighting the innovations we have introduced. Beyond these technical strides, we have analyzed three different vortex identification methods for the WMH for the first time, unique methodologies that have not been investigated on the WMH previously.

This research focuses on the WMH test case, which can represent the flow over an iced airfoil. This study is limited to the use of the open-source solver SU2 and the application of the EDDES and the Spalart-Allmaras (SA) turbulence model for conducting numerical simulations. The investigation will evaluate the effect of grid resolution on aerodynamic coefficients and assess vortex behaviour using three vortex identification methodologies. However, it is essential to note that the results and findings of this study may not be directly applicable to other turbulence models or CFD solvers based on the specific requirements of the study. Additionally, the specific flow conditions and configurations considered in this research may not fully capture the complex behaviour of vortex structures under all possible icing scenarios. As a result, the findings of this study should be considered within the context of the chosen methodology and test case, and further research may be required to generalize the results to other contexts or configurations.

This thesis is organized into four chapters. The first chapter offers an extensive review of the relevant works on the WMH test case, the SU2 solver, and vortex identification methodologies. The literature review serves as a foundation of the research and emphasizes the required contributions. In chapter two we will describe the methodologies employed in this work, including the computational setup, the choice of turbulence, configurations of the solver and the vortex identification techniques. Chapter three presents the results obtained from the numerical simulations of our steady and unsteady simulations and provides a detailed analysis of the aerodynamic coefficients, vortex quantities, and the effectiveness of the vortex identification methodologies. Finally, in the conclusion, we will summarize the main findings of the research,

discusses their contributions to the field of aeronautical engineering, and identify the areas for future work.

CHAPTER 1

LITERATURE REVIEW

1.1 Introduction

The primary goal of this chapter is to highlight the most recent studies and projects on flow separation and vortex identification methods so that the background, needs, and contributions made to the discipline are clarified to the reader. In other words, the reader will gain a clearer understanding of the studies done on the Wall Mounted Hump (WMH) test case, especially using the open-source software SU2, limitations of the Reynolds Averaged Navier Stokes (RANS) on separated flows, how the local vortex identification techniques are used and what remains to be done to contribute to the use of hybrid RANS/LES simulations and the behaviour of vortices after flow separation.

In this chapter, the background of the test case that we considered for this master thesis will be discussed in section 1.2. In addition, we will discuss the computational setups used by researchers to compare their numerical results such as pressure coefficient, skin-friction coefficient and separation length to those of experiments, discuss the limitation of the numerical methods and the challenges of the test case. In section 1.3, we will concentrate on the selected solver, its capabilities, and some of the past research works, where it has been used. More precisely, we will look at studies that investigated the numerical settings we are adopting in this thesis. We shall discuss the most recent identification techniques that have been put out for vortex detection in the final section of chapter 1. Finally, section 1.4 will focus on the difficulties in comprehending vortex behaviour and how crucial it is to do so.

1.2 The Wall Mounted Hump

Within the NASA CFDVAL2004 (https://turbmodels.larc.nasa.gov/nasahump_val.html) workshop, one of the documented test cases that has drawn much attention is the WMH (Armstrong *et al.*, 2022). This test case was initially introduced with rich experimental results to assess

different numerical approaches on turbulent flows. The test case can be interpreted as the separation on the upper surface of an airfoil over a hump (Fagbade & Heinz, 2022). The well-researched WMH experiments offer a database for the creation of CFD algorithms that can simulate separation (Siggeirsson & Andersson, 2019). It presents a challenging test case for CFD validation because of its arbitrary curved geometry, unstable separation and reattachment, and high Reynolds number separation bubble (Rumsey, Gatski, Sellers, Vasta & Viken, 2006), (Uzun & Malik, 2017).

Figure 1.1 shows the configuration of the Glauert-Goldschmied type body. The body has a chord length of 0.42 meter and is fixed on a splitter plate on the wind tunnel floor between two side plates that are 0.584 meter apart and is identical to the setup used by Seifert & Pack (Greenblatt *et al.*, 2006). Similar to the first experiment of Seifert & Pack (2002) of the active flow separation control at high Reynolds numbers, the test case represents an example of flow separation followed by reattachment. The Reynolds number in the Greenblatt *et al.* setup reports a Re=929,000 and a Mach number of Ma = 0.1, which was always held consistent during the experiment with an error of less than 1 percent (Greenblatt *et al.*, 2006).

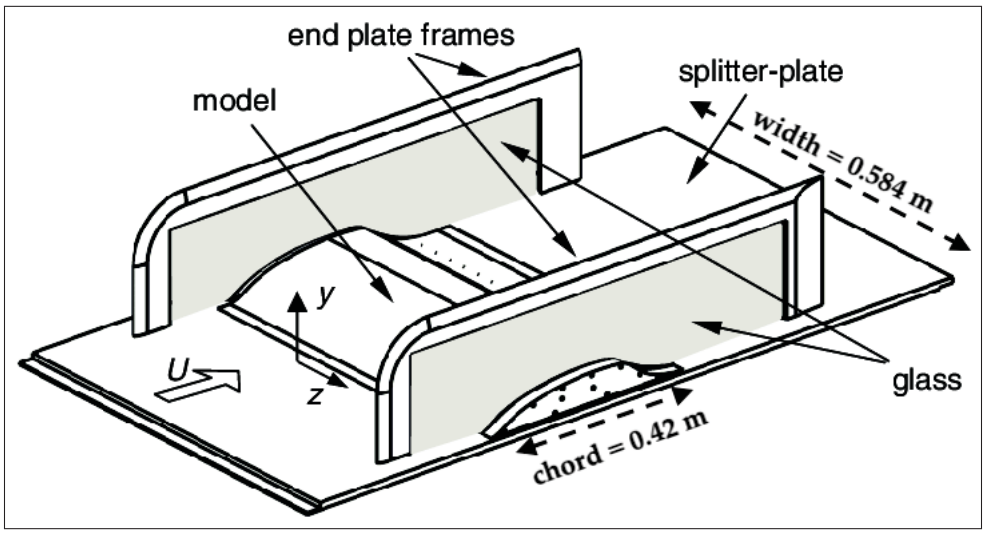

Figure 1.1 Experimental setup of NASA WMH,
taken from Greenblatt *et al.* (2006)

The WMH test case has been the subject of numerous studies (Gritskevich, Garbaruk, Schütze & Menter, 2012). For example, the keyword "Wall Mounted Hump" returns 177 hits in Engineering Village[1] and 874 hits in Google Scholar[2]. Just a few of the related and cited papers are: Kiris *et al.* (2018); Rumsey (2007) for Reynolds Averaged Navier Stokes *(RANS)* simulation, Franck & Colonius (2008); Šarić, Jakirlić, Djugum & Tropea (2006); Sekhar, Mansour & Caubilla (2015); You, Wang & Moin (2006) for Large Eddy Simulations *(LES)*. Taking into account papers of Lattice-Boltzmann based *(LB-LES)* Noelting *et al.* (2008); Kiris *et al.* (2018), Wall Resolved LES *(WRLES)* Uzun & Malik (2017), Wall Modeled LES *(WMLES)* Dilip & Tafti (2014); Iyer & Malik (2016). And also hybrid RANS-LES simulations on the Wall Mounted Hump like Bozinoski & Davis (2012); Šarić *et al.* (2006) for the Detached Eddy Simulations *(DES)* and most importantly, papers that are most relevant to this work: Siggeirsson & Andersson (2019); Guseva *et al.* (2017); Probst *et al.* (2017); Patel & Zha (2020); Peng *et al.* (2014); Armstrong *et al.* (2022); Fagbade & Heinz (2022).

In the NASA Langley Workshop on CFD Validation of Synthetic Jets and Turbulent Separation Control (Rumsey *et al.*, 2006; Seifert & Pack, 2002; Greenblatt *et al.*, 2006) both numerical and experimental simulations are documented. The experiment produced a comprehensive data set that is easily applicable for CFD validations. This section will concentrate on some numerical studies where this test case was mainly used for validation. To start, we will discuss the grids and meshing technique utilized for the WMH test case. Then, we will highlight the primary distinctions between these publications and discuss how well they agree with the experimental findings to clarify the meaning of our numerical results.

The NASA CFDVAL2004 (https://turbmodels.larc.nasa.gov/nasahump_val.html) workshop website offers different grid resolutions for this test case. Five grids, ranging in mesh size from coarse to fine, were initially introduced. These grids were offered both with and without plenum. They are built from hexahedral elements with one element in the spanwise direction. Figure 1.2 is the third grid with 409×109 (in x and y direction respectively). Moreover, we

[1] Engineering Village keyword search performed on May 19, 2023

[2] Google Scholar keyword search performed on May 19, 2023

see a contoured top wall over the hump, which was suggested by the NASA CFDVAL2004 workshop(https://turbmodels.larc.nasa.gov/nasahump_val.html), to account for the side-wall blockage effect, allowing the boundary layer to be resolved. This numerical trick was used to account for the installation effects (Kalsi & Tucker, 2016).

The near-wall fine grid resolves the little structures in the boundary layer, whereas the coarser outside grid is suitable for bigger structures far from the wall (Uzun & Malik, 2017). Furthermore, because of the flow separation that occurs over the hump surface due to unfavourable pressure gradients, a denser meshing is needed in the separation zone to capture the small structures (Fagbade & Heinz, 2022).

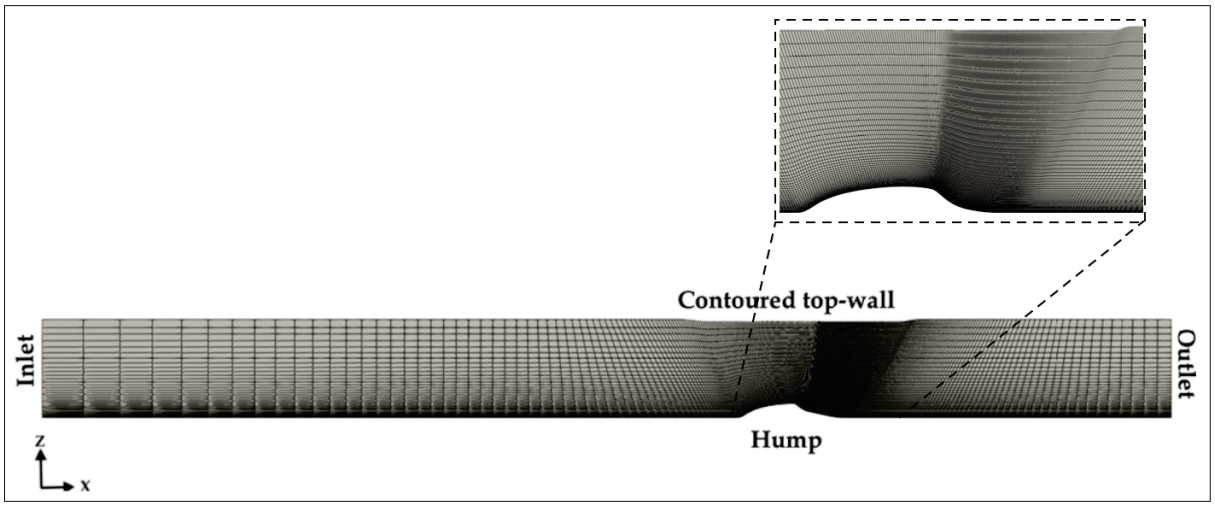

Figure 1.2 Computational domain (x-z view) of the WMH (NASA CFDVAL2004 workshop)

In RANS simulations, the flow quantities are divided into their time-averaged and fluctuating components to simulate a turbulent flow. However, as we will discuss further, the RANS simulations can only resolve large and time-averaged scales eddies. Therefore, RANS predicts a much larger separation area in the WMH simulations showing that using RANS alone has limitations for this test case (Patel & Zha, 2020; Bozinoski & Davis, 2012; Krishnan, Squires & Forsythe, 2006; Guseva *et al.*, 2017; Menter, Hüppe, Matyushenko & Kolmogorov, 2021).

During the last decades, it has been clear that RANS is the basis for the studies conducted by academics and other individuals to assess the validity of hybrid RANS models. The RANS approach, with its extensive history, computational efficiency, broad applicability, and well-understood behavior, naturally positions itself as a foundational pillar in turbulence research. Even as more advanced models are developed, RANS remains an essential benchmark and reference point in the field of computational fluid dynamics (Blazek, J., 2015). We will begin by summarising two studies that were carried out at the NASA Langley Research Center. In the papers by Rumsey (2007) and Kiris *et al.* (2018), despite the limitations of the RANS simulations on the WMH, they employed the RANS simulations along with the hybrid RANS/LES and experiment to evaluate the hybrid RANS simulations as well as confirming the proper turbulence model implementation.

Three distinct turbulence models reviewed by Rumsey (2007) generated results that were quite similar. These turbulence models were the Spalart-Allmaras (SA) one equation model (Spalart & Allmaras, 1994), Menter's $k-\omega$ two equations SST Model (Menter, 1994) and the Explicit Algebraic Reynolds Stress Mode in $k-\omega$ form (EARSM-kω) (Rumsey,C & Gatski, 2003). These simulations were conducted using the CFL3D solver. The over prediction of their RANS separation length were thought to be caused by the fact that the modelled turbulent shear stresses in the separated region were too low in magnitude compared to the separation point of the experimental results to a point that showed using RANS alone is not sufficient. They compared the results with and without the blocking effect (the curve on the wall above the hump). This modification demonstrated that findings were improved by accounting for the blockage effect. For an unsteady case, they conducted a grid study to investigate two grids, the structured medium mesh (53,000 grid points) and a finer mesh (210,000 grid points), resulting in an insignificant difference (generally less than 5%) in long averaged periods of C_p. Finally, the SA one equation turbulence model was used to investigate two eddy viscosity away from the wall. With an arbitrarily turbulence model that was modified to produce twice the eddy viscosity in the separation region away from the wall, an interesting finding was that the size of the separation bubble was reduced. However, the flow field had too little mixing, causing it to

reattach much later than the experiment suggested, while also underestimated the turbulence shear stresses (Rumsey, 2007).

Later on, Kiris *et al.* (2018), due to the limited computational details provided in the previous papers, conducted a thorough review on the WMH with RANS as well as hybrid RANS/LES simulations. For the RANS results with the reattachment location being located at 1.263 m (compared to 1.10 ± 0.005 m of the experimental results), and the separation location being located at 0.661 m (compared to 0.665 ± 0.005 m of the experimental results) after the hump being at zero with a height of 0.128 m, the RANS results had an error of 38.3 % compared to the experimental results, while this error was decreased to 31.2 % using the hybrid RANS/LES approach. Additionally, they used the zonal-DDES(ZDDES), with noticeably better results than normal DDES. The reason for using ZDDES was to capture smaller flow structures. Indeed, they enforced the solver to apply RANS and LES methods specifically in selected regions (employing LES in the separation area and near the wall while using RANS in attached areas). The only way to do this is by defining the zones for each test case which takes a lot of time and cannot be generalized, whereas optimizing the Hybrid RANS-LES has the potential of being used in other simulations without defining the regions.

One of the important works, is the paper by Siggeirsson & Andersson (2019). The computational setup and the approach that we have taken in this thesis is similar to the one they have used. Siggeirsson & Andersson (2019) used the SA-DDES model. They used two grids for the DDES simulations and used RANS simulations with four different grids to ensure that the turbulence model developed by Spalart and Allmaras was properly implemented in their simulation. Table 1.1 shows the grids they have used for their simulations. In the last column of Table 1.1 we can see the longer reattachment lengths compared to the one in experiment (x/c = 1.10 ± 0.005).

Siggeirsson & Andersson (2019) have conducted two DDES simulations where the differences were in the grid spacing and topology. "DDES 1" grid had 1.27 millions total nodes (236 nodes in the stream wise direction × 90 nodes in the normal direction × 60 nodes in the spanwise direction) while "DDES 2" grid had 5.12 million total nodes (474 nodes in the stream wise

direction × 180 nodes in the normal direction × 60 nodes in the spanwise direction). The "DDES 1" grid is generated by extending the "RANS 2" grid that they used (with 249×90 in x and y-direction) in the span-wise direction. While the "DDES 2" grid is generated to have slightly larger cells in separation area but more uniform towards the outlet. Moreover, the span-wise size for both of these simulations is z/c = 0.2.

The size of the domain in the span-wise direction is 0.2c. With 50 inner iterations, the time step is set to $4 \times 10^{-3} c/U_0$ to ensure a CFL (see section 2.2) value of around 1 in the region of interest. Their findings revealed an extended shear layer in the separated region, delaying the transition from RANS to LES. They believed this was due to the lack of grid resolution in the separation region. This delay affected the velocity profiles downstream of the hump and the reattachment location. Out of five full flows they have selected the last three full flows for time averaging. In the end, they concluded that a meshing that combines the DDES1 and DDES2 topology and even has a finer meshing in the separation area is required to have better results compared to the ones in the experiment.

Table 1.1 Grid information of Siggeirsson & Andersson simulations

Grid	n_x	n_y	n_z	n_{tot}	Re-attachment length (x/c)
RANS 1	123	45	-	0.006M	1.251
RANS 2	249	90	-	0.02M	1.24
RANS 3	501	180	-	0.09M	1.225
RANS 4	1005	360	-	0.36M	1.205
DDES 1	236	90	60 (z/c = 0.2)	1.27M	1.212
DDES 2	474	180	60 (z/c = 0.2)	5.12M	1.236

Figure 1.3 contrasts the outcomes of Siggeirsson & Andersson's two DDES simulations, a steady-state simulation and the experimental findings. We can observe flow separation ranging from x/c = 1.10 ± 0.005 (for the experiment) to 1.266 for DDES2. Figure 1.3b better distinguishes the re-attachment location of their simulations. We can observe that DDES1 is the closest to

the experimental re-attachment point (at around x/c 1.12), while the steady-state and unsteady DDES2 have a longer separation length. The spanwise length used in the transient simulations of Siggeirsson & Andersson was z/c= 0.2. They suggested investigating other spanwise sizes to pinpoint the origin of the late transition from RANS to LES.

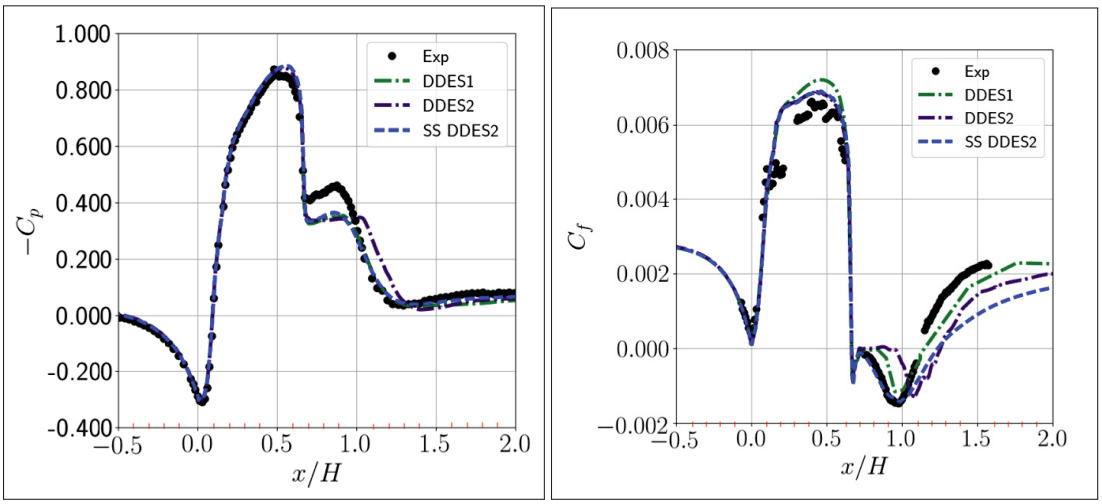

a) Pressure coefficient (C_p) b) Skin friction coefficient (C_F)

Figure 1.3 Distribution of the pressure and skin friction coefficient along the wall of the WMH, taken from Siggeirsson & Andersson (2019)

In the paper by Armstrong *et al.* (2022), they employed two groups of unstructured grids in their investigation; namely P1 and P2. The P1 and P2 grids came in three different sizes: (103 x 28), (205 x 55), and (409 x 109). The P1 grids were derived from NASA CFDVAL2004 (https://turbmodels.larc.nasa.gov/nasahump_val.html) modelling resource page. However, for the P2 grid set, Armstrong *et al.* used a mesh generator for high-order numerical method. The area of flow separation received a finer mesh treatment in P2 grids. The mesh topology difference can be seen in the Figure 1.4.

The turbulent Navier Stokes equation (RANS) and the negative Spalart Allmaras (SA-NEG) turbulence model were employed. The boundary condition and computational domain was similar to other papers. Patel & Zha and Armstrong *et al.* did not exclude the first part (from

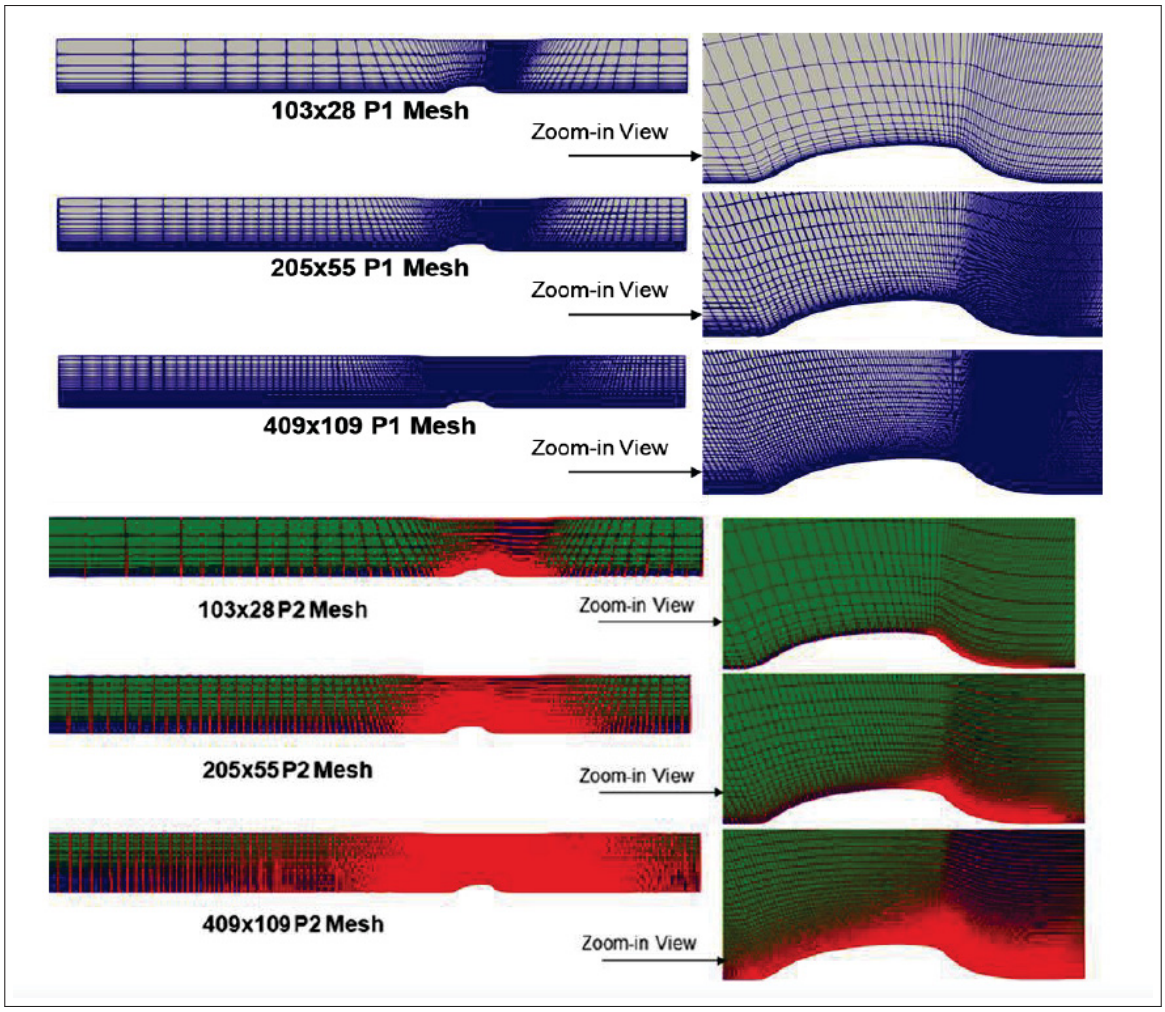

Figure 1.4 The difference between the P1 and P2 grid topology.
The red lines represent the high order cells in grids,
taken from Armstrong *et al.* (2022)

x/c=-6 to x/c=-2.14) of the WMH. They applied a no-slip wall condition on the bottom wall. The numerical methods they used for the DDES simulations, however, are unknown. Moreover, based on the idea of Shur *et al.* (2015); Armstrong *et al.* (2022) compared the DDES results using various delta scaling constants (a_1 in equation 2.14), P1 and P2 grid sets, as well as grids with linear and curved geometries. The re-attachment location for their P2 grids where around x/c = 1.25 to 1.3. Armstrong *et al.* (2022) believed the reason behind this error (compared to x/c = 1.10 ± 0.005 in experiment) was that the turbulent boundary layer directly at the wall was

most likely not adequately captured. They believed one would require either the construction of a wall model or finer grid resolution at the wall to achieve better results.

Patel & Zha (2020) used the DDES with SST turbulence model. They used the second coarse mesh provided on the NASA CFD validation website (205×55×1). In addition, they reduced the span-wise size from 1c to 0.2c, leading to 205×55×25 number of cells in x,y and z-direction respectively for the DDES simulations.

Table 1.2 Grid information of Patel & Zha simulations

Grid	n_x	n_y	n_z	n_{tot}
RANS A	205	55	-	0.01M
RANS B	409	109	-	0.04M
RANS C	817	217	-	0.17M
DDES A	205	55	25	0.28M

A time step of $\Delta t = 2.5 \times 10^{-3} c/U_\infty$ was chosen. This configuration was meant to provide a CFL value of 2 in the region of interest. They disregarded the first 60 percent of the solution in statistical time-averaging to prevent initial flow transition effects. According to the Patel & Zha model, x/c = 1.18 was the reattachment point in their EDDES simulation. Compared to the SST turbulence model result (x/c=1.27), their results appeared good.

In hybrid RANS-LES methods exists a zone known as the 'gray area.' This region, encountered during the transition between RANS and LES modeling approaches, represents a zone where neither the averaged dynamics of RANS nor the resolved scales of LES are adequately captured. As a result, the model can exhibit unpredictable behaviors and may not truly reflect the underlying physics of turbulent flows. This problem was first introduced and explained in Spalart *et al.* (1997a) and then profoundly elaborated upon by Shur *et al.* (2015) who highlighted the challenges posed by the gray area specially on the WMH test case where a longer separation than the experimental results happened.

In the works of Probst *et al.* (2017), Guseva *et al.* (2017), and Peng *et al.* (2014), the computational domain had a considerably finer resolution than the one which was used in the paper by Patel & Zha (2020). Their mesh had around 5 million cells (with 511×127×80 cells in the x, y, and z directions, respectively). The size in the spanwise direction is equivalent to 0.4c in their simulation. They used a time step of $\Delta t = 2 \times 10^{-3} c/U_\infty$ to achieve a CFL value well below 0.5. For the temporal sample for averaging turbulence data, the first third of the solution was disregarded, and then it was also averaged in space. They have used the SA-EDDES method for their simulations but with higher order schemes than the one we have selected (see section 2.3) that showed a decrease in the error in the separation length compared to the experimental results.

Guseva *et al.* (2017) have used a weighted, 4th-order centred and a 3rd-order upwind for the inviscid fluxes with the spanwise length of z/c = 0.4. Figure 1.5 compares the results of Guseva *et al.* between the experimental results, normal DDES, SLA DDES (EDDES) and Zonal IDDES (Zonal EDDES). We can see that their results are closer to the experimental results, and the gray area issue has been resolved.

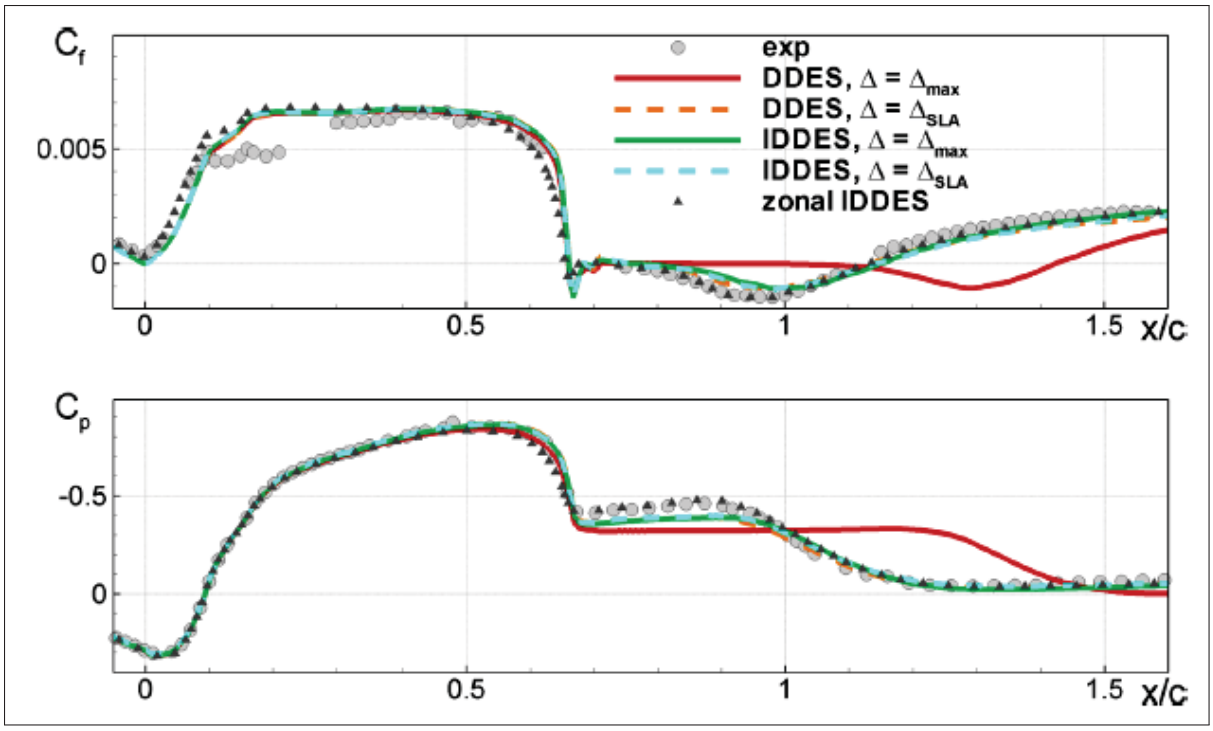

Figure 1.5 The time and spaced averaged skin friction coefficient (on top) and the pressure coefficient (bottom), taken from Guseva *et al.* (2017)

The findings from the chosen publications demonstrate that RANS simulations alone are insufficient to achieve good agreement with the experimental results in predicting the flow separation location. It must be noted here that the Reynolds number used in these numerical simulations is Re = 936000 and in the experimental setup, is Re = 929000. This minor difference of less than 1 percent with the numerical setup is believed to be insignificant (Greenblatt *et al.*, 2006). Moreover, despite employing the adaptive scale technique, the results from the EDDES simulations show that a fine mesh (more than 5 million cells) is still needed close to the separation area toward the outlet. That would justify the delay of RANS to LES in the separation area. Therefore, based on the literature review, to reach the sub-objectives pointed out earlier, it is critical to assess the effects of grid resolution in predicting aerodynamic coefficients on the wall of the WMH as well as the separation location. Moreover, for the unsteady EDDES simulations,

we should investigate the effects of the span-wise length on the solution as various span-wise lengths were used in the literature and was suggested for further investigations.

1.3 Assessment of the DDES simulations with the SU2 solver

The solver that is used in this study for the simulations is the open-source code SU2 (Economon, Palacios, Copeland, Lukaczyk & Alonso, 2016). SU2 is specially built to analyze partial differential equations with avant-garde numerical methods. This section is intended to take a closer look on publications that have shown, improved, or validated the use of SU2 with the DDES simulations. Although SU2 is designed to solve any problems that can be reduced to partial differential equations (PDE), it is especially effective with aerodynamic problems (Keep, Vitale, Pini & Burigana, 2017).

Molina *et al.* (2017)'s work provides a thorough explanation of hybrid RANS/LES algorithms implemented in the SU2. Molina *et al.* concentrated on the modifications required to implement the Delayed Detached-Eddy Simulation (DDES) method to the existing RANS framework built upon the Spalart-Allmaras turbulence model. They came up with a series of test cases for various regimes to show the SU2 DDES capacity on both academic and professional-grade applications.

A high level overview of the SU2 package is presented by Molina *et al.* In particular, second-order convective techniques suitable for hybrid RANS/LES calculations with low Mach and low dissipation were discussed. They tested 4 cases that have been selected as a sample set of the wide range of scale-resolving applications for which SU2 has been developed in order to show the initial implementation of hybrid RANS/LES models. These test cases were Spatial Shear Layer, Zero Gradient Flat Plate, Backward Facing Step (BFS) and the NACA0021 airfoil in deep stall (Molina *et al.*, 2017). The main difficulty with hybrid approaches, according to Molina *et al.* (2017), is being able to precisely evaluate the subgrid-scale velocity components. One also needs a suitable numerical technique, to maintain the RANS solution quality, and advanced numerical methods, which SU2 offers.

To validate the capabilities of SU2, we will use two well-known test cases. The BFS and NACA0012 have rich information accessible within the NASA Langley research center TMR section by Rumsey and in the literature Eaton & Johnston (1981); Jacob, Louisot, Juvé & Guerrand (2001). One of the referenced papers that validate their proposed DDES simulation is the paper by Spalart *et al.* (2006). They have used circular cylinder, single airfoil, BFS and multi-element airfoil test cases using RANS, DES97 and DDES. They believed the BFS is a perfect choice for hybrid methods. Therefore, researchers like Gritskevich *et al.* (2012); Deck (2012); Reddy, Ryon & Durbin (2014); Shur, Spalart, Strelets & Travin (2008); Sainte-Rose, Bertier, Deck & Dupoirieux (2009) are only some of the highly cited papers that used BFS with the DDES. Moreover, for the NACA0012, To mention a few, we can consider Im & Zha (2014a); Jain & Baeder (2015); Gao & Li (2017); Yang & Zha (2016); Tagawa *et al.* (2019), that all used the DDES, at different angles of attacks.

BFS is well known for its application in the studies on turbulence in internal flows (Tagawa *et al.*, 2019). The flow separation is due to the sudden change in the geometry (Satheesh Kumar, Singh & Thiagarajan, 2020). This sudden change creates a re-circulation zone, a point of flow re-attachment like the one after the hump in the WMH. Thus, the BFS and WMH test cases share some similarities in their properties. The WMH produces a region of flow re-circulation just downstream of the hump, which is also present in the flow over the BFS. They are, therefore, excellent candidates to evaluate the performance of numerical solvers. In addition, the flow over the NACA0012 in high and reversed angles of attack also separates from the leading edge of the airfoil. These angles of attack were investigated thoroughly by Shan, Jiang, Liu, Love & Maines (2008). By using SU2, Tagawa *et al.* (2019) studied the impact of span width length on the pressure coefficient and anticipated aerodynamic coefficients. The shear-layer modified DDES approach of SU2 was presented first. The numerical findings were validated using the BFS and a stalled NACA0012. They also analyzed the numerical flow over an iced Model 5-6. Tagawa *et al.* studied the BFS using a Reynolds number of 36000 and a Mach number of 0.128. The Reynolds number was determined by the step length. 298.33 K serves as the reference temperature, and the wall heat flux has been set to zero. Due to the strong resemblance between this arrangement and

the computational setup we are employing for the WMH, we will briefly look at their findings here.

The 2D grid from NASA CFDVAL2004 (https://turbmodels.larc.nasa.gov/nasahump_val.html) web-page served as the foundation for the computation grid that was employed. A 3D example with 821,600 points was produced by extending the original mesh, a four-zone mesh with 20,540 nodes, by 40 nodes in the z-direction over a spanwise length of z/H = 4 with H being the thickness. A fluid particle may travel the domain almost five times with a non dimensional time steps sets $\Delta_t^* = \Delta t U_\infty / H = 0.2$ in 19.4 seconds, or 43000 time-steps during the simulation. The latest 1.3 seconds were used to get the statistical average (3000 iterations) (Tagawa *et al.*, 2019).

Tagawa *et al.* (2019) explain that the mean wall pressure coefficient and friction coefficient distribution along the lower wall of the BFS test case that was simulated using SU2 have acceptable agreement with Molina, Silva, Broeren, Righi & Alonso (2019) numerical and Dietiker & Hoffmann (2009) experimental results. Tagawa *et al.* explain the tiny gap of around 0.02 % in C_p distribution and 2.28 % in C_f was due to the fact that Molina *et al.* have not explicitly stated their sampling size. Tagawa *et al.*'s NACA0012 results in deep stall also had a great agreement with the Im & Zha (2014b) numerical findings. Table 1.3 shows how the experimental results and the DES, URANS, and DDES results of Im & Zha differ from the DDES results obtained using SU2. Therefore, we can see the potential of SU2 in predicting flow properties compared to other numerical solvers.

Table 1.3 Comparison of Tagawa *et al.* lift and drag coefficients of NACA 0012 in deep stall results with the literature and experiment, taken from Tagawa *et al.* (2019)

Author	Im & Zha	Im & Zha	Im & Zha	Im & Zha	Tagawa *et al.* (SU2)
Method	URANS	DES	DDES	Experiment	DDES
C_D	1.421	1.075	1.076	1.109	1.077
C_L	1.432	1.086	1.087	1.168	1.064
Error % C_D	24.190	0.215	0.048	2.885	N/a
Error % C_L	25.699	2.001	2.092	8.904	N/a

The analysis of the turbulent flow around a Gates Learjet Corporation-305 airfoil with a leading edge horn-shape glazing ice was then pursued by Molina *et al.* (2019). For this simulation, Molina *et al.* (2019) used an unstructured grid design compatible with SU2. Molina *et al.* devised the computational domain to have a far-field boundary condition 40 chords away from the airfoil (with a spanwise length of 0.5c). The sharp trailing edge has two chords downstream, insuring a dimensionless y^+ (see section 2.2) of the last grid to be less than one around the airfoil. Moreover, the grid is stretched over 60 layers with a ratio of 1.1, filled with triangle shape grid cells up to the far-field. Molina *et al.* also gave close attention to refining the grid around the ice-ridge. The baseline grid has a size of 0.1c in the focus region around the ice (x-z direction), and the baseline and fine grids were extruded in the spanwise direction with 50 and 100 layers for the same span-wise dimension, respectively. This resulted in a medium grid of roughly 3 million cells and a fine grid of 10 million grid units. The non-dimensional time step was set to $\Delta t^* = \Delta t U_\infty / c = 0.0001$, with 20 sub-iterations in a dual-time step approach. They used the HR-SLAU2 scheme with the Venkatkrishnan limiter Venkatakrishnan (1993) for the convective numerical scheme. The unsteady simulation was used from the RANS solution, the first third of the transient phase was not used for the time averaging (Molina *et al.*, 2019). For the DDES coupled with (HR)-SLAU2 numerical method Molina *et al.* used the Shear-Layer Adapted (SLA) sub-grid scale (SGS), the predictions improved by modifying the SGS to accelerate the

RANS to LES transition to reduce the gray area issue as it was discussed in section 1.2 (by replacing Δ_{max} with Δ_{SLA}(Shur *et al.*, 2015)). It was evident from the comparison of Δ_{SLA} and Δ_{max}, that Δ_{max} results exhibit a significant delay in the roll-up of the shedding vortex and, as a result, the emergence of Kelvin-Helmholtz instability (Molina *et al.*, 2019).

To reduce the viscosity in the numerical method, they use a low dissipation correction. The three parameters for the low dissipation scheme are :σ_{min} = 1 (original SLAU2), σ_{min} = 0.05 and σ_{min} = 0.01. The σ_{min} = 0.01 simulations were unstable in certain conditions due to the presence of the ice horn, which according to the experiment, re-attachment occurs at roughly 0.53c from the leading edge. A sizable re-circulation bubble was predicted above the suction surface. Molina *et al.* discovered that by reducing the dissipation parameter, they could move the reattachment point closer. Therefore, Molina *et al.* believed a stable low numerical dissipation convective scheme is essential for accurate prediction of flow over the ice (Molina *et al.*, 2019). The low dissipation parameter σ_{min} = 0.01 has been used for a grid study. Molina *et al.* compared the RANS and EDDES with the base and fine grid. They found out that in an angle of attack of α = 6 deg, both RANS and DDES were capable of accurately predicting the flow separation. However, as they increased the angle of attack, they found that RANS results deviate from the experimental results. Moreover, Molina *et al.* discovered that velocity fluctuations (U_{RMS}/U_{inf}) of the baseline grid and the finer grid were nearly identical when utilizing the Δ_{SLA} method. They believed this is a promising potential for future extension of simulating a full iced-aircraft (Molina *et al.*, 2019).

In unsteady simulations, the hybrid RANS/LES (EDDES) solver offered by SU2 presents a promising potential. We have briefly mentioned few of the test cases like Spatial Shear Layer, Zero Gradient Flat Plate, BFS, NACA0012, NACA0021 and GLC-305 which the SU2 results had a good agreement with other numerical and experimental results. The papers from Molina *et al.* (2017), Molina *et al.* (2019) and Tagawa *et al.* (2019) were just a fraction of SU2 active research. The development of SU2 is expanding and will be further explored in the coming years as RANS/LES hybrid computing capacity increases.

1.4 Vortex identification methodologies

Few people stop to consider what the term "vortex" actually implies because it is used so frequently in fluid dynamics. Those who do take a deeper look immediately understand how challenging it is to clearly define vortices (Wang, Vita, Fraga, Wang & Hemida, 2021). Although vortices are frequently thought of as having high vorticity, there is no set limit above which vorticity should be deemed high. Even more concerningly, vorticity may be strong in parallel mean shear flows without any visible vortices, because vortices are the results of strong vorticity not yet "visible" going unstable. The development of coherent structures holds information about the type of flow regime and can be distinguished by their scales, strengths, and directions, among other characteristics. However, there is not yet a well-established and widely accessible mechanism for extracting these characteristics (Devaux, Thomas, Calluaud & Pineau, 2020).

To fully understand the phenomenon of turbulent motions, coherent structures must be found, tracked, visualised, and analysed. With this knowledge, turbulent flow modelling and predictions can be improved. Because it is not always evident how to quantify the extension of the vortex from its centre of spin, it is challenging to identify vortices and interactions between several coherent structures (Lindner, Devaux & Miskovic, 2020).

Vortex identification techniques should be used to create qualitative and quantitative descriptions of the vortex dynamics based directly on the flow field so that the physical processes of lift generation/loss and moment balancing may be understood (Huang & Green, 2015). Identifying vortices in realistic (complex, unstable, 3D) fluids like in the WMH, is a challenging approach due to the diffusion of vorticity by viscosity and the interplay of vorticity distribution with background strain fields. The difficulties in the identification and visualisation of vortical structures in turbulence have accelerated the development of vortex identification techniques, such as intuitive measurements, Lagrangian objective criteria, and Eulerian velocity-gradient-based criteria (Jeong & Hussain, 1995).

A vortex is typically seen in Lagrangian techniques as a developing region with a high level of material invariance. Typical intuitive signs like local pressure minima, closed or spiralling

streamlines, and pathlines have significant difficulties identifying vortices, as reviewed in great detail by Jeong & Hussain (1995). Almost all Lagrangian methods are based on the flow map, a vector variable that plots fluid paths from their starting points to where they end up in space after some integration period, building a comprehensive picture of how individual fluid particles move and interact in the fluid flow over time(Chakraborty, Balachandar & Adrian, 2005; Haller & Beron-Vera, 2013). For Eulerian methods, the criteria is different.

The examination of the velocity gradient tensor serves as the foundation for the majority of the current widely used Eulerian vortex identification criteria. Numerous frequently employed vortex criteria, such as closed or spiralling streamlines, iso-vorticity surfaces, pressure minima, etc., are Eulerian and are derived using spatial derivatives of the velocity field. According to the Eulerian criteria, coherent structures are typically recognised as concentrated areas of high vorticity that typically contain the key elements of the flow caused by a vortex filament. These Eulerian methods provide a function that may be evaluated point-by-point and then categorize each point as being within or outside a vortex according to a standard based on the point values (Chakraborty *et al.*, 2005).

Most local vortex identification criteria are derived from the velocity gradient tensor (or Jacobian), they are Galilean invariant that remain unchanged when the underlying coordinate system is translated at a constant speed (Fasel & Postl, 2006). The most widely utilized local criteria for vortex identification is as follows:

- Vorticity
- The Q-criterion (Hunt, J. C. R. and Wray, A., and Moin, P , 1988)
- The λ_2-criterion (Jeong & Hussain, 1995)
- The Δ-criterion (Chong, Perry & Cantwell, 1990)
- The Swirling Strength (λ_{ci}^2-criterion) (Zhou, Adrian, Balachandar & Kendall, 1999)
- Rortex (Liu, Gao, Tian & Dong, 2018a)

This following aims to provide information on the benefits and advancements of the listed quantities. Vorticity can acquire significant values even in the presence of shear flows and might

thus result in false detections in non-rotating velocity fields, it might be unwise to include it in this list. Vorticity is simply the curl of the velocity field, $\overrightarrow{v}$, and it is the classical quantity in fluid mechanics used to represent local rotating motions (Blazek, J., 2015), (Canivete Cuissa, J. R. & Steiner, O., 2022).

$$\omega = \overrightarrow{\nabla} \times \overrightarrow{v} \tag{1.1}$$

According to the right-hand rule, the vorticity vector direction shows the rotation orientation, and its norm is proportional to the force of rotation. The norm of the vorticity vector for a rotational vortex, which is a flow spinning rigidly around an axis, is $\omega = |\omega| = 2\Omega$, Ω is the fluid angular velocity. In the context of vortices, gamma (Γ) often represents circulation closely related to vorticity. For a simple vortex, the circulation (Γ) equals the vorticity (ω) times the area (A) enclosed by a given loop, represented by the equation $\Gamma = \Omega \cdot A$. However, for more realistic vortex models in fluid dynamics, such as Lamb-Oseen or Burgers vortices, this straightforward relationships between the vorticity norm and the characteristics of vortical flows does not hold (Canivete Cuissa, J. R. & Steiner, O., 2022).

The Q-Criterion techniques are easy to use because they require the instantaneous velocity field and its gradient. They do, however, have several drawbacks, as discussed by Kolář (2007) and Jeong & Hussain (1995). The structure size and border form can change depending on the value that the user input for iso-surface level value while displaying the data, especially in 3D. Furthermore, these criteria can be thought of as eigenvalue-based criteria because they are only based on the eigenvalues of the velocity gradient tensor or the associated invariants. Although in theory Q should be greater than 0, in actuality, depending on the mesh density, Q must be high in order to detect an actual vortex (Jeong & Hussain, 1995). Many unsteady simulations have employed the Q-criterion to depict the flow and vortical structures over time. In the articles by Siggeirsson & Andersson (2019); Armstrong *et al.* (2022); Patel & Zha (2020); Iyer & Malik (2016); Uzun & Malik (2017); Kalsi & Tucker (2016), that were covered in section 1.2, to see the 3D vortical structures above the WMH, the authors used the Q-criterion to visualize vortices in their unsteady simulations.

The λ_2 criterion proposed by Jeong & Hussain (1995) is a commonly used technique for pinpointing vortices, especially in non-compressible fluid flows. Based on this method, a vortex is identified as connected regions in the fluid where two out of three specific values of the eigenvalues of the symmetric matrix $M = S^2 + \Omega^2$ are negative. Vortices are identified when the condition $\lambda_2 < 0$ holds. This method identifies a vortex based on whether the second largest eigenvalue, λ_2, of the symmetric part of the velocity gradient tensor, is negative. This feature differentiates it from other methods that rely solely on the magnitude of vorticity, allowing it to detect vortices even in complex, changing flow fields. Moreover, unlike other vortex methodologies, the λ_2 and Q-criterion are not affected by the Disappearing Vortex Problem (DVP), making them more consistent and reliable for identifying vortices (Kolář & Šístek, 2022).

The Swirling Strength method (λ_{ci}^2), also known as the local swirling velocity, is based on the imaginary part of the non-zero complex eigenvalue of the velocity gradient tensor. While the λ_{ci}^2 resolves the pure shear flow issue, it is still unable to estimate the angular velocity of more complex and realistic vortices. The λ_{ci}^2 cannot distinguish between the intrinsic shears present in a differentially rotating flow and the rigid-body rotational component of the flow (Canivete Cuissa, J. R. & Steiner, O., 2022). The advantage of λ_{ci}^2 is that the threshold value is defined by Zhou *et al.* (1999) and it would be three percent of the max value.

In recent years, the scientific community has focused on studying Coherent Vortex Structures (CVS) and the instability in complex fluid flows. One of the focuses of their research was on the fluctuations of a fully separated flow, particularly in the zone close to reattachment in low frequencies When the boundary layer flow separates from the wall due to the negative pressure gradient produced by the hump geometry, a shear layer region forms parallel the surface of wall at the edge of the hump. In the shear layer area, the separated flow interacts with the surrounding fluid in a thin, high-shear region. When the separated flow encounters the re-circulation area on the side of the hump or the downside of the BFS while moving downstream, it eventually reconnects with the wall. It is distinguished by a quick drop in turbulence and an increase in the wall shear stress. The flow continues downstream after the reattachment region and starts to recover from the impacts of separation and reattachment.The turbulence will then progressively

diminish as the flow seeks to return to its initial state before separation. These studies continued to the equilibrium of the reattached shear layer (Wang *et al.*, 2019). Figure 1.6 is a simplified representation of the separated flow in the BFS by Wang *et al.* (2019). They have conducted a quantitative analysis of the CVS in the flow over the BFS. In this study, Wang *et al.* has visualized the vortices with the ghosting pictures which was a specific imaging technique to visualize the vortices. Then, he defined the stages of the vortices and their development in the BFS channel. Finally, they studied the vortex centers and their sizes and evolution.

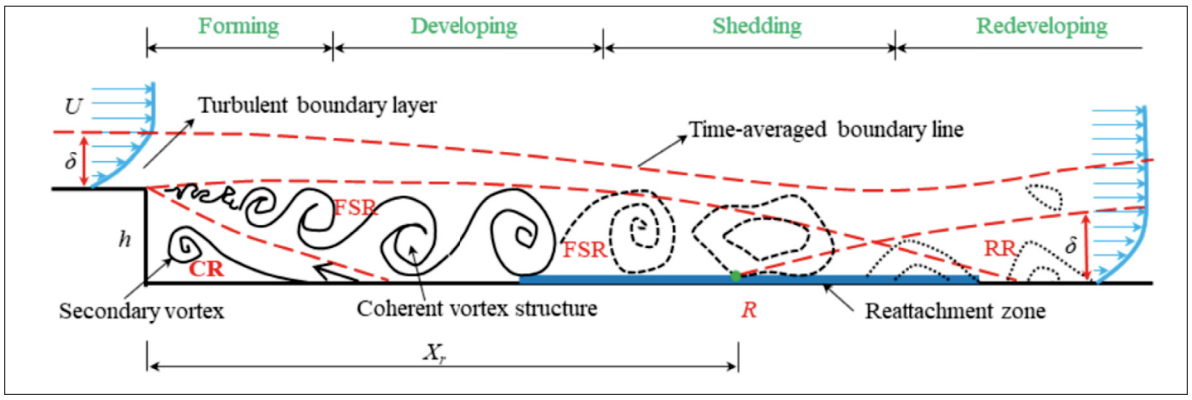

Figure 1.6 The stages of flow structure in a 2D BFS. (FSR = Free Shear Region , CR = Corner region, RR = Redeveloping Region and R is the re-attachment location, taken from Wang *et al.* (2019)

As stated earlier, identifying the vortex behaviour in turbulent and separated flows is challenging. Up to this date, we still lack a universal vortex identification method. This shortcoming has caused confusion and misunderstanding of turbulent flows (Liu, Yan & Lu, 2014). After the introduction of Rortex (Liutex) by Liu *et al.* in 2018, researchers like Yu, Shrestha, Alvarez, Nottage & Liu conducted a correlation analysis on the DNS case of a boundary layer transition between vorticity, Q-criterion and λ_2 criterion and Rortex (Liutex) methods. Due to the low correlation of vorticity, Yu *et al.* suggest that vorticity alone lacks the principle of a vortex identification method. Moreover, they state that although the Q-criterion and λ_2 criterion perform well, yet, these well-known methods cannot give the exact relative strength of fluid rotation (Yu *et al.*, 2020). Moreover, Lindner *et al.* (2020) states that it is feasible to approximate a possible vortex and the location of its centre by using the peak of the highest whirling intensity or by

locating the areas where the Q criterion is higher than 0. According to them, these Eulerian techniques do not always ensure the detection of an actual vortex, even when a threshold is used (Lindner *et al.*, 2020). Therefore, a quantitative study for the number of captured vortices in comparable threshold values on a well-known test case like WMH can give insights into the capabilities of these methods.

In this chapter, we have reviewed eight papers that used similar numerical settings on the WMH test case, particularly, we have defined the computational setups and discussed their main findings. Then, we have reviewed paper that used SU2 as their solver to simulate flow in similar test cases. Finally, we defined vortex, how they are usually identified and what are the shortcomings of their identification techniques.

CHAPTER 2

MATHEMATICAL MODEL AND METHODOLOGY

2.1 Introduction

In the previous section, we reviewed the works of the literature that used the same or comparable settings in their WMH simulations. In this section, we intend to dig deeper into the properties and configurations used in our simulations. In the first part, we will discuss the general mathematical and physical expressions in more detail. More specifically, we will define the underlying mathematics used by the SU2 solver to run the simulations. We will discuss the options, capabilities of the solver and the numerical configurations we have used to run our steady and unsteady simulations. In the last part, we will discuss the vortex identification methods used in this thesis. More specifically, we will define the mathematics of three vortex identification techniques.

2.2 Mathematical model

In contrast to laminar flows, the distinguishing characteristic of a turbulent flow is that fluid particles move chaotically along complex, irregular paths. In turbulent zones, several fluid layers are strongly mixed by the strong chaotic motion. Turbulent wall bounded flow results in more skin friction and heat transfer than laminar flow under the same conditions because of the improved momentum and energy exchange between fluid particles and solid surfaces (Blazek, J., 2015).

Even though the Navier Stokes Equations (NSE) can be used to analyze turbulence, doing so at high Reynolds numbers is impossible due to the massive range of length scales that must be resolved. (Kundu, Cohen & Dowling, 2016). Moreover, only very straight-forward flow problems at low Reynolds numbers (in the range of 10^4 to 10^5) can be directly simulated by the time-dependent NSE, also known as the Direct Numerical Simulation (DNS). Because of the number of grid points required for adequate spatial resolution scales as $Re^{9/4}$ and the CPU-time

as Re^3, greater use of the DNS is prevented. So, we are compelled to account for the effects of turbulence without fully reaching it (Blazek, J., 2015). Using the Reynolds decomposition to evaluate the statistical mean flow from the fluctuating part, it is possible to rewrite the NSE into the Reynolds Averaged Navier Stokes (RANS) equations.

With a control volume Ω defined by a close surface of S and with a normal vector of $\overrightarrow{\mathbf{n}}$, the integral form of continuity equation is (Blazek, J., 2015):

$$\frac{\partial}{\partial t}\int_{\Omega}\rho d\Omega + \oint_{\partial\Omega}\rho(\mathbf{v}\cdot\mathbf{n})dS = 0 \tag{2.1}$$

where ρ is the density, and $\mathbf{v}$ is the air velocity vector. Also, the momentum equation with $\boldsymbol{\text{ø}}$ being the shear stress is written as:

$$\frac{\partial}{\partial t}\int_{\Omega}\rho\mathbf{v}d\Omega + \oint_{\partial\Omega}\rho\mathbf{v}(\mathbf{v}\cdot\mathbf{n})dS = -\oint_{\partial\Omega}p\mathbf{n}dS + \oint_{\partial\Omega}(\boldsymbol{\text{ø}}\cdot\mathbf{n})dS \tag{2.2}$$

And the energy equation :

$$\frac{\partial}{\partial t}\int_{\Omega}\rho E d\Omega + \oint_{\partial\Omega}\rho H(\mathbf{v}\cdot\mathbf{n})dS = \oint_{\partial\Omega}k(\nabla T\cdot\mathbf{n})dS + \oint_{\partial\Omega}(\boldsymbol{\text{ø}}\cdot\mathbf{v})\cdot\mathbf{n}dS \tag{2.3}$$

where E is the total energy per unit mass, H is the total enthalpy per unit mass, k is the thermal conductivity and T is the temperature.

There are six additional unknowns called Reynolds stresses as a result of developing RANS equations. So, to solve these issues, a turbulent model is needed. The kinematic eddy viscosity (ν_t) is determined by a single transport equation in the classic Spalart-Allmaras model (SA) (Spalart & Allmaras, 1994). It has been demonstrated that this model performs well with respect to boundary layers and negative pressure gradients. Thus, this model has gained popularity for use in external aerodynamics (Javaherchi, 2010).

The SA one-equation turbulence model (Spalart & Allmaras, 1994) employs transport equation for an eddy-viscosity variable $\hat{\nu}$. It was developed based on empiricism, dimensional analysis,

and Galilean in-variance (Spalart & Allmaras, 1994). It was calibrated using results for 2D mixing layers, wakes, and flat-plate boundary layers. The SA model also allows for reasonably accurate predictions of turbulent flows with adverse pressure gradients (see for example Constantinescu, Chapelet & Squires (2003); Kalitzin, Medic, Iaccarino & Durbin (2005); Breuer, Jovičić & Mazaev (2003); Bardina, Huang & Coakley (1997)).

The SA model has several favorable numerical features. It is "local", which means that the equation at one point does not depend on the solution at other points. Therefore, it can be readily implemented on structured multi-block or on unstructured grids. It is also robust, converges rapidly to steady-state, and requires only moderate grid resolution in the near-wall region (Spalart & Allmaras, 1994).

We provide the standard SA model (Spalart & Allmaras, 1994) for reference. The Boussinesq eddy viscosity assumption is used to calculate Reynolds stresses and the eddy viscosity ν_t is determined by:

$$\nu_t = \hat{\nu} f_{\nu 1}, \qquad f_{\nu 1} = \frac{X^3}{x^3 + c_{\nu 1}^3}, \qquad x \equiv \frac{\hat{\nu}}{\nu} \tag{2.4}$$

where ν is the kinematic viscosity. The working variable for the SA and transport equation is $\hat{\nu}$, where:

$$\frac{D\hat{\nu}}{Dt} = P - D + T + \frac{1}{\sigma}\left[\nabla.((\nu + \hat{\nu})\nabla\hat{\nu}) + c_{b2}(\nabla\hat{\nu})^2\right] \tag{2.5}$$

in which, production, wall destruction, and diffusive terms are:

$$P = c_{b1}(1 - f_{t2})\hat{S}\hat{\nu}, \qquad D = \left(c_{wq} f_w - \frac{c_{b1}}{k^2} f_{t2}\right)\left[\frac{\hat{\nu}}{d}\right]^2, \qquad T = f_{t1}(\Delta u)^2 \tag{2.6}$$

The modified vorticity is $\hat{S}$ and given by:

$$\hat{S} \equiv |S| + \frac{\nu}{k^2 d^2} f_{v2}, \qquad f_{v2} = 1 - \frac{X}{1 + X f_{v1}}, \tag{2.7}$$

where in this equation, the vorticity magnitude is |S|, and d is the distance from the nearest wall. For defining f_w is:

$$f_w = g\left[\frac{1+c_{w3}^3}{g^6+c_{w3}^6}\right]^{1/6}, \qquad g = r + c_{w2}(r^6 - r), \qquad r = min\left(\frac{\hat{\nu}}{\hat{S}k^2d^2}, r_{lim}\right). \tag{2.8}$$

The coefficients in P,T and D terms are given by:

$$f_{t1} = c_{t1}g_t exp\left(c_{t2}\frac{\omega_t}{\Delta u^2}[d^2 + g_t^2 d_t^2]\right), \qquad f_{t2} = c_{t3}exp\left(-c_{t4}X^2\right), \tag{2.9}$$

Here $g_t = min(0.1, \Delta u/\omega_t \Delta x)$, where d_t is distance to transition point (from laminar to turbulent). ω_t is the vorticity at the transition point, Δu is the change in velocity relative to the transition point, Δx is the stream-wise grid spacing at the same point.

The previously mentioned constants are:

$$\begin{gathered} c_{b1} = 0.1355, \qquad \sigma = 2/3, \qquad c_{b2} = 0.622, \qquad k = 0.41, \\ c_{w1} = \frac{c_{b1}}{k^2} + \frac{(1 + c_{b2)}}{\sigma}, \qquad c_{w2} = 0.3, \end{gathered} \tag{2.10}$$

and, $r_{lim} = 10$, no-slip wall: $\hat{\nu} = 0$, symmetry plane: $\partial\hat{\nu}/\partial n = 0$ and free-stream (fully turbulent): $\hat{\nu}/\nu$ = a range of 3 to 5 and free-stream: $\hat{\nu}/\nu \ll 1$

In the original SA model, the eddy viscosity is usually positive. However, in the Negative Spalart Allmaras (NSA) model, it can occasionally turn negative. As a result, the NSA model can depict the effects of back-scatter, which is the transfer of kinetic energy in turbulence from smaller sizes to larger scales. The NSA model is more accurate than the original SA model when predicting turbulent flows with boundary layer separation, as demonstrated by the test cases in the paper (Allmaras, Johnson & Spalart, 2012). The ability to represent back-scatter and its improved performance in predicting separation makes the NSA model a better option for separated flows (Allmaras *et al.*, 2012).

Due to the low computational costs of RANS models in comparison to DNS, RANS simulations are being used widely in the industry for attached boundary layer cases. However, RANS models cannot predict the turbulent separated flows in complex cases accurately, owing to the fact that the RANS model tries to model the entire turbulent spectrum with statistical time-averaging (Wang *et al.*, 2021).

Large Eddy Simulations (LES) can resolve most of the turbulent energy directly. Nonetheless, in LES simulations an exceedingly fine mesh is required near the wall. These conditions lead to large computational resources. Even with the advancements of technology and computation power, LES simulations are still not practical for flows with a very high Reynolds number (typically 10^5 or higher) and complex geometry (Guseva *et al.*, 2017; Armstrong *et al.*, 2022).

Over the last three decades, researchers tried to come up with a solution to the previously mentioned contradiction. Therefore, several hybrid turbulence models have been put forward to secure LES precision combined with RANS modeling (see Figure 2.1).

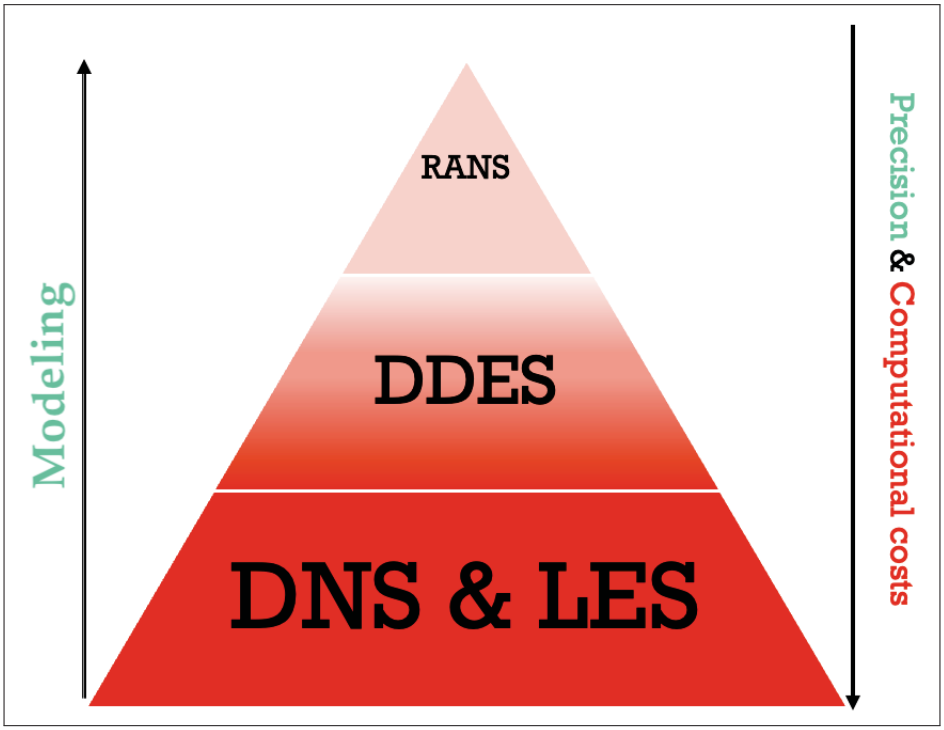

Figure 2.1 Characteristics of DDES simulations in compared to RANS and DNS/LES

In 1997, Spalart *et al.* (1997a) proposed a Detached Eddy Simulation method called DES97, in which the transition from RANS to LES explicitly depended on the grid resolution. Following this paper, nine years later, Spalart *et al.* (2006) proposed Delayed Detached Eddy Simulations (DDES), building the blocks of the idea of the shielding of the boundary layer proposed later by Menter, Schütze & Gritskevich (2012).

Due to the strong natural Kelvin-Helmholtz (KH) instability, the transition from fully modelled turbulence in attached boundary layers by RANS to turbulent separated shear layers tends to be resolved by LES. However, in practice, the problem with these methods was the gray area issue which was addressed in the first paper (Spalart *et al.*, 1997a). This issue corresponds to the delay in the transition from RANS to LES. Later Spalart *et al.* (2006) investigated the origin of this issue.

To minimize the effect of gray area issue in DDES, Shur *et al.* (2015) proposed a promising new approach called Enhanced Delayed Eddy Simulations (EDDES) with "Shear Layer Adapted" strategy. The criteria for this methodology is based on twisting the computational grids (to smaller cells) across the shear layer in the same direction. It has been demonstrated in Shur *et al.* (2015) that in this methodology, by replacing the local grid spacing Δ_{max} with the newly offered strategy of Δ_{SLA}, leads to an accelerated unlocking of Kelvin-Helmholtz instability, subsequently, a faster "second transition" to 3D turbulence.

A detailed background of the physical components of the SLA strategy is available in Shur *et al.* (2015). With the direction of the vorticity vector ($\overrightarrow{\mathbf{n}}\omega$) and a cell with $\overrightarrow{\mathbf{r}}$ as center and $\overrightarrow{r_n}$ with n representing the shape of the cells (n=1...8 for hexahedral cells), the first definition is:

$$\tilde{\Delta}_{\omega} = \frac{1}{\sqrt{3}} max|I_n - I_m| \tag{2.11}$$

where $I_n = n_\omega \times r_n$ (n_ω) is the unit vector aligned with vorticity vector × the position vector of the n-th vertex from the grid cell of interest (r_n). Here $\tilde{\Delta}_{\omega}$ represents the diameter of the cross product points divided by $\sqrt{3}$. The value of $\sqrt{3}$ is the approximation for Δ_{max} recovering turbulence computed on the cubic cells. With this methodology, for example, a free shear layer

flowing in the x-y direction that has a much larger grid spacing in the span-wise direction, $\tilde{\Delta}_\omega$ reduces to $\frac{1}{\sqrt{3}}(\Delta x^2 + \Delta y^2)^{\frac{1}{2}}$. However, replacing Δ_{max} with $\tilde{\Delta}_\omega$ is not enough to accelerate the transition to resolved turbulence (Guseva *et al.*, 2017). In the SLA methodology, $\tilde{\Delta}_\omega$ essentially measures the variation in the direction of vorticity across a given grid cell by comparing the direction of the vorticity vector, $\overrightarrow{n\omega}$, at each vertex of the grid cell, represented by $\overrightarrow{r_n}$ (Shur *et al.*, 2015). For each pair of vortices, a quantity I_n - I_m is computed, which signifies the difference in the cross products of the vorticity vector and the position vectors of these vortices. The maximum absolute difference amongst these quantities, normalized by $\frac{1}{\sqrt{3}}$, gives us $\tilde{\Delta}_\omega$. This indicates the maximum relative shift in the direction of vorticity across the cell, essentially representing how homogeneous the vorticity is within the cell. This measure is useful in refining the calculation of grid scales, allowing for the more accurate capture of turbulent structures. Specifically, in flows where the grid spacing varies significantly in different directions, $\tilde{\Delta}_\omega$ provides a more robust and flow-adaptive grid scale estimate (Shur *et al.*, 2015).

Therefore, an additional modification to the sub-grid length scale is required. The additional modification proposed by Shur *et al.* (2015) is called the Vortex Tilting Measure (VTM) that is defined by a cross product of inviscid vorticity-evolution ($S.\omega$) with the vorticity vector as:

$$VTM = \frac{\sqrt{6}|(S.\omega) \times \omega|}{\omega^2\sqrt{3tr(S^2) - [tr(S)]^2}} \tag{2.12}$$

In this equation ω is the vorticity, S is the strain tensor and tr(.) is the trace. By using the VTM equation, the definition of $\tilde{\Delta}_\omega$ can be further deduce to:

$$\Delta_{SLA} = \tilde{\Delta}_\omega F_{KH}(< VTM >) \tag{2.13}$$

Here, the function of the non-dimensional F_{KH} (Shur *et al.*, 2015) is to unlock the Kelvin-Helmholtz instability in the early stages of the shear layers. It is defined as:

$$F_{KH}(< VTM >) = max\left\{F_{KH}^{min}, min\left\{F_{KH}^{max}, F_{KH}^{min} + \frac{F_{KH}^{max} - F_{KH}^{min}}{a_2 - a_1}(< VTM > -a_1)\right\}\right\} \tag{2.14}$$

In this equation, F_{KH}^{max}= 1.0 and F_{KH}^{min} = 0.1. The two constants of a_1 and a_2 are 0.15 and 0.3 respectively. Which will give:

$$F_{KH}(< VTM >) = max\left\{0.1, min\left\{1, 0.1 + \frac{1-0.1}{0.3-0.15}(< VTM > -0.15)\right\}\right\} \tag{2.15}$$

As for EDDES formulations, this definition implies only a partial replacement of the Δ_{max} with Δ_{SLA}

$$\Delta = min\{max[C_w d_w, C_w \Delta_{max}, \Delta_{wn}], \Delta_{max}\} \tag{2.16}$$

where C_w is the empirical constant and equals to 0.15 and Δ_{wn} is the grid spacing normal to the wall. That being the case, the new definition is,

$$\Delta = min\{max[C_w d_w, C_w \Delta_{max}, \Delta_{wn}], \Delta_{SLA}\} \tag{2.17}$$

The interesting thing about this methodology is that the computational cost of simulations using these definitions will not exceed two percent of DDES simulations (Guseva *et al.*, 2017). Molina *et al.* (2019) implemented the Delayed Detached Eddy Simulation (DDES) model in SU2. Its foundation is the SA model and its variations. Different recently proposed modifications of the sub-grid scale (SGS) were made to handle unstructured grids in order to reduce the gray area issue. These modifications include the Vorticity Adapted SGS, and the Shear-Layer Adapted (SLA) SGS (Shur *et al.*, 2015; Guseva *et al.*, 2017).

For the final part of this section, our goal is to define the used terms throughout this thesis to enhance the reader's comprehension. In particular, we will explore the terminology covering aerodynamic coefficients, including pressure, skin friction, drag, and lift coefficients. Additionally, we will explain the concepts of CFL and y^+ for a comprehensive understanding of the subject matter (from Blazek, J. (2015)).

Pressure coefficient (C_P) is a dimensionless number which describes the relative pressures throughout a flow field in fluid dynamics. It is defined by the equation:

$$Cp = \frac{P - P_0}{0.5 * \rho * U_\infty^2} \tag{2.18}$$

where: P is the pressure at the point in the flow field, P_0 is the reference pressure , ρ is the fluid density, U_∞ is the free-stream velocity.

The skin friction coefficient (C_F) is a measure of the resistance of a fluid directly adjacent to the boundary of a body moving through it. It is defined as:

$$C_F = \frac{\tau}{0.5 * \rho * U_\infty^2} \tag{2.19}$$

where: τ is the wall shear stress, ρ is the fluid density, U_∞ is the reference velocity.

The lift coefficient (C_L) is a dimensionless number that characterizes the lift generated by an object in a fluid flow. It is defined as:

$$C_L = \frac{L}{0.5 \cdot \rho \cdot U_\infty^2 \cdot A} \tag{2.20}$$

where L is the lift force acting on the object, ρ is the fluid density, U_∞ is the free-stream velocity, and A is the reference area.

The drag coefficient (C_D) is a dimensionless number that quantifies the drag experienced by an object moving through a fluid. It is defined as:

$$C_D = \frac{D}{0.5 \cdot \rho \cdot U_\infty^2 \cdot A} \tag{2.21}$$

where D is the drag force acting on the object, ρ is the fluid density, U_∞ is the free-stream velocity, and A is the reference area.

The CFL (Courant-Friedrichs-Lewy) number is defined as the ratio of the product of the characteristic velocity (U) and the time step size (Δt) to the characteristic length or grid spacing (Δx). The equation for the CFL number is:

$$CFL = \frac{U \cdot \Delta t}{\Delta x} \tag{2.22}$$

The CFL number is used to determine the stability and accuracy of numerical methods for solving fluid dynamics equations. It sets a limit on the time step size based on the characteristic velocities and grid spacing to ensure stable and accurate simulations.

The y^+ value is a dimensionless parameter used in computational fluid dynamics (CFD) to describe the behaviour of fluid flow near a wall. It represents the non-dimensional distance from a cell center to the nearest wall, normalized by the local viscous length scale. The equation for the y^+ value depends on the specific definition of the viscous length scale (δ) used:

$$y^+ = \frac{u \cdot \delta}{\nu} \tag{2.23}$$

where u is the velocity magnitude at the cell center, δ is the viscous length scale, and ν is the kinematic viscosity of the fluid. The y+ value helps determine the appropriate treatment of the near-wall region in CFD simulations, such as selecting the turbulence model and the corresponding wall treatment, based on the grid resolution and the distance from the wall.

2.3 Numerical method in SU2

Below is a quick summary of the specifics of how the relevant numerical approaches are implemented in SU2. On unstructured meshes, the flow problems are numerically resolved using an edge-based data structure. The governing equations are discretized in space and time separately using the method of lines. The choice of various type of schemes for the integration of space and time is achieved by the decoupling of space and time. The finite volume method (FVM) is used to integrate space. A dual time-stepping method is utilised for calculations that are accurate in time (Economon *et al.*, 2016). At first we will take a look at the spatial integration

using the FVM, a dual grid with a typical edge-based structure and control volumes created using a median-dual, vertex-based approach is used to discretize partial differential equations (PDEs) Blazek, J. (2015). By joining the centroids, faces, and edge-midpoints of all cells sharing the specific node, dual control volumes are created. The semi-discretized, integral version of a typical PDE (such as the RANS) is provided from the divergence theorem and integration of the governing equations across a control volume. For example:

$$\int_{\Omega_i} \frac{\partial U}{\partial t} d\Omega + \sum_{j \epsilon N(i)} (\hat{F}_{c_{ij}} + \hat{F}_{v_{ij}}) \Delta S_{ij} - Q|\Omega_i| = \int_{\Omega_i} \frac{\partial U}{\partial t} + R_i(U) = 0, \tag{2.24}$$

where $R_i(U)$ is the numerical residual that represents the integration of the spatial factors and U is a vector of state variables. Q is a source term, while $\hat{F}_{cij}$ and $\hat{F}_{vij}$ are the projected numerical approximations of the convective and viscous fluxes, respectively. ΔS_{ij} is the portion of the face that corresponds to edge ij, Ω_i is the volume of the control volume, and $N_(i)$ is the collection of nodes that are immediately adjacent to node i. Figure 2.2 shows these symbols in an imaginary 2D grid.

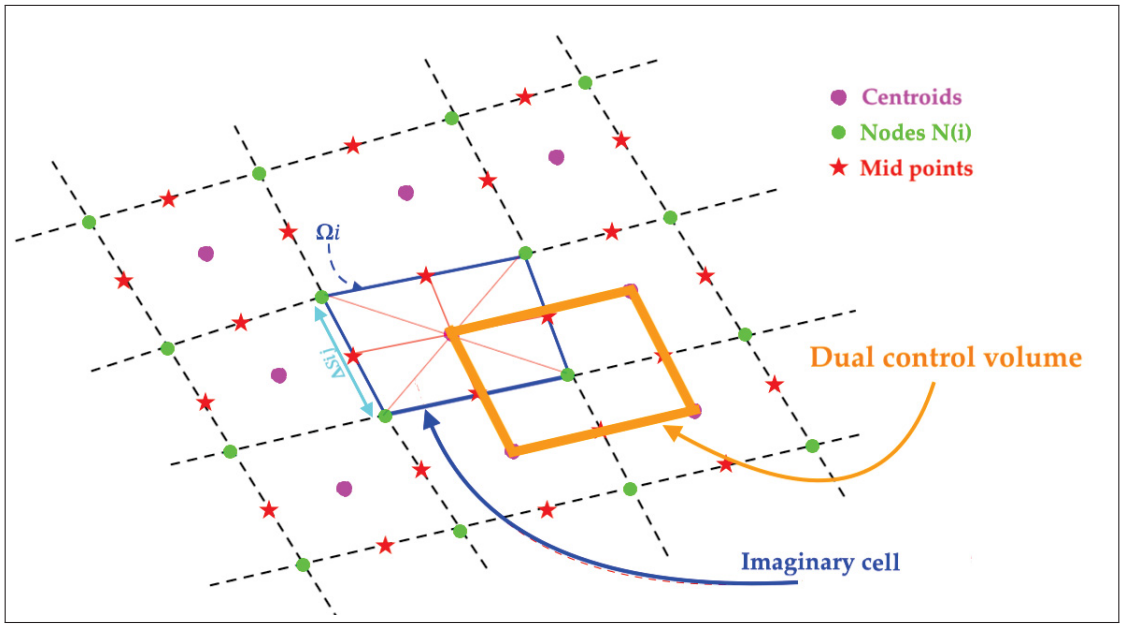

Figure 2.2 A schematic diagram of a finite volume cell illustrating the relevant entities, the control volume Ω_i, the faces and edge-midpoints, the centroids, and the adjacent nodes $N(i)$

SU2 evaluates the convective and viscous fluxes at the middle-edge (red stars) of each cell. These fluxes are then calculated by the numerical solver looping through all of the edges in the original mesh (Economon *et al.*, 2016). Then they are integrated to determine the residual at each node in the numerical grid. With SU2, the convective fluxes are discretized using upwind scheme. The evaluation of the viscous fluxes with the finite volume approach requires the flow quantities and their first derivatives at the control volume faces. First, using the weighted least-squares, the gradients of the flow variables are estimated at each grid node to determine the gradients at the cell faces. Source terms are roughly developed within each cells using piece-wise constant reconstruction. For the time integration, it is necessary to evaluate $R_i(U)$ at time t^{n+1}(implicit methods) for the equation 2.24 to be valid over the entire time range. The following linear system must be solved to determine the solution update, concentrating on the implicit integration.

$$\left(\frac{|\Omega_i|}{\Delta t_i^n}\delta_{ij} + \frac{\partial R_i(U^n)}{\partial U_j}\right).\Delta U_j^n = -R_i(U^n), \tag{2.25}$$

where $\Delta U_i^n = U_i^{n+1} - U_i^n$

To resolve equation (2.25), the SU2 framework has various linear solvers implemented. The main techniques for the linear solvers that we are using is the Generalized Minimal Residual (GMRES) approach uses a vector in a Krylov subspace to approximate the solution with minimal residual. It uses the Arnoldi iterative algorithm to find the vector in the Krylov subspace which best approximates the solution ΔU^n, minimizing the residual in the process (Economon *et al.*, 2016).

2.4 Vortex Identification Techniques

In fluid dynamics, a vortex is a region where the fluid rotates around an axis line that may be either straight or curved. Vortices can be identified by their swirling motion and are typically characterized by a low-pressure core. We will use three identification techniques in section 3.4 to detect the possible vortices after the hump. To have a clearer understanding of these methodologies, we present the mathematical equations of these techniques here. These techniques are :

1. Q-criterion
2. λ_2 criterion
3. Swirling Strength (λ_{ci}^2)

The vortices are recognized as flow regions with a positive second invariant of the velocity gradient tensor, denoted by 'Q', as determined by the Q-criterion proposed by Hunt, J. C. R. and Wray, A., and Moin, P (1988) Another requirement is that the pressure in the eddy zone should be lower than the surrounding pressure. According to Chakraborty *et al.* (2005), "in an incompressible flow, Q is a local measure of the excess rotation rate relative to the strain rate". $\overrightarrow{v}(\overrightarrow{\mathbf{x}}, t)$.

$$\nabla v = S + \Omega \tag{2.26}$$

where

$$S = \frac{1}{2}\left(\Delta v + (\Delta v)^T\right) \tag{2.27}$$

is the rate of strain tensor and:

$$\Omega = \frac{1}{2}\left(\Delta v - (\Delta v)^T\right) \tag{2.28}$$

and Ω is the vorticity tensor. A vortex is discovered when the difference between the vorticity and strain is positive. In other words:

$$Q = \frac{1}{2}(|\Omega|^2 - |S|^2) > 0 \tag{2.29}$$

where the rate of strain is dominated by the vorticity tensor Euclidean norm. When simulating simple flows, particularly in two dimensions, contours of $Q > 0$ are frequently employed to identify vortices, which are considered to be regions in which local rotation predominates over local strain tensor (equation 2.29). In simple flows, the areas with positive Q are referred to as vortex zones. Practical implementation frequently uses contours that are a specified percentage of the maximum Q value, in complicated 3D or turbulent experimental flows.

Another technique for identifying vortices is called λ_2, which was developed by Jeong & Hussain (1995). It is well-liked because of how consistently it can find vortices and how straightforward

the computation processes are. The same as Q-criterion, S indicates the rate-of-strain tensor and Ω rate-of-rotation tensor. By excluding the unstable irrotational straining and viscous effects the symmetric portion of the gradient of the incompressible Navier-Stokes equation can be written as:

$$S^2 + \Omega^2 = -\frac{1}{\rho}\nabla^2 p \tag{2.30}$$

Therefore, $S^2 + \Omega^2$ represents the pressure minima. This matrix has precisely three real eigenvalues because it is real and symmetric. The following eigenvalues are calculated and arranged in descending order: $\lambda_1 \geq \lambda_2 \geq \lambda_3$. Therefore the regions with $\lambda_2 < 0$ indicate possible location of a vortex (Dong, Yan & Liu, 2016) .

The Swirling Strength (λ_{ci}^2) was initially suggested by Zhou *et al.* (1999) for the shear flow problem. It is calculated using the $U = \nabla v$ velocity gradient, which transforms into a Jacobian matrix of the velocity field. The velocity gradient can be diagonalized as follows for a rotating flow:

$$U = [u_r, u_+, u_-] \begin{pmatrix} \lambda_r & 0 & 0 \\ 0 & \lambda_+ & 0 \\ 0 & 0 & \lambda_- \end{pmatrix} [u_r, u_+, u_-]^{-1}, \tag{2.31}$$

where $\lambda_\pm = \lambda_{cr} \pm i\lambda_{ci} \in C$ (complex numbers) and $\lambda_r \in R$ (real numbers) are the corresponding eigenvalues that make up the change of basis matrix P, and $u_\pm$ and u_r are the eigenvectors of U that make up the eigenvalue of the middle matrix. Two times the imaginary part of the complex eigenvalues is how we define the Swirling Strength (λ_{ci}^2) (Zhou *et al.*, 1999).

$$\lambda = 2\lambda_{ci} \tag{2.32}$$

In this chapter, we have defined the mathematical equations of the flow, including the original and negative SA turbulence models, and introduced the concepts of the SLA strategy. Then, we explored the configuration and functionality of SU2. Finally, we identified the vortex identification techniques that will use in the next section. More specifically, we will employ the EDDES solution to capture vortices occurring after the hump of the WMH. For vortex

identification, we will employ the Q-criterion, λ_2, and λ_{ci}^2. To evaluate these identification techniques quantitatively, we will analyze the number of vortices in different sections following flow separation. This analysis will provide valuable insights into the characteristics and behaviour of the vortices in our simulation.

CHAPTER 3

RESULTS

3.1 Introduction

From the literature review, in chapter 1 we have concluded that the EDDES method can predict the turbulent flow structure over the Wall Mounted Hump (WMH). However, these structures have not yet been investigated with vortex detection methods for this test case.

In chapter 2, we have defined the mathematical and numerical settings employed for this thesis. More specifically, a summary of the approaches by the numerical solver as well as different definitions used in this work were explained. Then, we defined various vortex identification methods.

In this chapter, Section 3.2 will present a study based on RANS simulations with SU2 solver on the NASA WMH grids. To be more precise, we shall define the test case first. By examining the distribution of the pressure and skin friction coefficient along the wall, we shall determine how the grid density affects the results. We will contrast our findings with those obtained from similar numerical settings and experimental data after examining the impact of the grid on the solution. Finally, by finding the errors in aerodynamic coefficients, and a Grid Convergence Index study of the grids, we choose the grids for the EDDES section. In section 3.3, after defining the test cases in more depth, we will do a grid study on three separate grids with two different span-wise sizes (L_Z). We will look at the time and space-averaged solution to pinpoint the possible reason for the late transition of RANS to LES in hybrid models. We will use vortex identification, with the different techniques presented in chapter 2 on the EDDES simulations in the final section (3.4). We shall observe the variations in vortices in the various grids and time steps. Finally, we will determine the number of vortices in the WMH channel at various time steps in different sections. We will use the EDDES data from section 3.3.

3.2 RANS simulations

Examining the effect of grid resolution on the separation length is the main goal here. The inaccuracy caused by the selection of grids will be examined and quantified. More specifically, on the WMH velocity field and aerodynamic coefficients, we shall observe the impact of grid resolution. We will compare the results with similar findings in the literature with a simillar configuration to ensure the correct turbulence model is implemented.

Figure 3.1 represents the layout of the WMH. The WMH measures $l_x = 10.39m$ in length. The depth is $l_y = 1m$, while the height is $l_z = 0.90905m$. With a Mach of 0.1 (34.3 m/s), the flow enters the WMH channel and reaches the hump at x=0 m. Based on the chord length of 1(m), the Reynolds number is 936000.

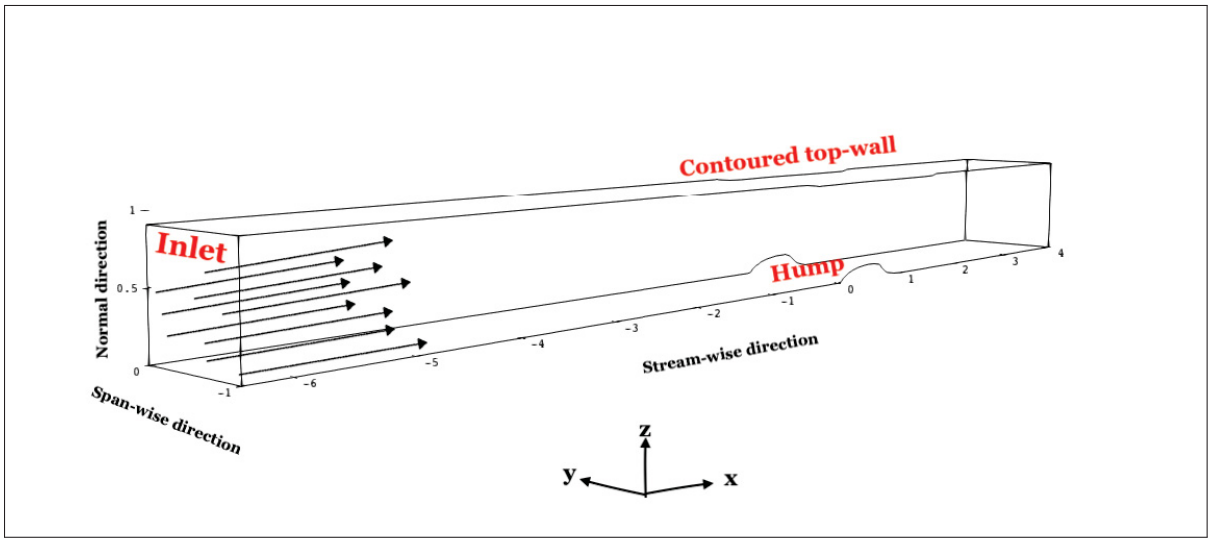

Figure 3.1 Scheme of the WMH test case

Figure 3.2 represents the boundary conditions of the WMH. At the inlet, which is located at x = -6.39 m, a uniform flow enters the WMH channel and hits the hump at position zero in the direction of the stream. A total temperature and pressure of 298.92 k and 42847.65 Pa, respectively, are imposed through the inlet border with no angle of attack (flow is in the x-axis only). The imposed static pressure at the exit is 42533.63 Pa. The top wall has an inviscid

slip-wall condition. Whereas the front face and back face walls have symmetry plane conditions. Since we are solving the compressible RANS equations, the bottom wall has adiabatic wall conditions, flow adheres to the wall. Thus, the heat flux is equal to 0 J/m^2, and the velocity on the bottom wall is 0 m/s.

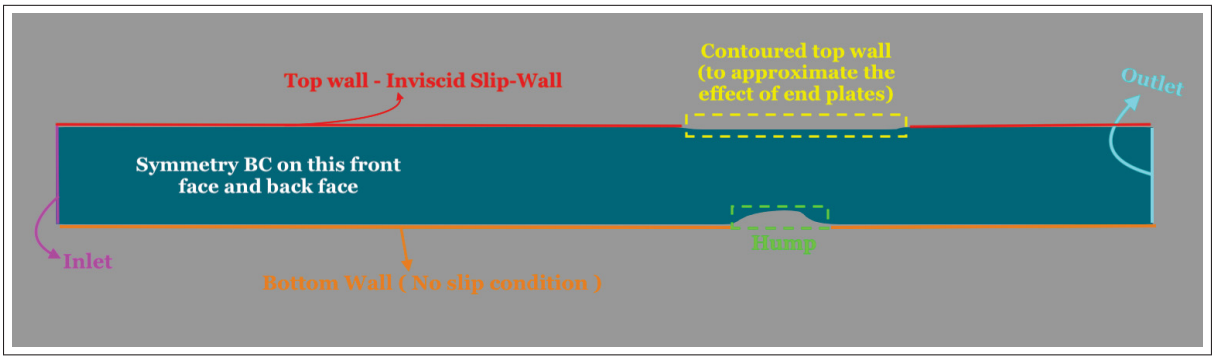

Figure 3.2 WMH simulation model displaying the boundary conditions

Various characteristics of these grids are displayed in Table 3.1. Δ_x and Δ_z , respectively, represent the minimum distance between the nodes in the stream-wise direction and the nodes normal to the wall. It is important to note that the values for Δ_x and Δ_z are approximations and were calculated in the downstream side of the hump. Figure 3.3 show the area where the Δ_x and Δ_z are evaluated. The reason behind choosing this location is to find the minimum values of Δ_x and Δ_z in the computational domain. These grids are numbered from coarse to fine.

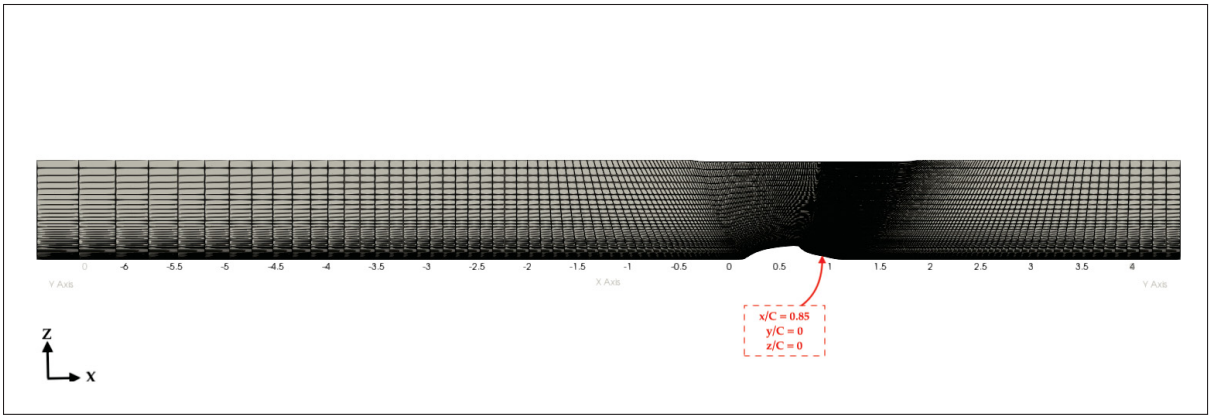

Figure 3.3 Location of the area where Δ_x and Δ_z is evaluated

Table 3.1 Characteristics of NASA grids for the WMH

No.	n_x	n_y	Δ_x	Δ_z	**Total cells**
1	103	28	9.3×10^{-3}	6.6×10^{-5}	2,754
2	205	55	4.7×10^{-3}	3.3×10^{-5}	11,016
3	409	109	2.3×10^{-3}	1.6×10^{-5}	44,064
4	817	217	1.1×10^{-3}	8.3×10^{-6}	176,256
5	1633	433	5.0×10^{-4}	4.1×10^{-6}	705,024

We will use grids without plenum in this thesis. These grids are displayed in Figure 3.4 in the same sequence from coarse to fine as in Table 3.1. In all of these meshes, the density tends to increase in the normal direction as it gets closer to the wall. Additionally, this tendency of increasing mesh density can be seen over the hump in the x-direction as well.

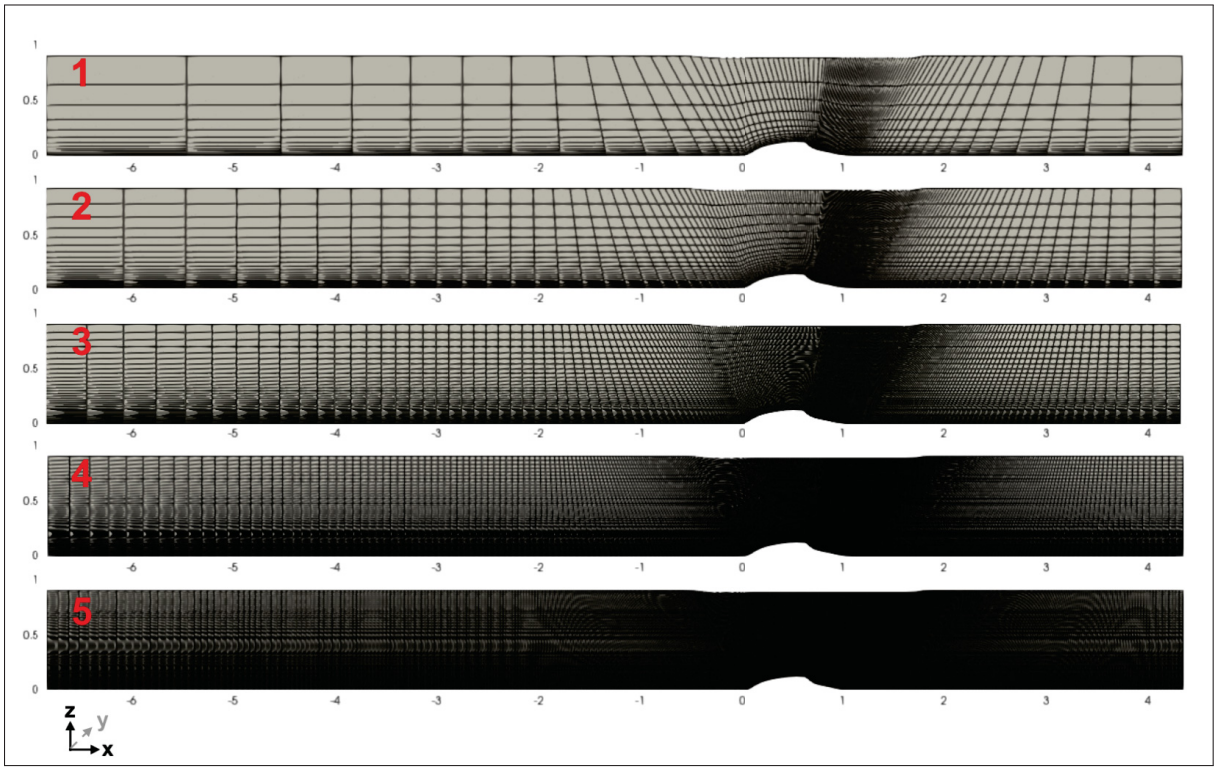

Figure 3.4 Front view of the NASA CFDVAL2004 workshop grids (XZ)

Table 3.2 shows the computational resources spent on each grid. The problem is handled iteratively with a maximum CFL of 5 with the time adaptive strategy to reach a steady state solution. The number of iterations for each grid is different since it took more time to get a converged solution for denser grids. Following this we will compare the (ρ) and $\tilde{\nu}$ residuals for each grid. For our RANS simulations, the space-numerical integration uses the SLAU2 for the inviscid terms of the RANS equation (Kitamura, 2016). A weighted least square interpolation method is used for spatial gradient interpolation (Hu *et al.*, 2019). A second-order MUSCL scheme with the Venkatakrishnan limiter stabilizes the convective flux calculations (Venkatakrishnan, 1993). An Euler implicit scheme is used for time discretization (Hirsch, 2007). The linear system is solved with FGMRES and a minimum error of 1×10^{-10} or 20 iterations (DeVries, Iannelli, Trefftz, O'Hearn & Wolffe, 2013). For the negative Spalart Allmaras turbulence equation, a scalar upwind is used for the inviscid terms. A second-order integration in space using the MUSCL scheme employs the same Venkatakrishnan slope-limiting method (Venkatakrishnan, 1993). The problem is solved iteratively using a constant CFL of 5.

Table 3.2 Computational resources of the simulations on Niagara cluster

No.	**Grid**	**Total iterations**	**Time of simulation**	**CPUs**
1	103×28	130,000	00hr:17min	40 (1 node)
2	205×55	311,200	01hr:31min	40 (1 node)
3	409×109	799,999	16hr:25min	40 (1 node)
4	817×217	696,051	40hr:23min	40 (1 node)
5	1633×433	439,230	89hr:54min	40 (1 node)

The degree of convergence of the numerical solution is measured by the density residuals for these CFD simulations. The solution improves as the residuals decrease. High value of the density residual means that the numerical solution is not converged, which can be due to a mistake in the numerical formulation, a lack of grid resolution, improperly selected boundary conditions, or numerically unstable flows. When the residuals go down at least 3 or 4 degrees of

magnitude, we can conclude that the solution is converged (Blazek, J., 2015). Figure 3.5a and 3.5b shows the evolution of ρ and ($\tilde{\nu}$) residuals for the five grids we have used. We can observe that as the level of grid density increases, it takes more iteration for the solver to converge to 10^{-9} (which is the order of magnitude below the starting 10^{-5}). However, the number and limit of iterations seem sufficient for these simulations.

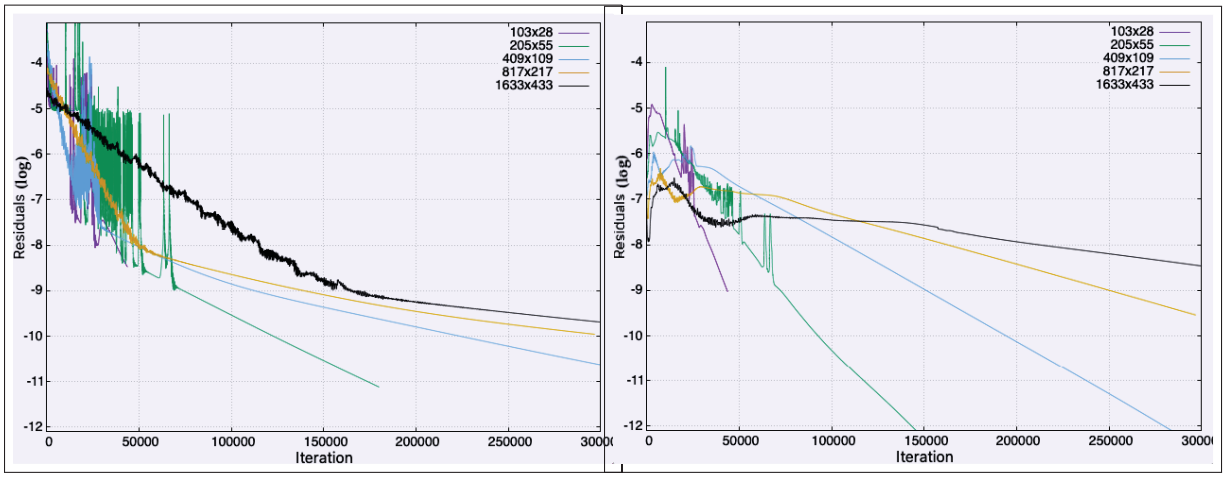

a) Density (ρ) residuals

b) $\tilde{\nu}$ residuals

Figure 3.5 Comparison of density and $\tilde{\nu}$ residuals between the five simulations (5 grids)

The 2D velocity distribution will be our first point of focus for post-processing. To examine the separation and reattachment location more precisely, we will zoom in the streamlines downstream of the hump.

The velocity distribution in the channel of the WMH is depicted in Figure 3.6 as the first step. As previously mentioned, the flow enters the WMH channel with a velocity of 34.3 m/s (Ma=0.1). As the area narrows, speed will increase over the hump (yellow). Just downstream of the hump, low velocity is visible (black). This figure shows the general characteristics of physical flow. In other words, the flow is not acting oddly or unrealistically.

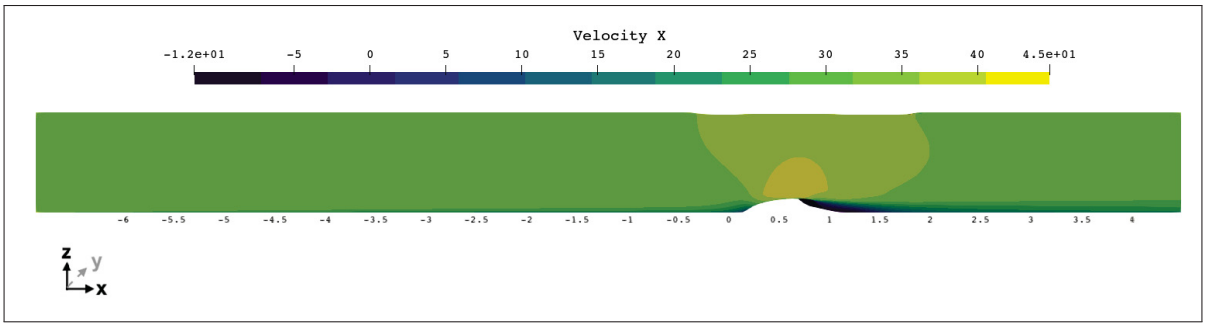

Figure 3.6 Velocity-x distribution on the channel of the WMH for the fourth grid (817x217)

With a closer look at the velocity distribution in the separation zone, we can better identify in Figure 3.7 where the flow separates from the wall and where it reattaches. A tangential line to the instantaneous velocity direction is referred to as a streamline (in white in Figure 3.7). We may picture the movement of a tiny marked fluid element along these white lines. The fluid re-circulation, separation, and reattachment points can all be seen clearly in this way.

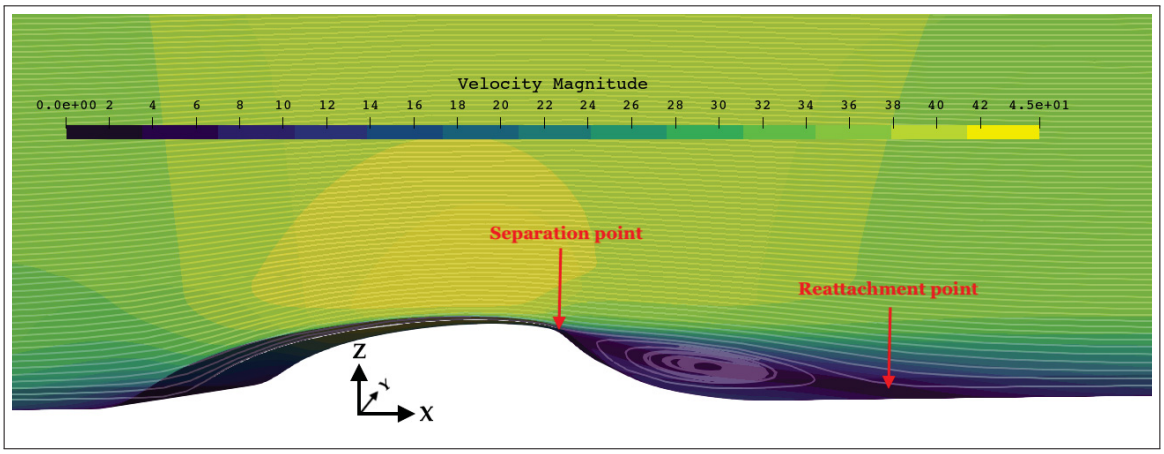

Figure 3.7 A closer look at the separation and reattachment point of the fourth grid (817x217)

The pressure coefficient on the WMH 2D cut is shown in Figure 3.8. This representation is from the results of the fourth grid (817x217). The pressure coefficient iso-contours are shown with white lines. As the velocity increases, we can see that the pressure coefficient just over the hump

has a lower value than in other areas of the computational domain as expected according to the Bernoulli's equation.

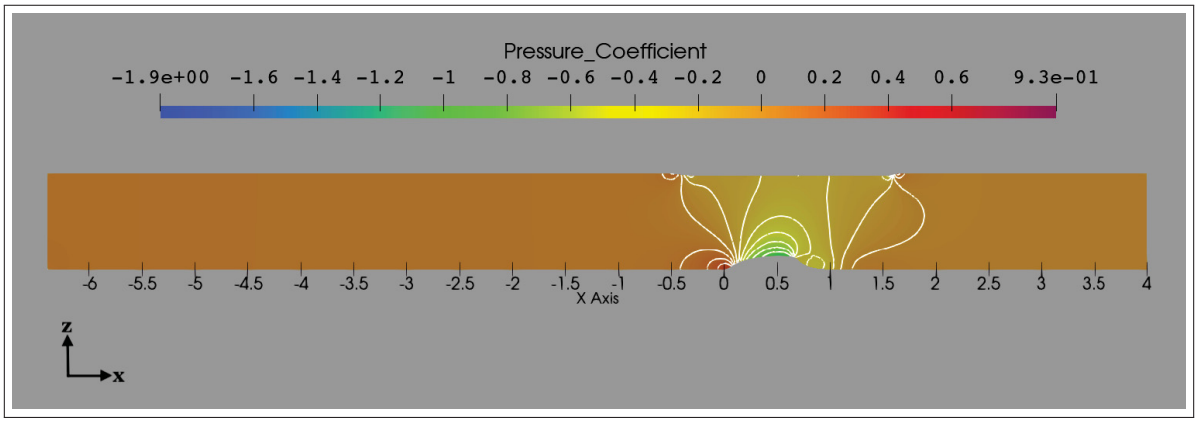

Figure 3.8 Distribution of pressure coefficient on the mid-section plane of the WMH for the fourth grid (817x217)

The pressure coefficient distribution along the WMH wall is shown in Figure 3.9. In the first step, we will compare the results from different grids. As we can see, before the flow encounters the hump at point x/c = 0, all grids have identical values with an error of less than 0.01 %. In this graph, we can also see the locations of the flow critical stages. Some differences are visible on the coarser grids as the flow enters the low-pressure region, where the velocity is high due to a reduction in area (around x/c=0.5). The highest inaccuracy can be visually observed close to the flow separation. We note that the difference between the grids also decreases as the pressure coefficient rises once more and gets closer to the free stream value (where the flow reattaches). We shall thoroughly compare these grids reattachment lengths at the end of this section.

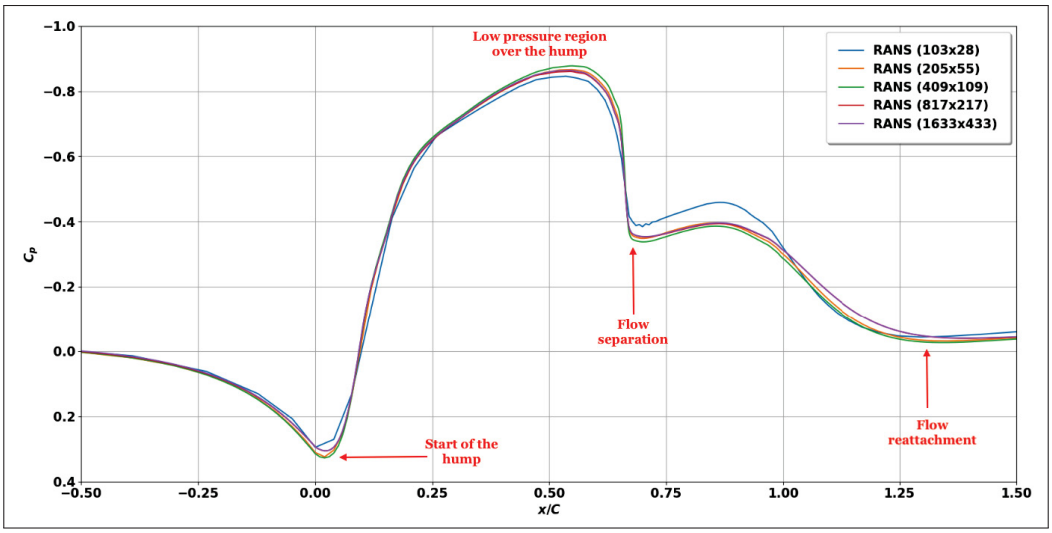

Figure 3.9 Distribution of pressure coefficient along the WMH wall (RANS) results shifted to have a start point at the location of zero at x/c = -0.5 (103×28 shifted by -0.035, 205×55 shifted by -0.02 and the rest with -0.015)

The second goal here is to quantify the error induced by the grids (shown in Figure 3.9). To accomplish this, we will compare each grid to the finest mesh, which will be used as the reference point. The grid-induced error of these grids compared with the finest grid (1633×433) is demonstrated in Table 3.3. We will use the Mean Absolute Error (MAE) and Root Mean Squared Error (RMSE) (Hodson, 2022) to get the difference between the pressure coefficients of the first four grids when compared with the fifth grid.

For each grid, we have sets of x-values x = $(x_1, x_2, \ldots, x_n)$ and y-values $(y_1, y_2, \ldots, y_n)$ which corresponds to the x/c and pressure coefficients respectively. The MAE between the pressure coefficients of two grids will be calculated by:

$$MAE = \frac{1}{n} \sum_{j=1}^{n} \left| y_i - y_i^* \right| \tag{3.1}$$

where the y^* is the pressure coefficient of the reference grid. This method shows the average magnitude difference between the pressure coefficient values of two grids without considering

the sign. The functions originally are used to get the difference between actual values and estimated values. However we have modified it to get the difference between our data sets.

The RMSE is defined as:

$$RMSE = \sqrt{\frac{1}{n}\sum_{j=1}^{n}(y_i - y_i^*)^2} \tag{3.2}$$

The RMSE also represents the average magnitude of the differences. However, it gives more weight to the higher differences as it squares them. Therefore, it is more sensitive to errors compared to the MAE. Additionally, because these approaches compute the pressure coefficient difference, which is a dimensionless value, they are dimensionless as well (Hodson, 2022). Table 3.3 indicates that by refining the mesh MAE will gradually decline, indicating that the grid refinement has a positive effect on C_P for these simulations.

Table 3.3 MAE and RMSE induced by each grid compared to the finest grid (1633×433) for the C_p curve

No.	**Grid**	**MAE**	**RMSE**
1	103×28	0.0283	0.0335
2	205×55	0.0098	0.0124
3	409×109	0.0140	0.0175
4	817×217	0.0013	0.0016

The SU2 solver and the CFL3D solver (Siggeirsson & Andersson, 2019) are compared in Figure 3.10. The MAE and RMSE of C_p between the results of the SU2 and the CFL3D solvers for the 817×217 grid is 0.0166 for both approaches. Therefore, we can conclude that the implementation of the SA turbulence model agrees with the literature. The difference between the SU2 C_p and the experiment is MAE = 0.0514 and RMSE = 0.0692. We can see that both CFD codes exhibit the same limitations when compared to the experimental results.

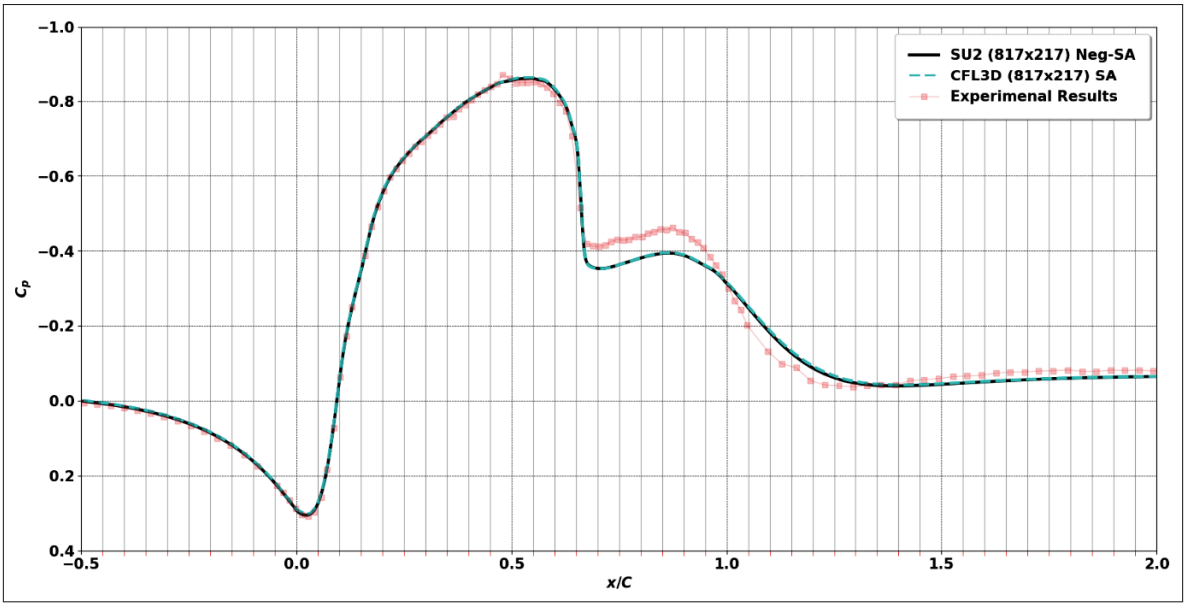

Figure 3.10 Validation of RANS results with the results available in the NASA CFDVAL2004 workshop for the WMH (resuts of SU2 and CFL3D solver is shifted by C_p = - 0.015 to better match with the experimental results of Greenblatt *et al.* (2006))

The distribution of the x-component of the skin friction coefficient on the bottom wall of the WMH is illustrated in Figures 3.11 and 3.12. The changes in the skin friction coefficient between each grid are shown in the first Figure (3.11). The graph shows the key points previously explained for the pressure coefficient in red (Figure 3.9). This graph illustrates how the flow behaves physically. Skin friction will gradually rise as the flow reaches the hump, increasing the x-component. The value drops to negative numbers just at the location of separation. Then rises to positive numbers as the flow re-attaches. We can see a decline in C_F curves from x/c = -0.5 to 0 as the fluid particles hit the hump at location zero. The area narrows down from x/c = 0 until the separation location around x/c=0.6, and the C_F increases. Just after this point, due to flow separation, we see a sudden drop in skin friction coefficient going into negative values until it re-attaches to the wall and goes into positive values.

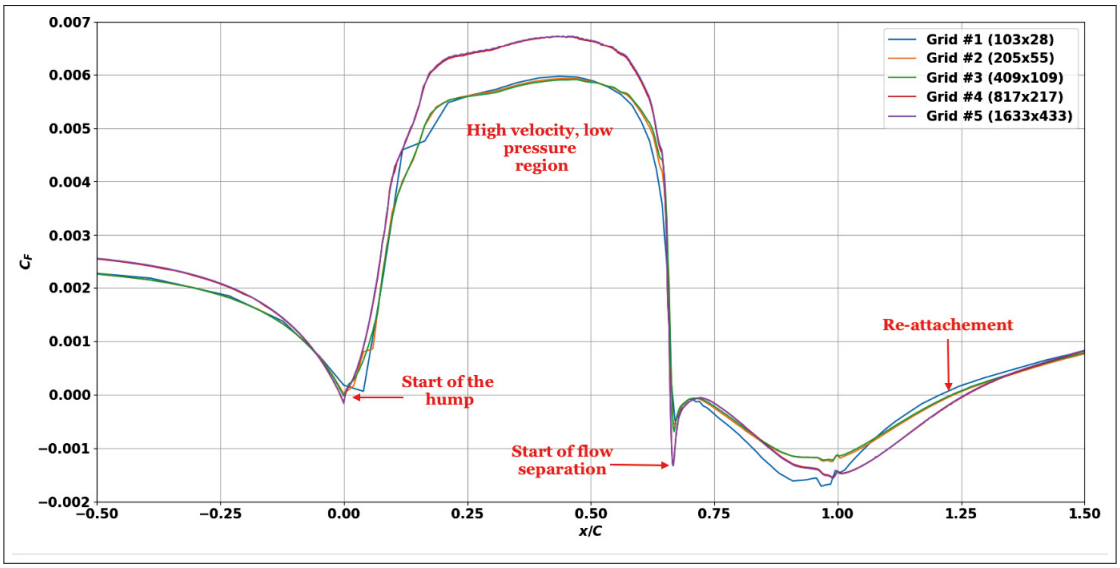

Figure 3.11 x-component of the skin friction coefficient distribution along the WMH bottom wall compared between the five simulations (5 grids)

We have conducted the same study on the effect of grids on the results as we did for the pressure coefficient. This time we see that the variations between the first three grids (Grid #1 to Grid #3) are much more significant in comparison to the last two grids (Grid #4 and #5). The method is identical as before, using the MAE and RMSE methods, we will determine the error between the first four grids and the finest grid.

Table 3.4 MAE and RMSE induced by each grid compared to the finest grid (1633×433) for the C_F curve

No.	Grid	MAE	RMSE
1	103×28	0.00034	0.00043
2	205×55	0.00029	0.00038
3	409×109	0.00028	0.00039
4	817×217	0.00012	0.00031

Figure 3.12 compares the results from the NASA turbulence webpage for the WMH with the results from the 817x217 grid. Before the low-pressure area and at the flow separation from the wall (between x/c=0.05 and x/c=0.4) the highest difference between the two numerical data sets are visible which could be due to different approaches to numerical approximation, turbulence modeling, and boundary layer resolution. The MAE and RMSE between the SU2 x-component friction coefficient and the CFL3D are 0.00004 and 0.00013 respectively. While comparing to the experimental results the difference increases to MAE= 0.00545 and RMSE = 0.01647. The main visible difference between the experimental results and the numerical solvers here is in the separation length. The separation in the experimental results starts at around x/c = 0.665 ± 0.005, and the reattachment is at 1.10±0.005. However, the numerical findings for the selected grid show a separation point of around ≈ 0.68 and a reattachment of approximately ≈ 1.25.

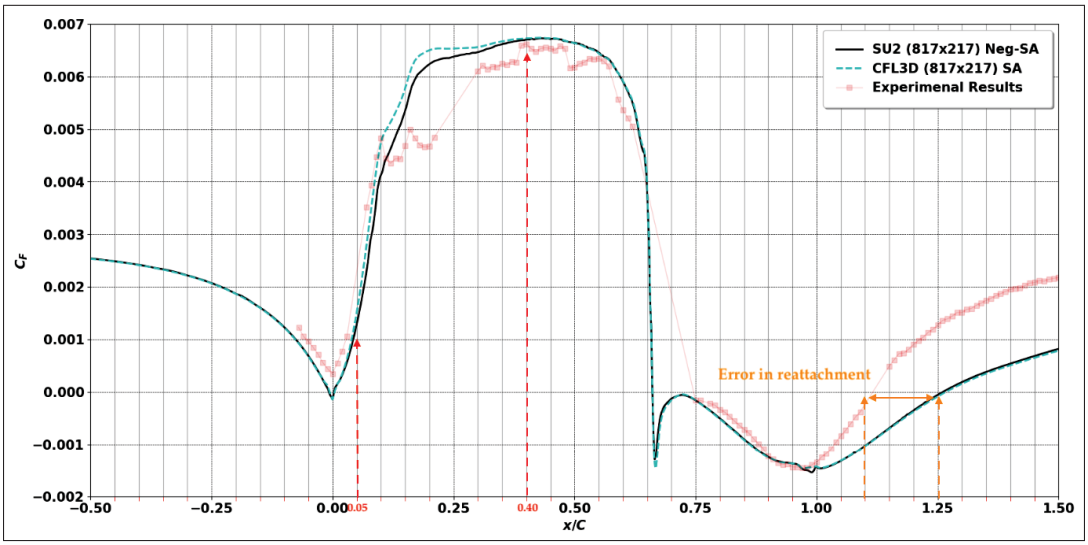

Figure 3.12 Comparison between SU2 and CFL3D solver for the skin friction coefficient on the bottom Wall of the WMH

Moreover, we shall compare the separation points and reattachment locations with the experimental findings. The C_F curves on the bottom wall of the WMH can be used to pinpoint the separation and reattachment sites. The criteria for identifying these sites is based on determining the location where the C_F value signs change. The first sign change will be the separation location (the location of x/c where C_F goes from a positive value to a negative value), the second

sign change will be the reattachment location (the location of x/c where C_F goes from a negative value to a positive value). Table 3.5 demonstrates the variation of separation and reattachment locations compared with the experimental results. Upon refining the mesh, the reattachment location and separation bubble length diverge from the experimental data. This indicates the complexities in the turbulence behaviour and the interaction with the wall, which may not be fully captured by the numerical models, especially in finer meshes that resolve more detailed flow features.

Table 3.5 Separation and reattachment locations of the WMH compared with the experimental data of Greenblatt *et al.* using the C_F values

Simulation	**Separation loc(x/c)**	**Re-attachment loc(x/c)**	**Separation bubble length(x/c)**
Experimental	0.665 ± 0.005	1.10 ± 0.005	0.435
103×28	0.667	1.246	0.579
205×55	0.664	1.246	0.582
409×109	0.661	1.235	0.574
817×217	0.661	1.263	0.602
1633×433	0.661	1.260	0.599

As the final step, we have conducted a grid study based on the values we have calculated for the pressure and skin friction coefficient to assess the robustness and uncertainty of our numerical simulations. The approach involves a spatial convergence analysis applied to our unstructured 2D grids. The Grid Convergence Index (GCI) proposed by Roache (1994) serves as an estimate for the upper bound of discretization error. The order of grid convergence (p) requires a refinement ratio of r for the calculations.

$$p = \ln\left(\frac{f_3 - f_2}{f_2 - f_1}\right)/\ln(r) \tag{3.3}$$

In this equation, we will assess three grids each time based on the GCI method. Here, f_1, f_2 and f_3 are the MAEs that we have previously calculated for C_p and C_F from Tables 3.3 and 3.4. To clarify, it means that the first calculated GCI is for the first three grids based on their C_p MAE.

For the grid refinement ratio (r) based on the total number of cells, we have selected $r \approx 2$ based on the Δ values and total number cells in Table 3.1 (each time the mesh was refined with an order of 2). Subsequently, we have used the following equation to calculate the GCI for each pair of grid (Roache, 1994).

$$GCI_{21} = \frac{Fs|f_2 - f_1|}{(r^p - 1)} \tag{3.4}$$

In this equation based on the paper by Roache (1994), the safety factor (F_s) is chosen as 1.25 for three or more grids, providing a conservative estimate of discretization error. Now we will use these equations to calculate the GCI of MAE for C_p. The GCI of the first three grids is approximately 2.005%, while the GCI for the second, third and fourth grids reduces to around 0.183%. Similarly, the calculated GCI for MAE of C_F in the first three grids is 0.006%, while for the following three grids (2nd,3rd and 4th grids), it falls to a GCI of 0.003%. Note that we cannot calculate the last three grids (3rd,4th and fifth grids) since the fifth grid was used as a reference point for the calculation of MAE (p will become ∞). From the calculated GCI values, it is apparent that as we refine the grid, the discretization error decreases, indicating an increase in the accuracy of our numerical simulations. However, it is crucial to note that beyond a certain level of refinement (in this case, from the fourth grid onward), the rate of improvement in accuracy tends to slow down, suggesting a degrading return on the computational effort invested in further grid refinement.

In this section, after defining the test case, we used five grids using steady RANS simulations. We reviewed the computational setup and processing times of simulations for each grid. After that, we analyzed different aerodynamic quantities to find the most suitable meshes for our EDDES simulations. More to the point, we found errors in the pressure and skin friction coefficients between the results. Finally, we performed a GCI study on the grids to solidify the choice of the grid for the following section based on all the findings. These steps showed that the fourth grid and fifth grid are refined sufficiently. Therefore, we will use these two grids for further investigations in EDDES simulations.

3.3 EDDES simulations

Previously, we observed that the final two grids outperformed the remaining grids available in the NASA CFDVAL 2004 workshop in the RANS simulations. We will now perform the unsteady simulations and examine how results change with each grid. To do so, the EDDES, defined in section 2.3, are used. We modify these two grids from the RANS simulations (817 x 217) and the fine grid (1633 x 433) in the spanwise direction. Three mesh densities and domain sizes are used to examine the impact of the grids on the WMH and subsequently vortex properties in the next section.

We have modified the original meshes used for the RANS simulations for these simulations. The inlet is now positioned at x/c = -2.14 (previously x/c = -6.39). The reason behind the length reduction is to lower the computational costs. Figure 3.13 shows the new computational domains coloured in black and blue. The velocity and turbulent distributions are interpolated from the RANS solution. The investigation of the effects of this size reduction on the developing boundary layer compared to the results with RANS solution at x/c = -2.14 will be discussed shortly.

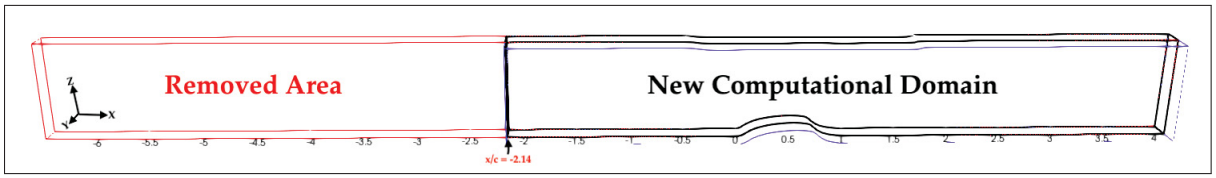

Figure 3.13 Modified computational domain of WMH for EDDES simulations

For the EDDES simulations, with a few minor exceptions, we will employ identical boundary conditions as the ones for the RANS simulations. The WMH boundary conditions for the EDDES simulations are shown in Figure 3.14. The upper wall is an inviscid wall. We imposed periodic boundary conditions in the spanwise direction. The flow enters the WMH channel at the inlet, which is situated at x/c = -2.14 and hits the hump at position zero in the stream direction. The unsteady EDDES simulations largely mirror the configuration of RANS simulations. The

main difference is that each iteration in the EDDES simulations includes sub-iterations that resemble those in the RANS simulations. The unsteady EDDES is carried out over time. This is accomplished using a second order dual-time step approach with the Euler implicit scheme for the inner iterations. Additionally, the time step values for each grid are adjusted based on the computational costs and the CFL value in the region of interest.

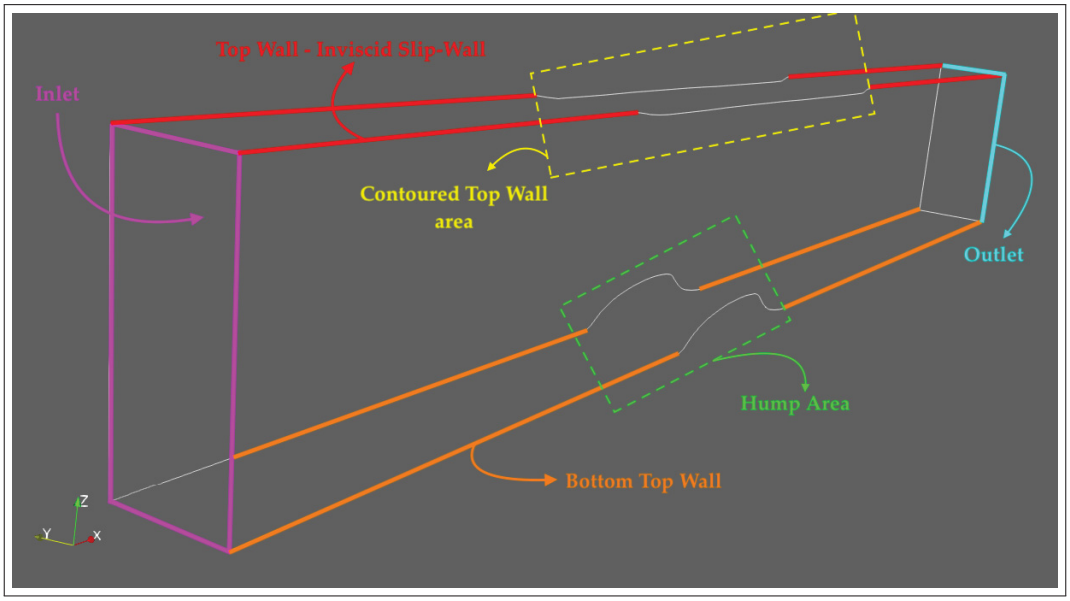

Figure 3.14 Boundary conditions for the EDDES simulations

We interpolated the node coordinates, the unit velocity orientations (i,j,k), the total pressure and temperature, as well as the $\tilde{\nu}$ of the one-equation turbulence model from the previous RANS solution at x/c = -2.14. At the exit, there is a static pressure of 42533.63 Pa. Figure 3.15 shows the imposed total pressure and total temperature at x/c = -2.14.

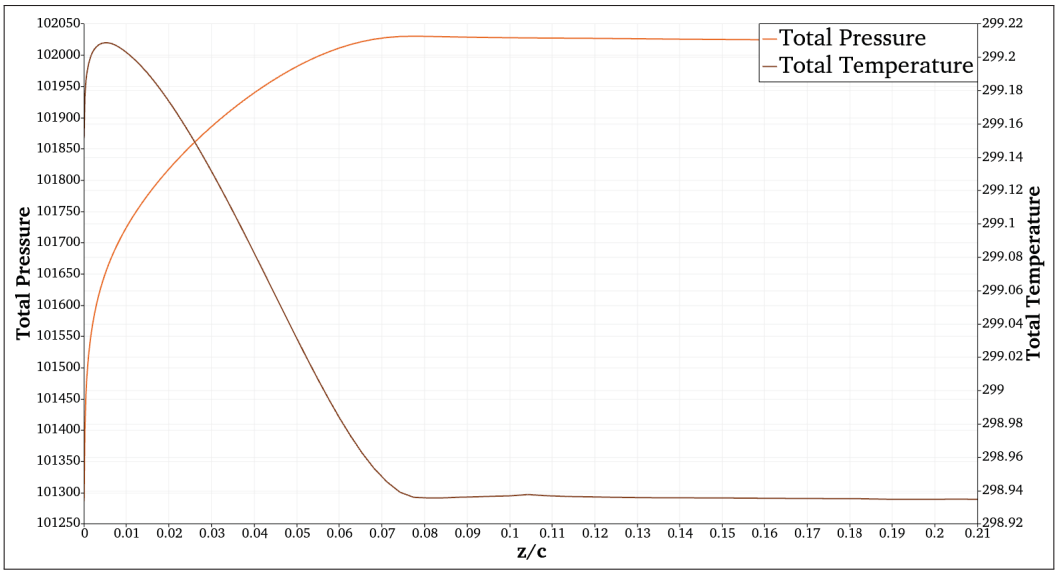

Figure 3.15 Total temperature and total pressure from RANS solution, imposed at inlet (x/c = -2.14)

Figure 3.16, shows the imposed $\tilde{\nu}$ and momentum at x/c = -2.14 of the RANS solution. The velocity vector orientation units are computed from the momentum components. The $\tilde{\nu}$ is for the one equation SA turbulence model.

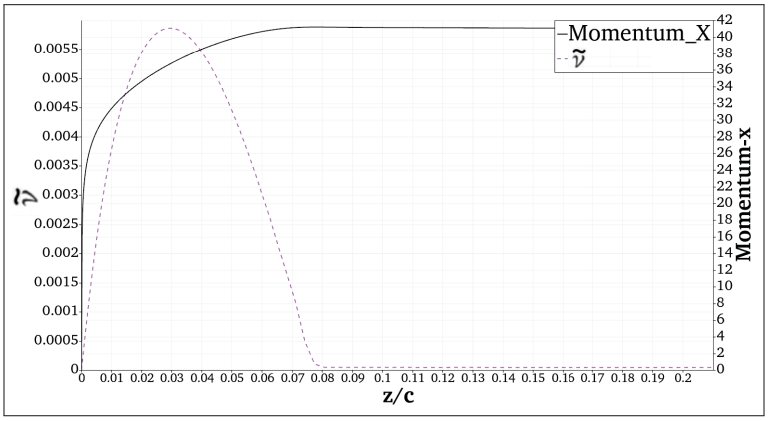

Figure 3.16 The imposed $\tilde{\nu}$ and momentum-x profiles extracted from the RANS solution at x/c = -2.14

We gave these simulations names. EDDES-M1, EDDES-M2, and EDDES-M3. The grids of these simulations are shown in Figure 3.17. The numerical settings of these simulations were explained in 2.3.

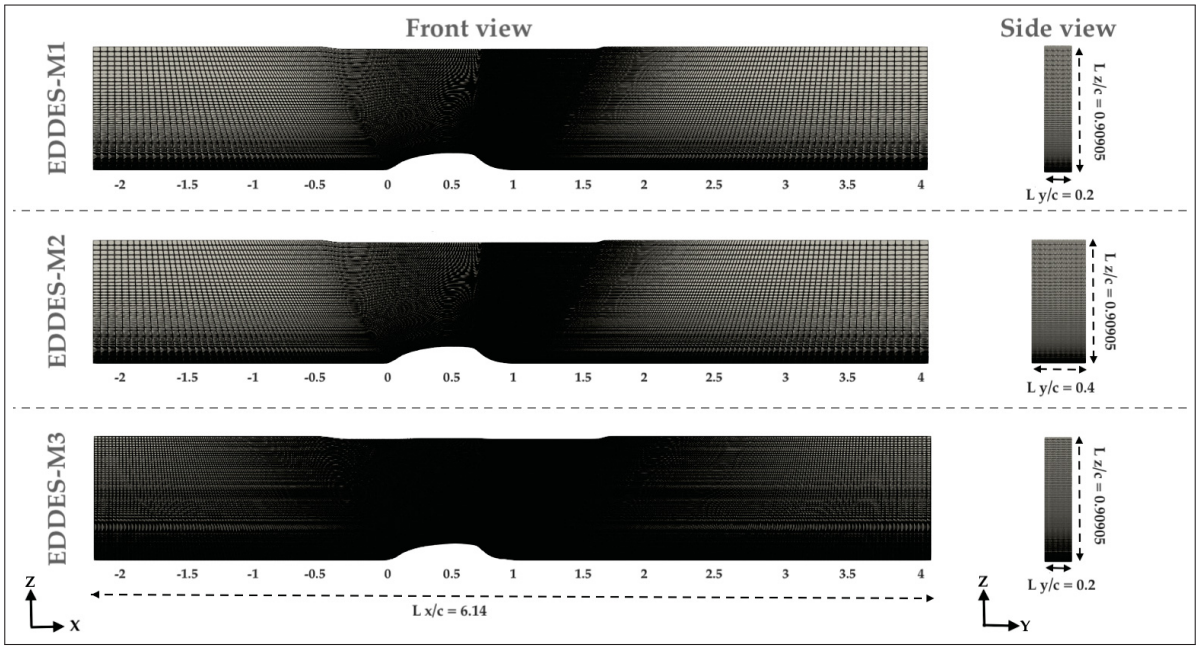

Figure 3.17 Grids used for the EDDES simulations

Table 3.6 displays the parameters of these grids. In essence, the second mesh is the first grid with double the spanwise size (x/c = 0.4 instead of x/c = 0.2). This is being done to examine the impact of the spanwise size and see whether we can lessen the impact of the gray area issue. It is important to note that the minimum distances depicted in the table (Δ_x, Δ_y and Δ_z) are measured near the wall, from where the flow separation begins (similar to Figure 3.3 for the RANS). Since the mesh is not constant, these numbers do not match across all of the computational domains. However, in the spanwise direction, the distances between each node (Δ_y) are the same.

Table 3.6 Characteristics of NASA grids for the WMH

Name	n_X	n_Y	n_Z	Δ_x	Δ_y	Δ_z	**Total cells**
EDDES-M1	768	216	32	1.14×10^{-3}	6.25×10^{-3}	7.41×10^{-6}	5,308,416
EDDES-M2	768	216	64	1.14×10^{-3}	6.25×10^{-3}	7.41×10^{-6}	10,616,832
EDDES-M3	1536	432	32	5.7×10^{-4}	6.25×10^{-3}	3.86×10^{-6}	21,233,664

The time step Δt varies between each simulation. Table 3.7 shows the time step for each of our EDDES simulations. The selected time steps are based on having a CFL of around one, near the wall in the separation region.

Table 3.7 Time step (Δt) for each simulations

Name	Δt
EDDES-M1	1.5×10^{-5} (s)
EDDES-M2	2×10^{-5} (s)
EDDES-M3	4×10^{-5} (s)

The EDDES-M1 simulations density residuals are displayed in Figure 3.18. The total number of iterations can be seen at the bottom of the graph, and the dimensionless simulation duration can be observed at the top ($\frac{\Delta t \times u}{c}$). We can see that each iteration involves completing several sub-iterations to obtain the log ρ of -8. Each of these colors represents an average flow over that period that was computed internally by SU2. In other words, each of these colors represent a simulation (of one day) and averaged in time by SU2 for that period. In the RANS simulations, we observed a direct correlation between a CFD solver convergence and the decline in the density residuals. However, the graphs for EDDES simulations won't be the same. It is because before moving on to the next iteration, some sub-iterations are completed in each iteration. The sub-iteration for these simulations is limited to a maximum of 20 or when the residuals reach -8 for the log ρ. Figure 3.18 shows the last value which is obtained at the end of the sub-iteration.

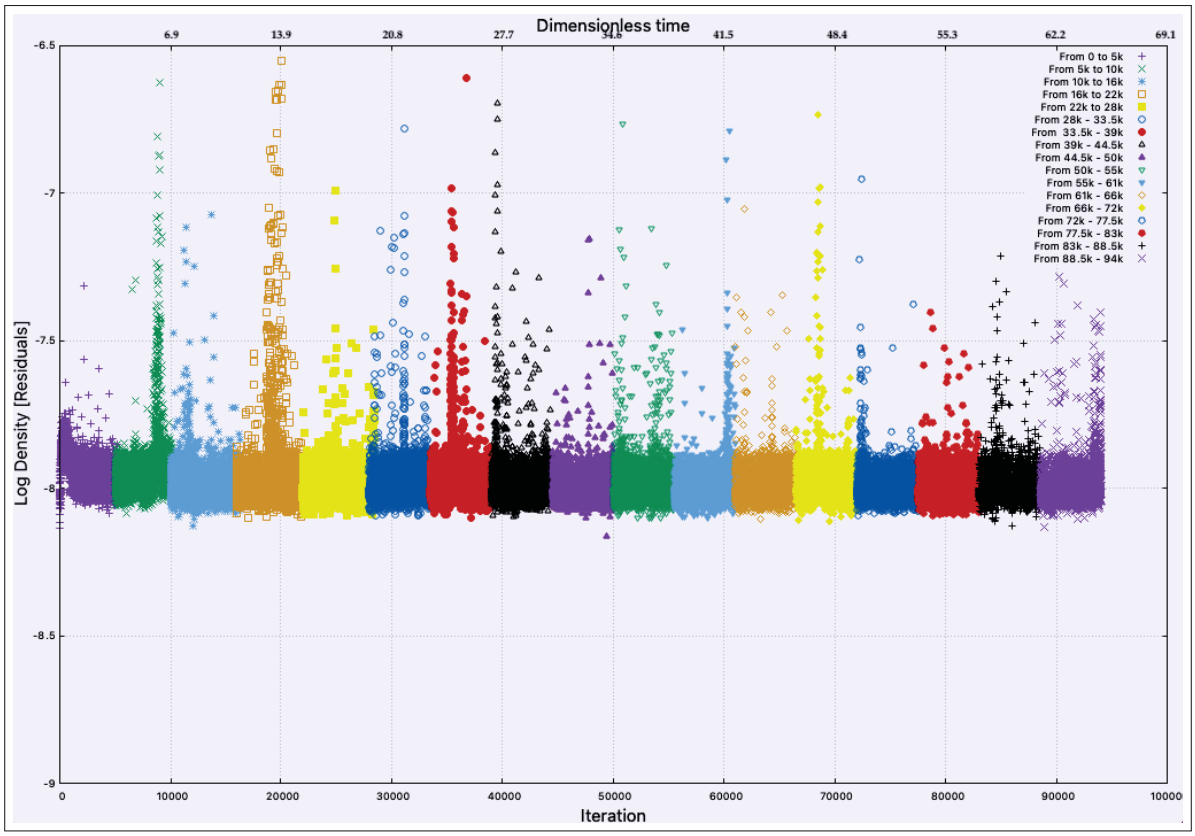

Figure 3.18 Log of the residuals ρ equation as a function of iteration and dimensionless time $\frac{\Delta t(s) \times u(m/s)}{c(m)}$ for the EDDES-M1 simulation

Figure 3.19 represents the lift coefficient calculated by SU2 for each iteration. The top axis shows the evolution of the lift coefficient as a function of dimensionless time. When the flow has laminar features, a sinusoidal pattern connected to the development of vortex formations in a separated flow may be seen. But because the flow is three-dimensional, vortex shedding does not happen all at once across the span. Therefore, in such complex situations, a perfect sinusoidal form is not usually expected.

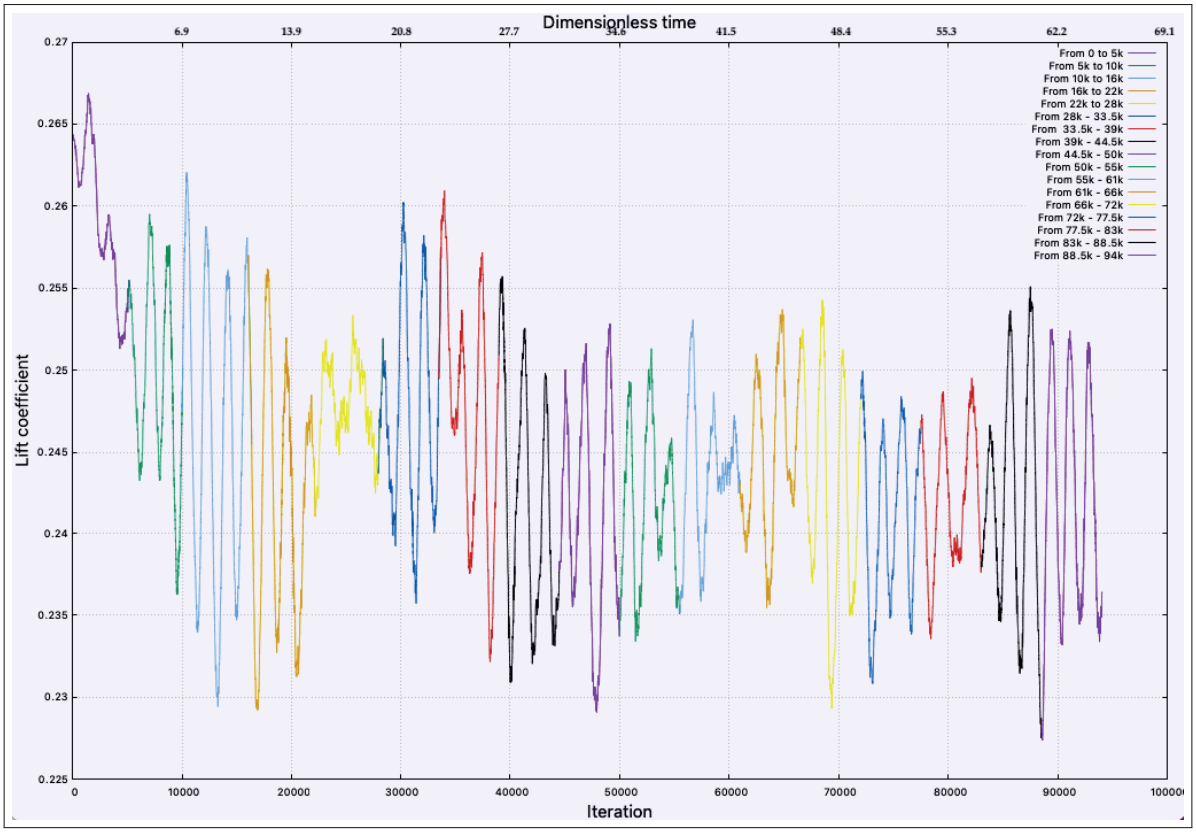

Figure 3.19 Lift coefficient C_L calculated by SU2 for each iteration for the EDDES-M1 simulation

The drag coefficient is also calculated iteratively by SU2. We can see the variation of drag coefficient in each iteration and also with respect to dimensionless time in Figure 3.20. The first four averaging periods show different drag coefficient values compared to other periods. Therefore it is another way of knowing which iterations are discarded to eliminate the transient effects of unsteady simulations. Only one of the simulations convergence curves is shown (EDDES-M1). We will utilize the same analysis criteria for the other two simulations to get averages in time and space.

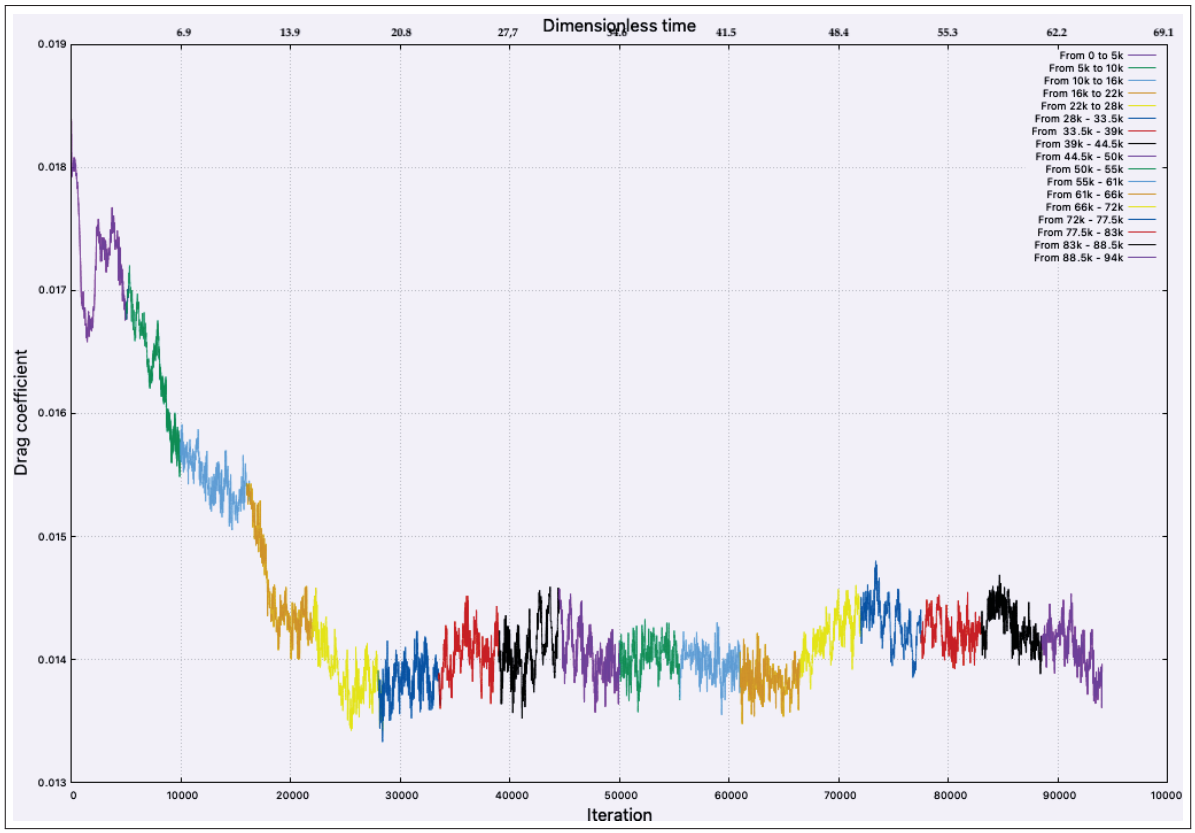

Figure 3.20 Drag coefficient C_D calculated by SU2 for each iteration for the EDDES-M1 simulation

Figure 3.21 shows the 2D velocity fields over the WMH using Line Integral Convolution (LIC) by Cabral & Leedom (1993). The LIC lines, which represent the direction and magnitude of velocity vectors, trace the instantaneous paths of particles. They illustrate the complex routes of flow particles as they cross the WMH channel. In Figure 3.21, random snapshots of LIC lines over the WMH signify the difference between the steady and unsteady simulations.

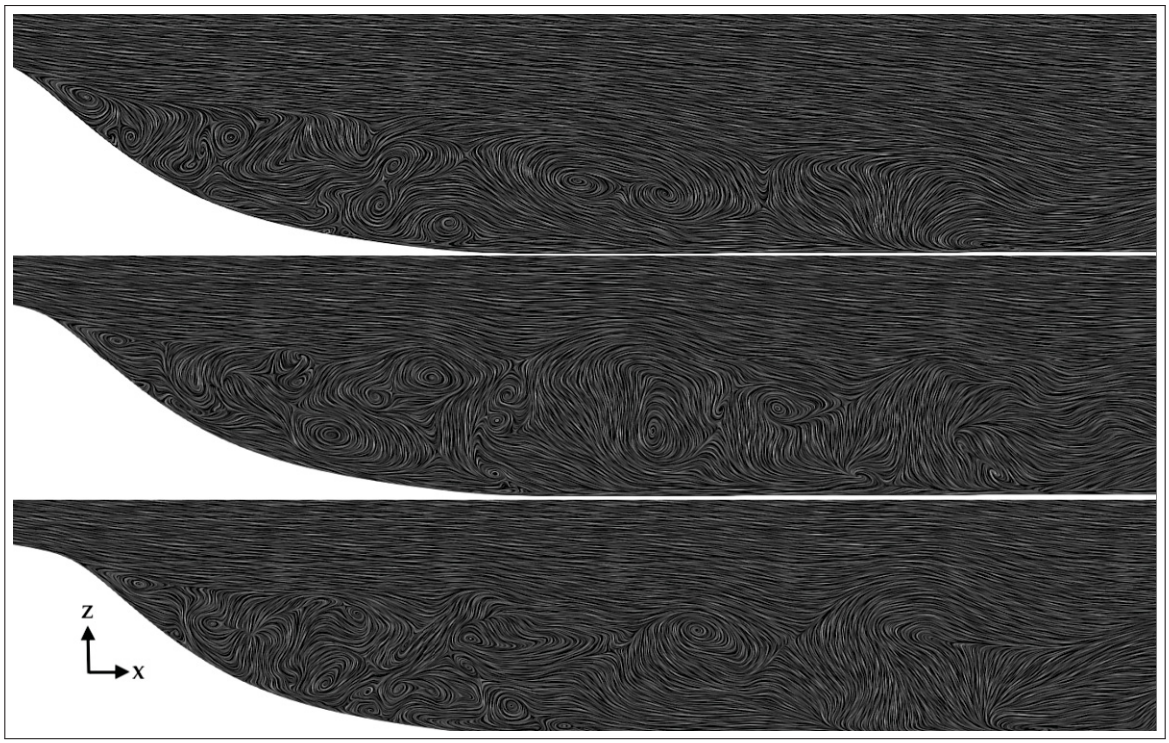

Figure 3.21 Snapshots of LIC lines in random time steps from EDDES-M1, illustrating instantaneous velocity over the mid-section plane of the WMH around the region of interest

Unlike RANS simulations, the unsteady simulations involve dynamic fluctuations where observing instantaneous variables can often prove misleading for gaining insights into the flow characteristics. This difference primarily comes from the fundamental difference in these methodologies. While the RANS focus on time-averaged flow properties and provides a statistically stable picture of the flow, unsteady simulations depict transient flow phenomena where the instantaneous snapshots of the variables do not represent the overall flow physics. It is crucial to realize that in unsteady simulations, the transient features manifest themselves through changes in the flow variables over time. Thus, understanding the underlying flow mechanisms requires averaging in space and time (Blazek, J., 2015).

The averaging intervals for these simulations are detailed in Table 3.8. Following the approach utilized in the literature, such as the studies by Guseva *et al.* (2017), Patel & Zha (2020), and

Siggeirsson & Andersson (2019), the transient periods at the beginning of their simulations are neglected for the time averaging (around one third of the full simulations). Upon examining the drag coefficient curve again (Figure 3.20), we observed that for the EDDES-M1 simulation, there is a noticeable reduction in fluctuation after the 28000th iteration, compared to the more significant variations observed during the initial stages. Therefore, we have neglected the first five averaging periods (from iteration 0 to 28000 for EDDES-M1) calculated by SU2 for our time averaging. We used the same examination for other two simulations. As the mesh gets denser, the computational cost is more expensive, subsequently, the averaging periods (colors in Figure 3.18) become shorter for a one day simulation. Therefore, the reason behind different periods in Table 3.8 is due to heavier computational costs and more averaging periods.

Table 3.8 Averaging periods for EDDES simulations

Name	**Iterations period**	**Non-dimensional time**
EDDES-M1	(28k - 94k)	(19.6 - 64.2)
EDDES-M2	(20k - 65k)	(13.9 - 44.6)
EDDES-M3	(18k - 28k)	(24.7 - 38.4)

Now that we have chosen the periods for the time averaging of our EDDES simulations, we should do the averaging in space. To do so, we plot the pressure coefficient along the wall at several locations in the spanwise direction. Figure 3.22 shows these lines on the wall of the WMH.

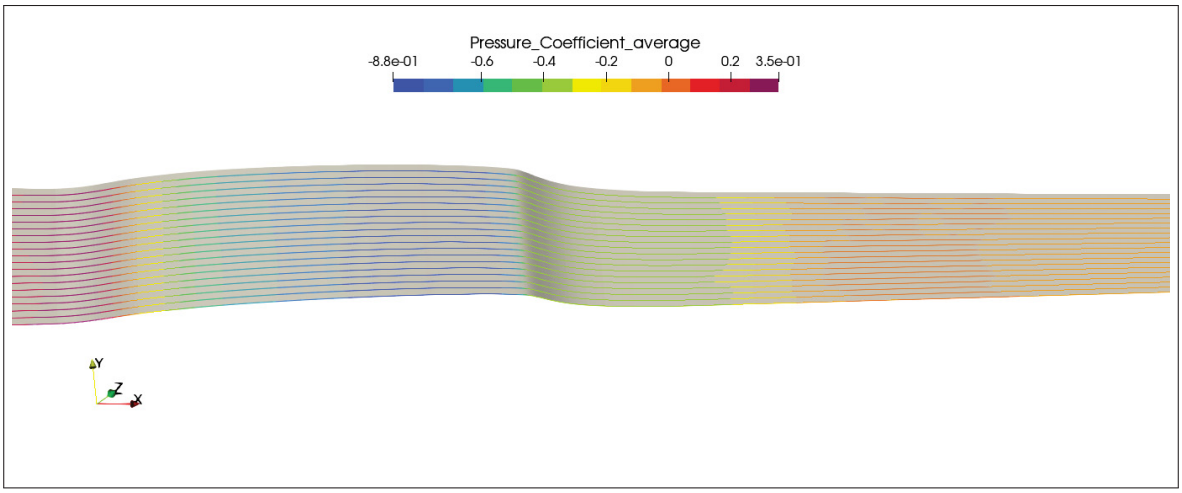

Figure 3.22 The time averaged pressure coefficient of the EDDES-M1 simulation, plotted over lines on the wall of the WMH

The spacing in selecting these lines is $L_{z/c} = 0.1$. It means that EDDES-M1 and EDDES-M3 have 20 lines from $z/c = -0.01$ to $z/c = -0.2$, since their spanwise length equals to $\Delta_{z/c} = 0.2$. For the EDDES-M2 with twice the spanwise length, 40 lines have been plotted along the wall (from $z/c = -0.01$ to $z/c = -0.4$). Figure 3.23 shows the different time-averaged pressure coefficients along the wall of the WMH as a function of x/c (previously shown in figure 3.22). This means that we get a full time average based on the selected periods (Table 3.8) and we have plotted lines in different locations of span along stream-wise direction to get an average in space.

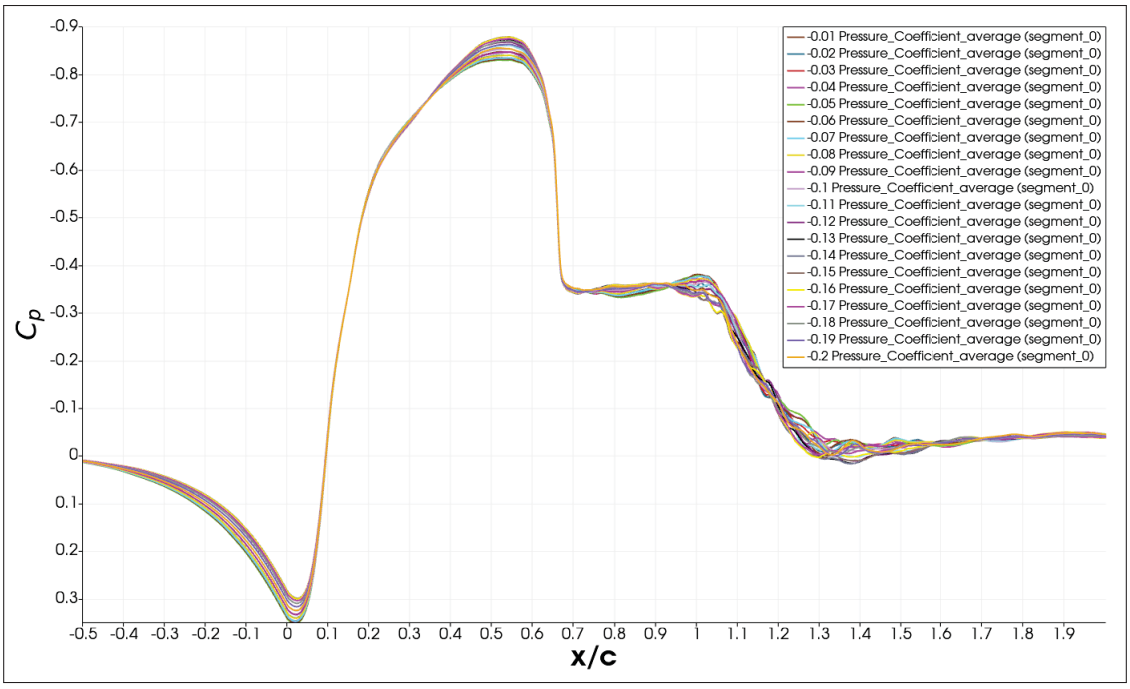

Figure 3.23 The time-averaged pressure coefficients of the EDDES-M1 in different spanwise locations along the wall of the WMH

We export these lines into Python to perform an average between all of the lines. We do this for EDDES-M2 and EDDES-M3 also. Figure 3.24 shows the time and space-averaged pressure coefficients between our EDDES simulations and the experimental result from Greenblatt *et al.* (2006). The critical locations of the WMH are also specified, as we have done for the RANS simulations.

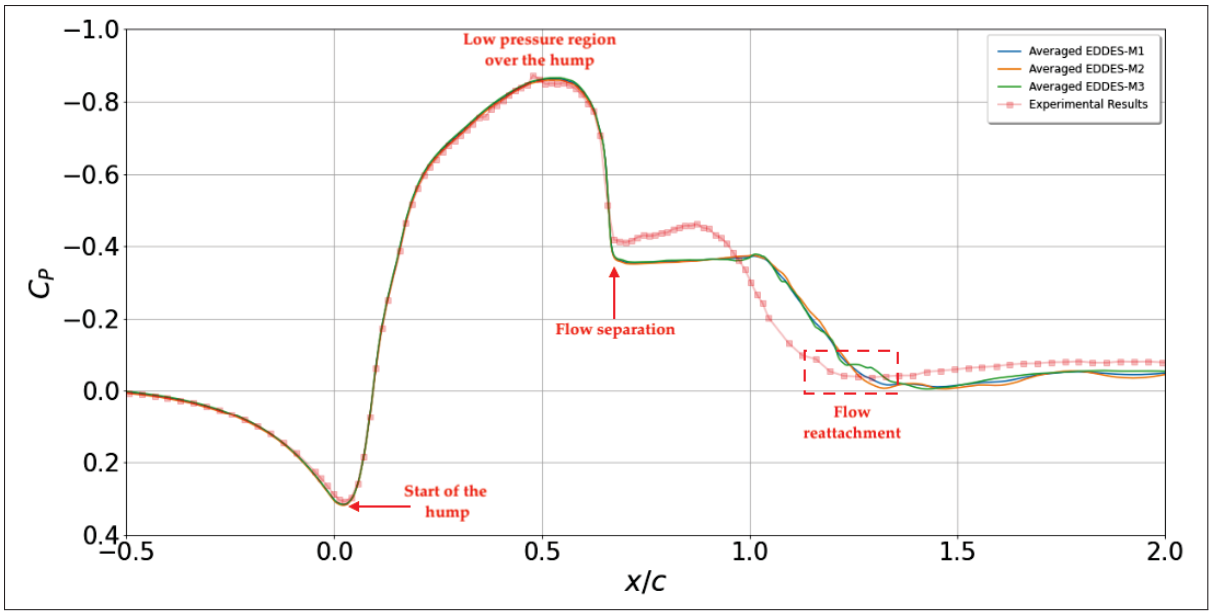

Figure 3.24 Time and space averaged pressure coefficients along the wall of the WMH for the EDDES simulations, compared with the experimental results of Greenblatt *et al.* (2006)

Figure 3.25 compares the EDDES-M2 pressure coefficient on the wall of the WMH with the results from Guseva *et al.* (2017); Siggeirsson & Andersson (2019) and experimental results (Greenblatt *et al.*, 2006). We can visually see that the EDDES-M2 behaves similarly to the Siggeirsson & Andersson results. However, Guseva *et al.* results have a better agreement with the experimental results. The comparison of the EDDES-M2 pressure coefficient with the literature and experimental results shows both areas of strong agreement and potential room for refinement. In particular, the good performance in the low-pressure region is encouraging, while the discrepancy in the reattachment region, points to areas where further investigation and model refinement may be needed.

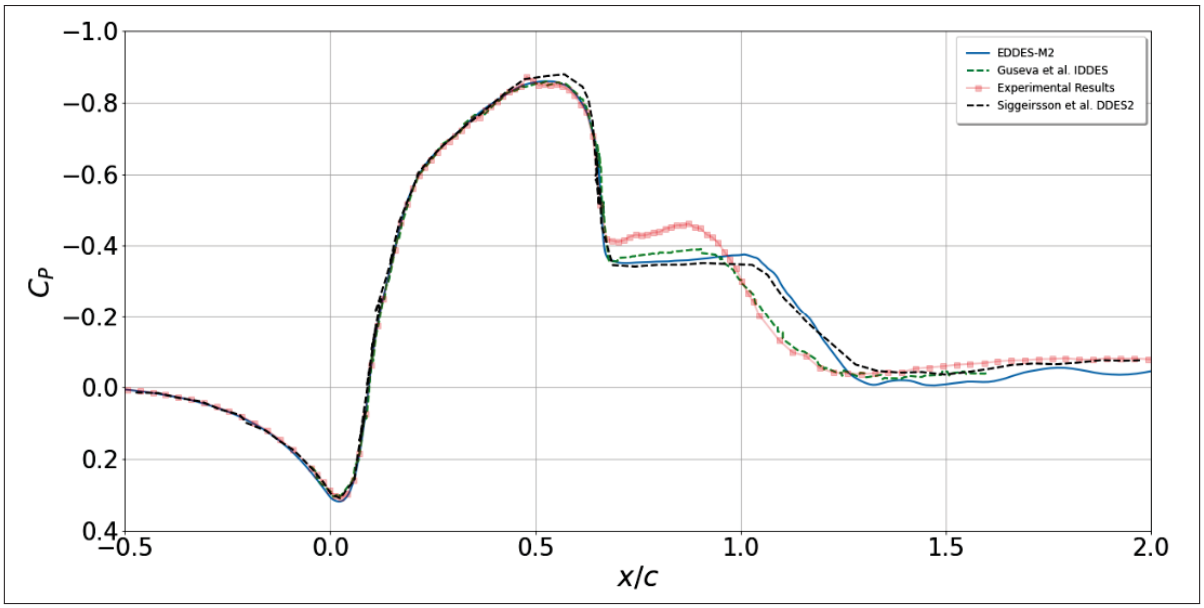

Figure 3.25 Time and space-averaged pressure coefficient of the EDDES-M2 simulations compared to the results of Guseva *et al.* (2017); Siggeirsson & Andersson (2019) and experimental results of Greenblatt *et al.* (2006)

We have averaged the pressure coefficient in time and space and the same approach is used for the skin friction coefficient. We use the time-averaged skin friction coefficients along the wall of the WMH (see Figure 3.22). Similarly, the EDDES-M1 and EDDES-M3 have twenty lines along the wall in the spanwise direction, while EDDES-M2 have forty lines. Figure 3.26 shows the time-averaged skin friction coefficients plotted along the wall in different spanwise locations for the EDDES-M1 solution. We can see the variations in the time averaged solutions begin after the flow gets separated from the wall, which suggests the complexity of flow dynamics in the separation region.

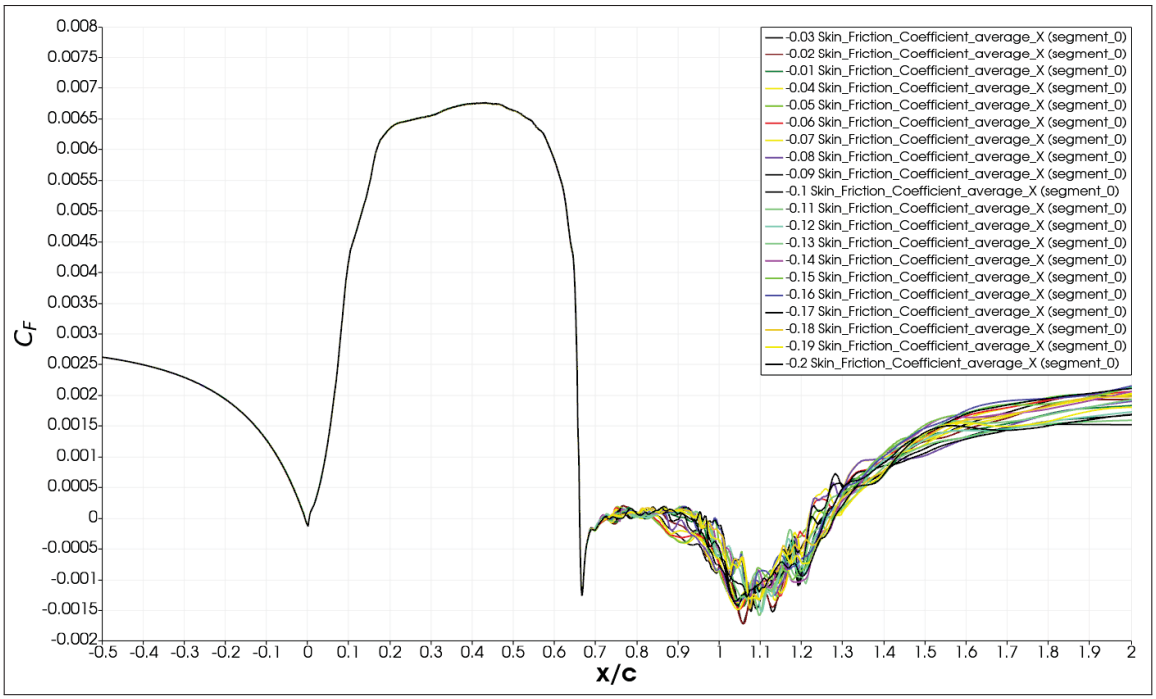

Figure 3.26 The time-averaged skin friction coefficients of the EDDES-M1 in different spanwise locations along the wall of the WMH

Figure 3.27 shows the time and space-averaged skin friction coefficients of our EDDES results compared with the experimental results from Greenblatt *et al.* (2006). The critical stages of the flow in the WMH are also identified. We can see that the curve for EDDES-M2 seems smoother than the other two simulations. This could be due to the fact that it had twice the spanwise length, and averaging in space is performed over forty lines (unlike twenty lines for EDDES-M1 and M2). The other potential cause is the limited number of time averaging periods because of the high computational costs. Moreover, we see an overall agreement between these simulations before the flow separation.

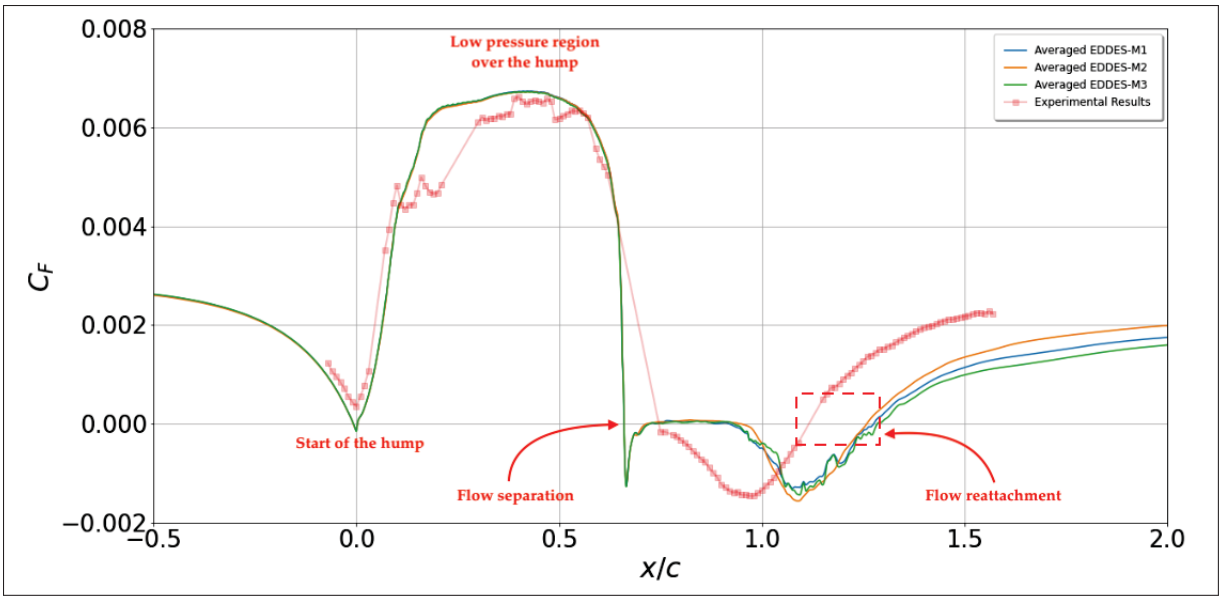

Figure 3.27 Time and space averaged pressure coefficients along the wall of the WMH for the EDDES simulations, compared with the experimental results of Greenblatt *et al.* (2006)

Figure 3.28 compares the skin friction coefficient obtained from the results of Siggeirsson & Andersson, Guseva *et al.* (see Figures 1.3b and 1.5), and experimental results of Greenblatt *et al.* to our EDDES-M2 results that have been time and spatially averaged. In this figure, the reattachment locations are also specified. Each arrow colour represents the reattachment location of the corresponding simulation. The error in the flow reattachment (difference from the experimental reattachment) is visible here. We can see that the difference between EDDES-M2 and the experimental reattachment is slightly less compared with the results from Siggeirsson & Andersson (2019). However, the results from Guseva *et al.* (2017) has the highest agreement with the experiment.

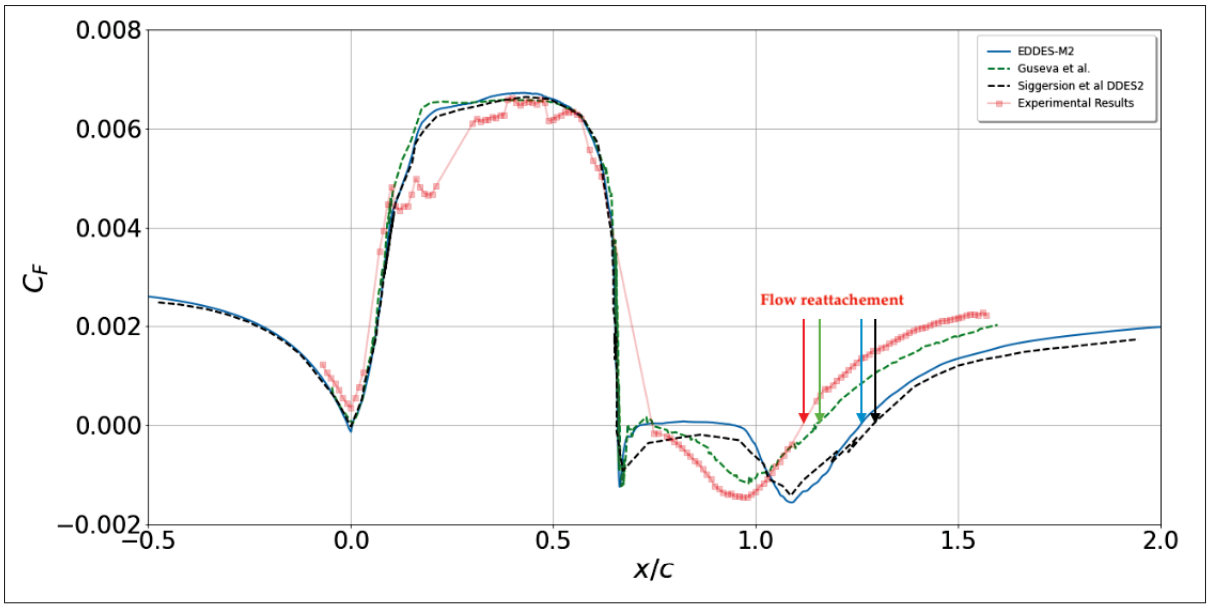

Figure 3.28 Time and space-averaged skin friction coefficient of the EDDES-M2 simulations compared to the results of Guseva *et al.* (2017), Siggeirsson & Andersson (2019) and experimental results of Greenblatt *et al.* (2006)

As a final step, we will use the skin friction coefficient plots to pinpoint the separation and reattachment locations. Usually, when the skin friction goes into negative signs, it indicates that the flow is getting separated from the wall. On the other hand, when it goes into positive values again, it shows the reattachment location (see for example Armstrong *et al.* (2022)). Table 3.9 presents the locations of flow separation and reattachment obtained from our simulations, along with corresponding numerical results from Siggeirsson & Andersson (2019), Guseva *et al.* (2017) and experimental findings from study Greenblatt *et al.* (2006).

Table 3.9 Non dimensional separation and reattachment locations (x/c) of the WMH compared to the experimental data of Greenblatt *et al.* and numerical results of Siggeirsson & Andersson and Guseva *et al.* (2017) using the C_F values

Simulation	**Sep. loc (x/c)**	**Re-attach. loc (x/c)**	**Bubble len. (x/c)**
Experimental	0.665 ± 0.005	1.10 ± 0.005	0.435
EDDES-M1	0.659	1.275	0.616
EDDES-M2	0.659	1.257	0.598
EDDES-M3	0.659	1.281	0.622
Siggeirsson & Andersson	0.659	1.266	0.607
Guseva *et al.*	0.663	1.151	0.488

To see the differences in these locations, we calculate the errors in reattachment and separation locations compared to the experimental results from Table 3.9. The formula is to differentiate the numerically predicted values from experimental values divided by the experimental values multiplied by 100%. Table 3.10 shows these errors compared to the experimental results. It is important to note that in our comparisons, we have used the exact values of x/c = 0.665 and x/c = 1.10 from the experimental data. However, the experimental results indicate a margin of error of x/c = 0.005 for separation and reattachment locations.

Table 3.10 Percentage errors in predicted separation and reattachment locations (x/c) of the WMH for various simulation models compared to experimental data

Simulation	**Error in Sep. loc (%)**	**Error in Re-attach. loc (%)**
EDDES-M1	0.90	15.91
EDDES-M2	0.90	14.27
EDDES-M3	0.90	16.45
Siggeirsson & Andersson	0.90	15.09
Guseva *et al.*	0.30	4.64

This table shows how EDDES and Siggeirsson & Andersson results over-predict the reattachment location, while the results from Guseva *et al.* are much closer to the experimental results. We explored finer meshes than the one Guseva *et al.* used, with different spanwise sizes as suggested by Siggeirsson & Andersson. Nevertheless, a wider separation can still be seen in our EDDES simulations. Therefore, a higher-order scheme (not currently available in SU2) is the suspect to solve the gray area issue. Higher-order schemes have the potential to capture flow features and gradients more accurately, thereby reducing numerical dissipation and enhancing the resolution of turbulence structures. Moreover, we can also conclude that between the EDDES results, EDDES-M2 having twice the span size (and twice the average samples in the spanwise direction) predicts a lower error in separation location and a smoother curve compared to EDDES-M1 and EDDES-M3 (see Figure 3.27, for example).

In this section, we have taken several steps toward understanding the differences between unsteady simulations compared with RANS simulations by establishing a robust computational setup. We have analyzed the internally averaged solution provided by SU2, enabling accurate time averaging of our EDDES solutions. Additionally, we have chosen multiple locations in the spanwise direction to extract aerodynamic coefficients, facilitating reliable spatial averaging. Then, to shed light on the gray area issue within hybrid approaches, we have compared our results and relevant literature and experimental data. This comparative analysis aims to identify potential challenges and discrepancies associated with the gray area phenomenon. Finally, moving toward our main objective, the subject of the next section lies on performing a quantitative analysis of the number of captured vortices using the mentioned methodologies, including the Q-criterion, λ_2, and λ_{ci}^2. By employing these techniques, we aim to differentiate this technique for identifying coherent structures present in the flow in the WMH channel after it gets separated from the wall.

3.4 Vortex identification

For steady and unsteady simulations of the WMH, we have assessed the velocity, pressure coefficient and skin friction coefficient. We have observed in the EDDES simulations that vortices form after the flow separation and affect the behaviour of the flow. Quantifying these

vortices is the main objective here. We do a quantitative analysis of the number of vortices in three main locations after the hump. Three different identification techniques are used to identify and analyze the vortices characteristics. The process of our identification methods for quantifying vortices is shown in the flow chart below. Our EDDES simulations (EDDES-M1, EDDES-M2, and EDDES-M3) provide the input data.

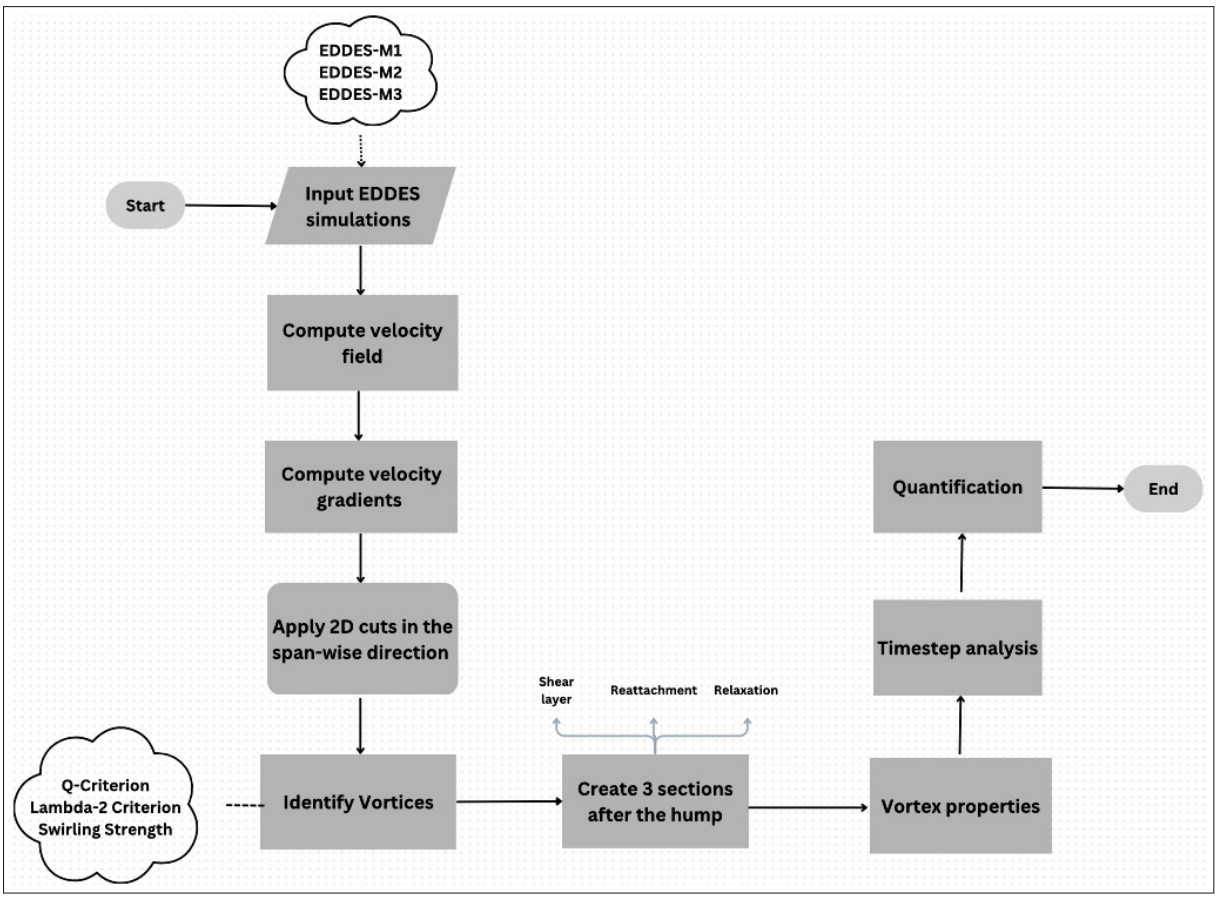

Figure 3.29 Flow chart of the first part of the quantitative study

Figure 3.30 illustrates schematically the flow behaviour after it gets separated from the wall and the vortex structures develop. There are three main sections in the WMH channel, as depicted in the figure, and previously covered in the literature review especially by the paper of Hao *et al.* (2021). Despite the common association of high vorticity with separated flows, it is important to note that a high level of vorticity also occurs in attached boundary layers, especially near the

wall. Therefore, even in the recovery region after reattachment, vorticity does not necessarily reduce due to the proximity to the boundary layer.

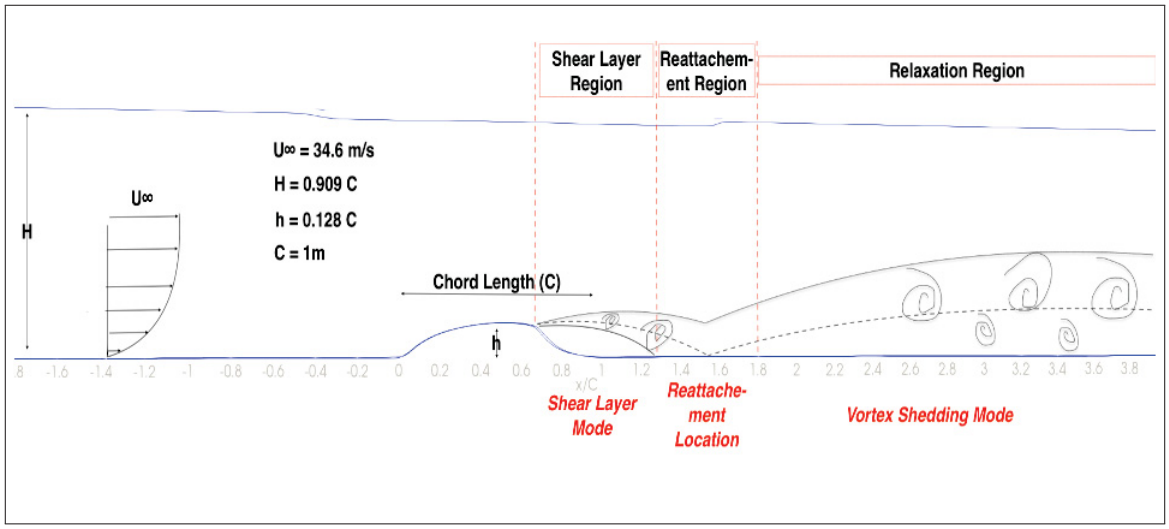

Figure 3.30 Scheme of the flow separation in the WMH channel

To count the number of vortices in the WMH channel, we have divided the part after the hump into its critical locations according to Hao *et al.* (2021). These locations are from (x/c= 0.65 to 1.25),(x/c= 1.25 to 2) and (x/c= 2 to 4). Figure 3.31 shows these locations on the WMH channel. The idea behind choosing these sections is based on the critical locations of literature findings and our EDDES simulations (We have selected an approximate-round value from Table 3.9 for separation and reattachment regions). The first section is from the separation point to the re-attachment point. The second section is from the re-attachment point to the approximate relaxation region, and the final section is from the chosen relaxation region until the end of WMH channel. Additionally, the domain is sliced in the stream-wise direction to obtain a 2D component of the solution. The mid-span plane for all of our simulations is represented by the pink plane, located at y/c= -0.1.

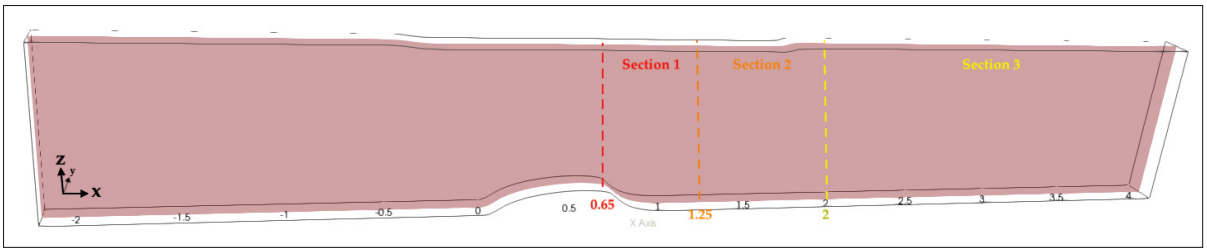

Figure 3.31 Channel division after separation point for vortex quantification

We intend to conduct a quantitative analysis of the number of identified vortices for our EDDES simulations, as was previously indicated. We will employ the Q-criterion, λ_2 criterion, and Swirling Strength (λ_{ci}^2 criterion) defined in section 2.4 as our three identification methodologies. Since the simulations are unsteady and vary in time, we will attempt to choose the snapshots for each simulation that are comparable to the other two EDDES simulations for the comparisons and post-processing.

Table 3.11 Table representing the periods for further analysis of the vortices

Section	**Location (x/c)**	$\Delta_{x/c}$ **(x/c)**	**Representing Region**
1	(0.65 to 1.25)	0.6	Shear layer region
2	(1.25 to 2)	0.75	Reattachment region
3	(2 to 4)	2	Relaxation region

The 2D and 3D Q-criterion contours are shown in Figure 3.32. We choose Q=25000 (s^{-2}) as the threshold after visualizing the flow with other well-known values used for this test case and the studies from Schanz *et al.* (2016) and Merabet (2021) that compare different threshold values. In the dimensionless form (with $Q = Q^* \times \frac{c^2}{U^2}$), $Q^* \approx 784.65$. The 3D form of Q, which resembles tubes after being separated from the hump, is depicted on the top in Figure 3.32. We will look for the 2D vortex formations to conduct a quantitative investigation. As a result, only Q contours on the pink plane (2D, $y/c = -0.1$) will be analyzed.

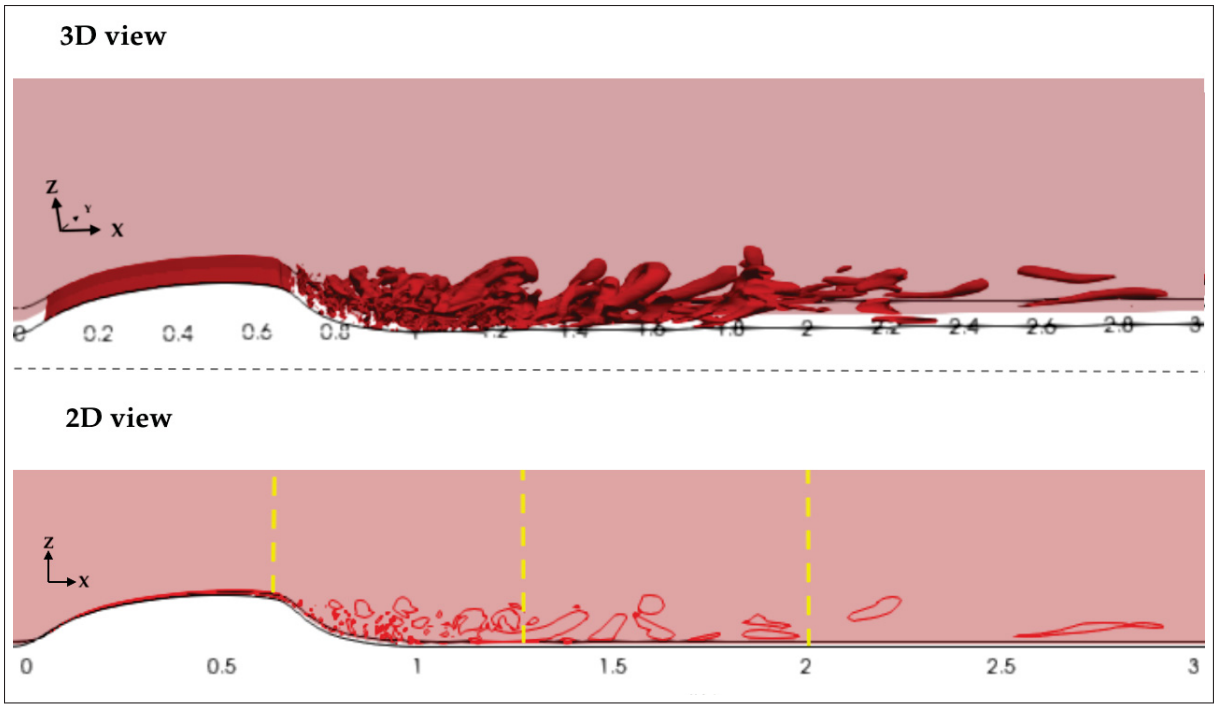

Figure 3.32 Q-criterion representation in 2D and 3D for EDDES-M1 simulations

The visualization of vortex forms in a flow field in 2D and 3D using the λ_2 criterion, is shown in Figure 3.33. The second eigenvalue (λ_2) of the symmetric tensor sum of the squares of the vorticity tensor (Ω) and the strain rate tensor (S) is the basis of the λ_2 criteria. Areas with negative λ_2 values are isolated to form vortex regions. The Q-criterion compares the magnitudes of the vorticity and strain tensors, while the λ_2 criterion uses eigenvalues to analyze the balance between vorticity and strain in the flow. Because of the mathematical equation of λ_2 the threshold value is similar to the opposite value of the Q-criterion. So, we have established $\lambda_2 = -25000(s^{-2})$ or $\lambda_2^* = -784.65$ as the threshold value for better comparisons.

Table 3.12 The properties of our vortex identification methods

Method	Threshold Value	Units	Color	Dimensionless values
Q-criterion	25000	s^{-2}	Red	784.65
λ_2 criterion	-25000	s^{-2}	Yellow	-784.65
λ_{ci}^2	1000	s^{-1}	Blue	31.43

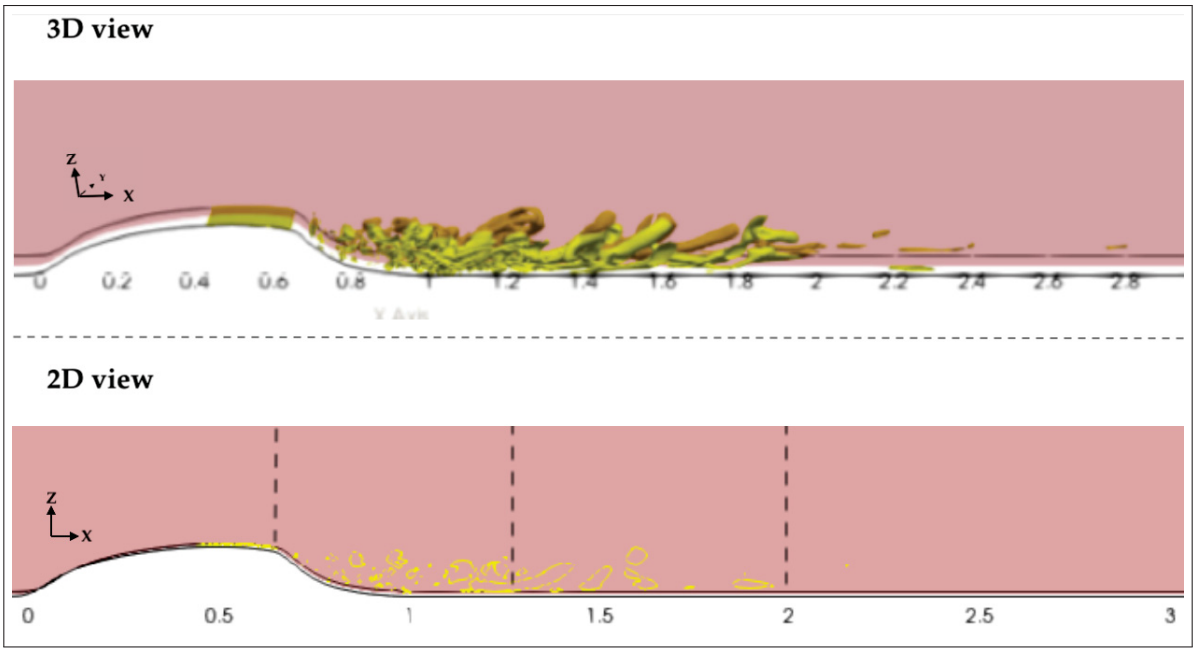

Figure 3.33 λ_2 Criterion representation in 2D and 3D for EDDES-M1 simulations

Figure 3.34 represents the λ_{ci}^2 in the WMH channel. Due to the differences in the underlying principles of each vortex identification technique, the λ_{ci}^2 values can have different magnitudes and distributions compared to λ_2 and Q-criterion values. Therefore, to effectively visualize vortex structures, the threshold value used for the λ_{ci}^2 method needs to be adjusted. The threshold value used to visualize a physical vortex representation is 1000 (s^{-1}) ($\lambda_{ci}^{2*} = 31.43$). For λ_{ci}^{2*}, there are no particular evidence of choosing this specific value from the literature and the suggested value by Zhou *et al.* that is exactly comparable to the other two methodologies, however, after trial and error, we have found out that lower values cannot distinguish the vortices clearly and increasing the value results in capturing large regions that are not connected to vortex properties.

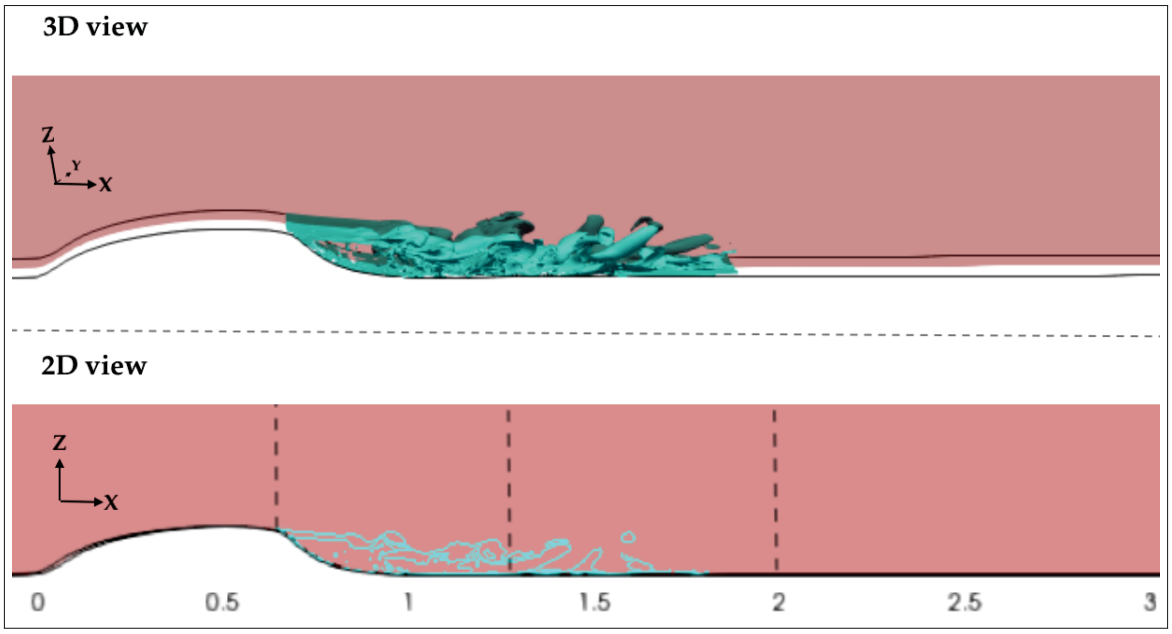

Figure 3.34 λ_{ci}^2 representation in 2D and 3D for EDDES-M1 simulations

A quantitative study on each simulation is performed over ten snapshots of our unsteady simulations. These gives us the number of vortices in time and space for each simulation. Which are then represented using histograms and tables.

We begin with the shear layer of the EDDES-M1 simulation. Figure 3.35 represents the identified vortices captured by our different vortex identification methodologies. The red lines represent the vortices detected using the Q-criterion, the yellow lines represent the λ_2 criterion, and the blue lines the λ_{ci}^2 technique. We will quantify the time of the simulation relatively in regards to the starting time, which we have excluded due the to the fact that the flow was transient. Thus, "t" stands for the difference between the second iteration number to the first one, multiplied by the time step for the simulation plus the starting time.

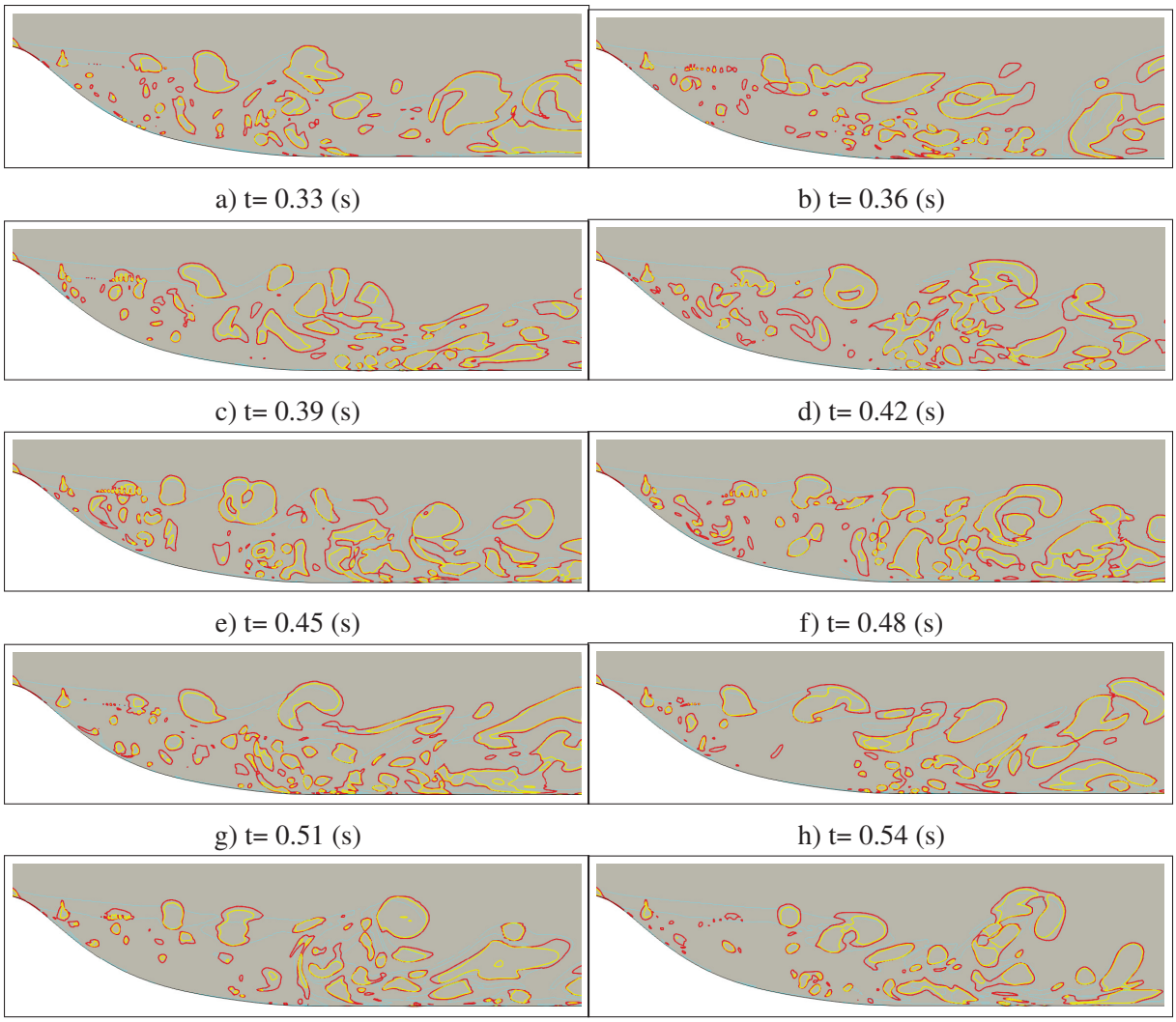

Figure 3.35 The first division of the WMH channel for the EDDES-M1 simulations, after the hump where the flow gets separated from the wall. This shear layer region is from x/c= 0.65 to 1.25 (red : Q ; yellow : $\lambda 2$; blue : λ_{ci}^2)

Figure 3.36 depicts the second region for the EDDES-M1 simulations following the hump from x/c = 1.25 to 2. We can observe a decrease in the overall number of vortices identified using our vortex identification techniques. The underlying reason is that the flow begins to slow down and reattach to the wall. If we compare it to the shear-layer region, the flow becomes less unstable. As a result, the vortices that develop here often have a smaller number and bigger size.

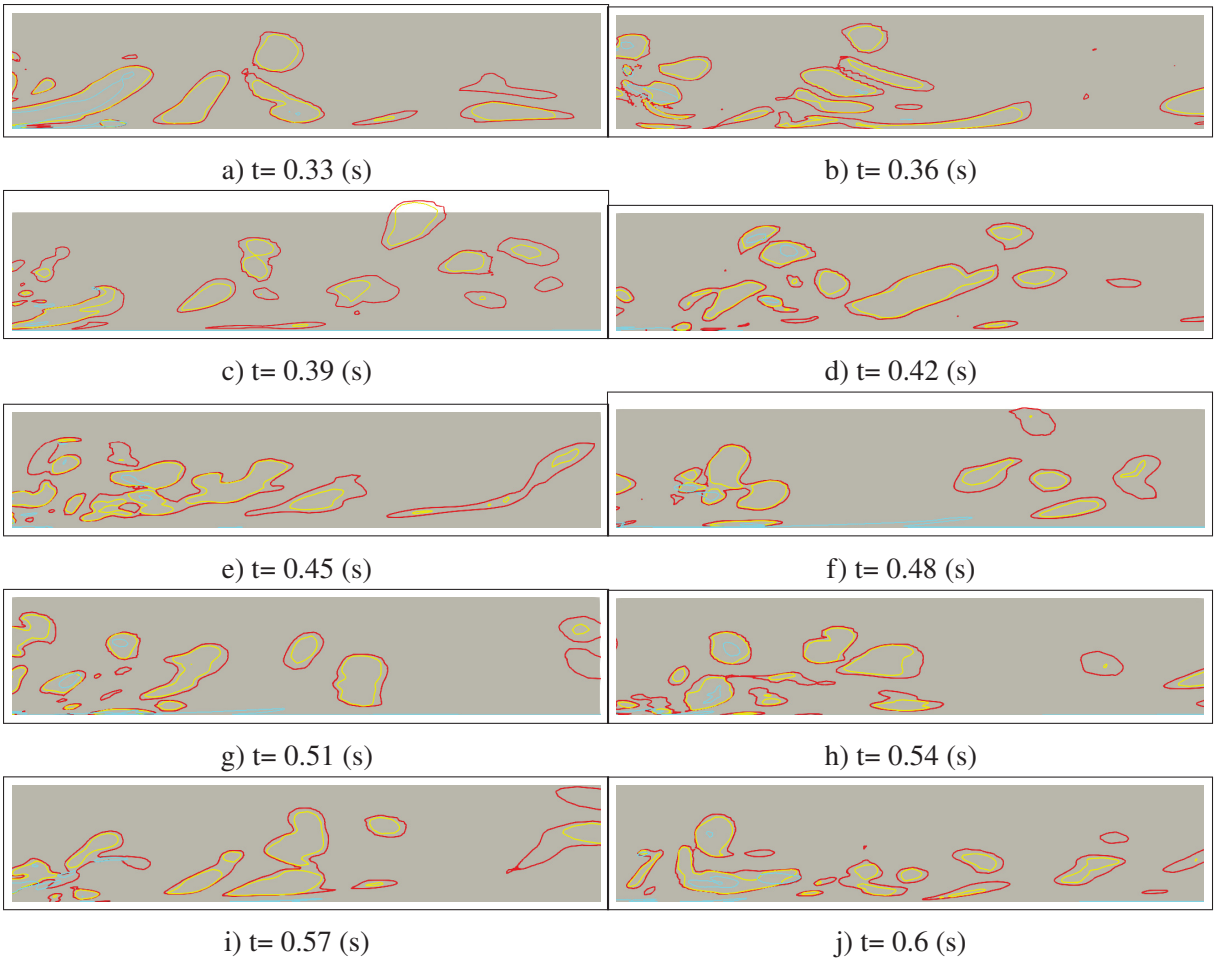

Figure 3.36 EDDES-M1, the second division of the WMH channel after the hump, where flow begins to reattach to the wall. This re-attachment region is from x/c= 1.25 to 2 (red : Q ; yellow : $\lambda 2$; blue : λ_{ci}^2)

The third division of the WMH channel is presented in Figure 3.37 before quantifying the vortices for the EDDES-M1 simulation. Given the return of the flow toward its original state, a decrease in discernible vortex structures is noticeable in this region. An important consideration to bear in mind is that, as suggested by Table 3.11, this segment is longer in the stream-wise direction compared with the other sections. A potential implication of this characteristic length could be a gradual decrease in turbulent activity as the fluid progresses along this extended path, further reducing the detectable vortex structures. We also observe that the λ_2 criterion commonly detects vortices within those identified by the Q-criterion. This phenomenon could imply that

λ_2 is adapted at recognizing more localized, smaller-scale vortices, potentially offering a more intricate view of the turbulent dynamics within larger vortex structures. Despite λ_{ci}^2 occasionally identifying stronger vortices, it's apparent that the quantity of captured vortices remains limited. There are also noticeable discrepancies near the wall. This limitation may hint at the criterion's sensitivity to wall-induced effects, which could potentially influence its effectiveness in detecting vortex structures near the wall.

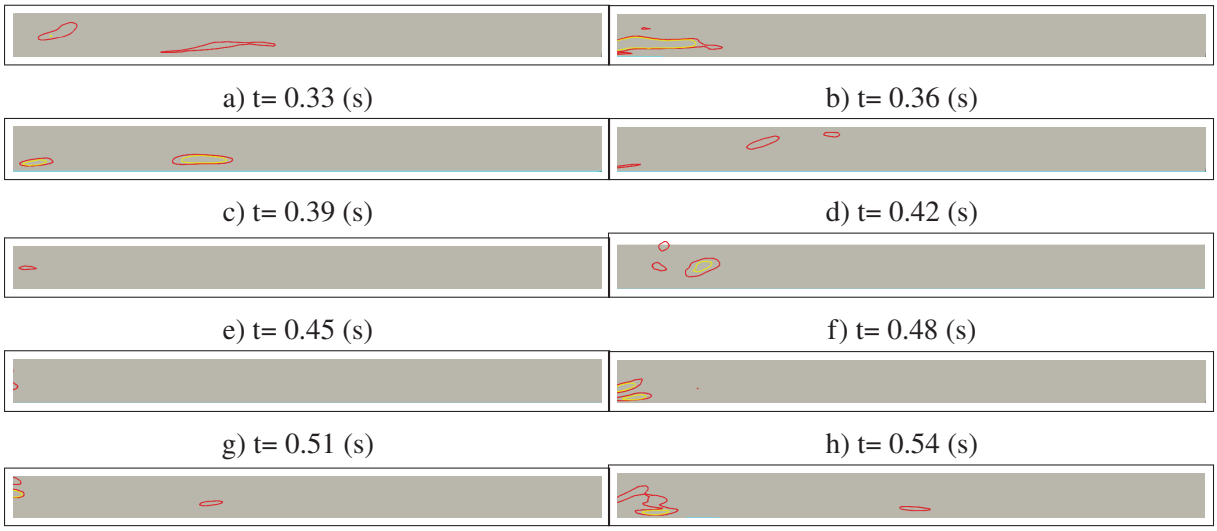

Figure 3.37 The third division of the WMH channel for the EDDES-M1 after the hump, where the flow enters the relaxation region. It is from x/c= 2 to 4
(red : Q ; yellow : $\lambda 2$; blue : λ_{ci}^2)

A quantitative study of the number of vortices in each section is then pursued. Counting the number of vortices is the easiest way to compare the credibility of vortex identification methods, since averaging the size or the vorticity is not trivial and requires to develop a specific tool. For all of the sections of the EDDES-M1, Table 3.13 shows the number of vortices using our three vortex identification methods. We can observe that in the shear-layer region, nearly in all time frames of this simulation, the Q-criterion method detects more vortices than the other two techniques (except 3.35f, where λ_2 had the same number of identified vortices). Moreover, it's worth noting that the Q-criterion, being sensitive to the strain rate of the fluid, might be more capable of detecting rotational structures in this high-strain region. This is consistent with the observation that this method often identifies a greater number of vortices. This trend is almost the same for the reattachment region except for 3.36e and 3.36h, where λ_2 identified more vortices. An interesting point is that the λ_2 criterion can sometimes detect more subtle vortex structures, as it is not strictly tied to the local strain rate. Each method only managed to identify less than three vortices in the relaxation region. There are not many vortices in the relaxation region because the flow is almost back to the state before separation. As a result, there are fewer vortices overall. We should also note that the vortices on the boundaries of each section location are counted in both sections. Therefore, there might be a minor error of around five percent in the overall number of vortices in the entire domain. moreover, it should be noted the average number of vortices and also the standard deviation values are rounded up since a fraction of a vortex is meaningless.

Table 3.13 Number of detected vortices using three different vortex identification methodologies for the EDDES-M1

	No	Fig no	Time	Q-criterion	λ_2 criterion	λ_{ci}^2
Section 1	1	3.35a	0.33	65	48	22
	2	3.35b	0.36	74	51	20
	3	3.35c	0.39	61	55	28
	4	3.35d	0.42	64	49	25
	5	3.35e	0.45	65	62	24
	6	3.35f	0.48	60	60	31
	7	3.35g	0.51	75	69	34
	8	3.35h	0.54	55	41	30
	9	3.35i	0.57	53	49	25
	10	3.35j	0.6	53	34	21
Average		-	-	**63**	**52**	**26**
Std Dev		-	-	**8**	**9**	**5**
Section 2	11	3.36a	0.33	13	11	5
	12	3.36b	0.36	20	16	7
	13	3.36c	0.39	18	16	4
	14	3.36d	0.42	21	15	5
	15	3.36e	0.45	11	15	7
	16	3.36f	0.48	12	11	3
	17	3.36g	0.51	19	14	3
	18	3.36h	0.54	12	14	3
	19	3.36i	0.57	9	11	7
	20	3.36j	0.6	16	14	6
Average		-	-	**14**	**14**	**5**
Std Dev		-	-	**4**	**3**	**2**
Section 3	21	3.37a	0.33	2	1	0
	22	3.37b	0.36	2	1	0
	23	3.37c	0.39	2	2	0
	24	3.37d	0.42	3	0	0
	25	3.37e	0.45	1	0	0
	26	3.37f	0.48	3	1	0
	27	3.37g	0.51	1	0	0
	28	3.37h	0.54	3	2	0
	29	3.37i	0.57	3	1	0
	30	3.37j	0.6	2	1	0
Average		-	-	**2**	**1**	**0**
Std Dev		-	-	**1**	**1**	**0**

Figure 3.38 shows the vortices found in ten distinct time frames for EDDES-M2 simulations using our vortex identification approaches. For EDDES-M1, EDDES-M2 and EDDES-M3 simulations time-steps were chosen based on identifying a period where the same trend of flow separation and re-attachment is observed through their time-steps.

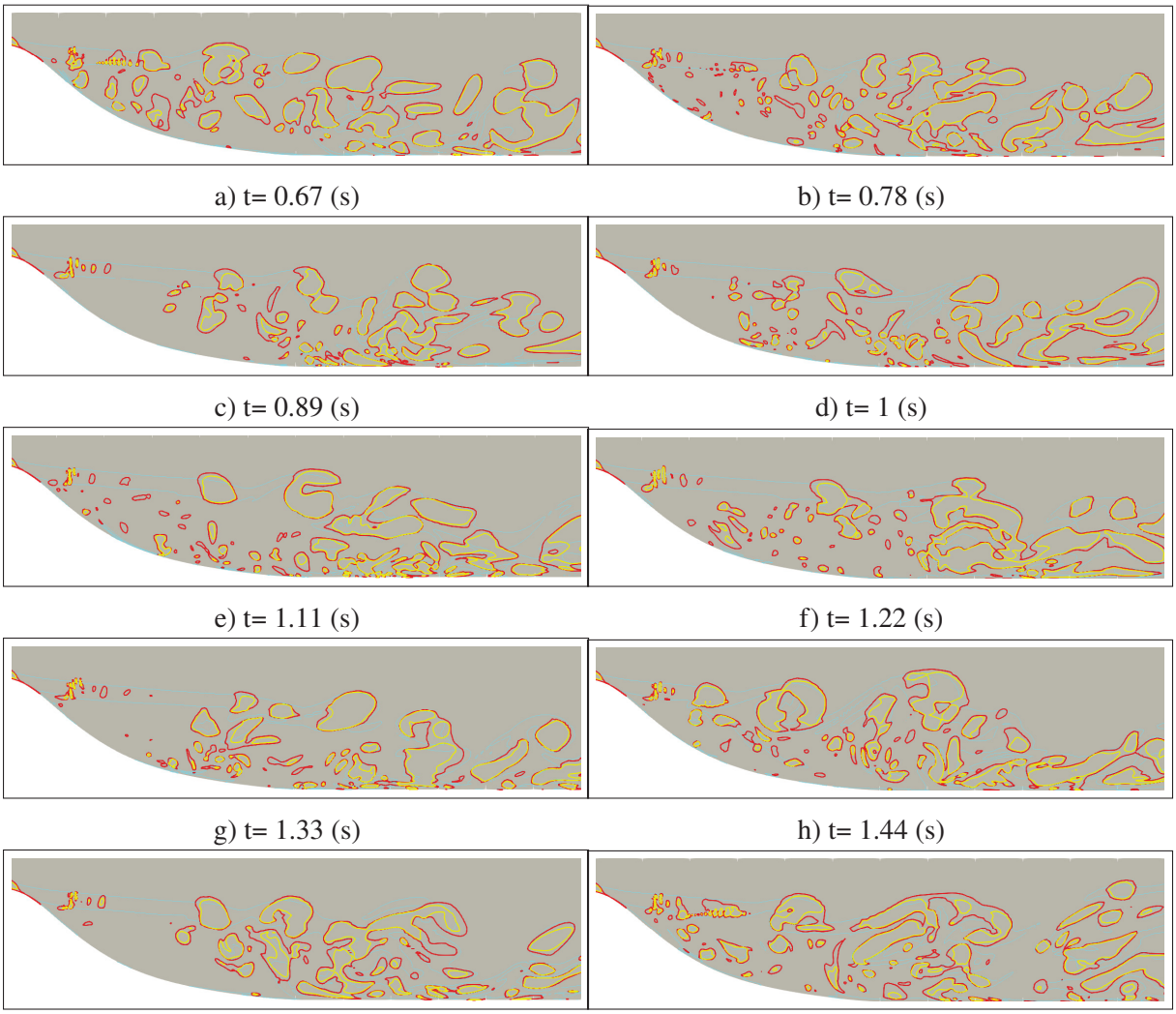

a) t= 0.67 (s) b) t= 0.78 (s)

c) t= 0.89 (s) d) t= 1 (s)

e) t= 1.11 (s) f) t= 1.22 (s)

g) t= 1.33 (s) h) t= 1.44 (s)

i) t= 1.55 (s) j) t= 1.66 (s)

Figure 3.38 EDDES-M2, the first division of the WMH channel after the hump where the flow gets separated from the wall. This shear layer region is from x/c= 0.65 to 1.25 (red : Q ; yellow : $\lambda 2$; blue : λ_{ci}^2)

For the EDDES-M2 simulation, Figure 3.39 illustrates the second division following the hump. The variation of vortices throughout different periods can be seen in each sub-figure. The vortices

that start to merge together are called interacted vortices (see for example Figure 3.39d). If we carefully examine, the λ_2 occasionally correctly identifies the interacted vortices individually, while Q-criterion identifies them as one in this threshold value.

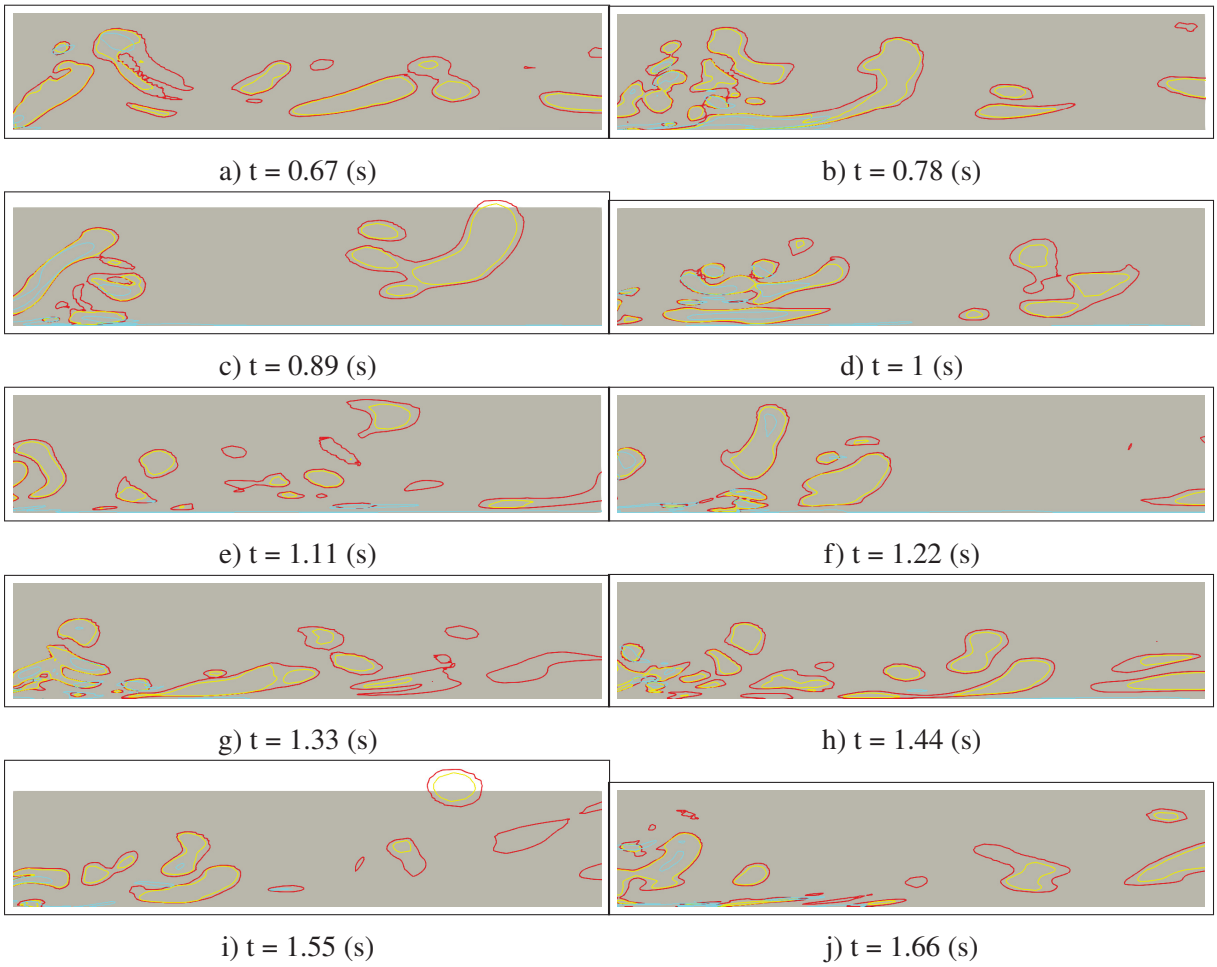

Figure 3.39 EDDES-M2, the second division of the WMH channel after the hump where the flow reattaches the wall. This period is from x/c = 1.25 to 2
(red : Q ; yellow : $\lambda 2$; blue : λ_{ci}^2)

Figure 3.40 shows the flow in ten different snapshots in the WMH channel final section following the hump. Although the number of identified vortices with λ_2 criterion is less than the Q-criterion, we can see that identified vortices with λ_2 criterion is in the middle of identified vortices using the Q-criterion. This will give the impression that with the comparable threshold value, λ_2 may have more level of precision in outlining the boundaries of interacted vortices.

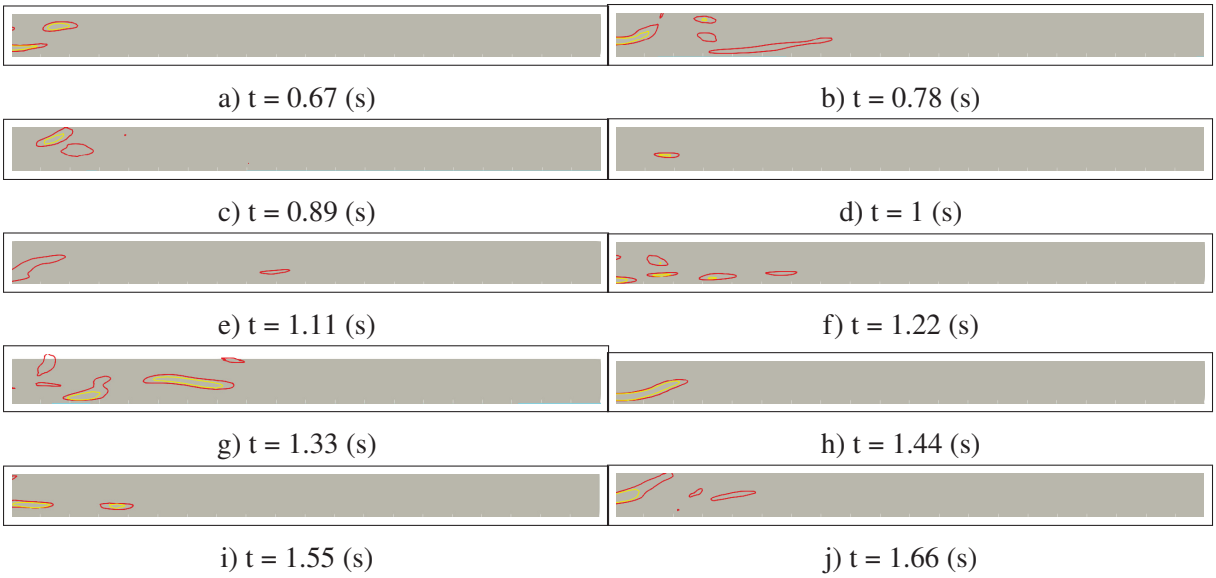

Figure 3.40 EDDES-M2, the third division of the WMH channel after the hump, in the relaxation region, from x/c = 2 to 4 (red : Q ; yellow : $\lambda 2$; blue : λ_{ci}^2)

The number of vortices following the hump is in Table 3.14. We will examine the number of vortices for the EDDES-M2 simulation over various time steps and sections in the table below. Once more, we can observe that the average number of vortices identified by Q-criterion is higher than other identification techniques. If we compare the average values between EDDES-M1 and EDDES-M2 simulation, we can see that EDDES-M2 has fewer average values compared to EDDES-M1. The only exception is the average number of identified vortices, with λ_2 in EDDES-M2 being higher than in EDDES-M1 in section 1.

Table 3.14 Quantity of detected vortices using three different vortex identification methodologies for the EDDES-M2

	No	Fig no	Time	Q-criterion	λ_2 criterion	λ_{ci}^2
Section 1	1	3.38a	0.67	59	60	23
	2	3.38b	0.78	79	65	22
	3	3.38c	0.89	52	50	22
	4	3.38d	1	63	53	25
	5	3.38e	1.11	67	52	30
	6	3.38f	1.22	52	45	13
	7	3.38g	1.33	61	50	23
	8	3.38h	1.44	56	53	22
	9	3.38i	1.55	45	41	17
	10	3.38j	1.66	67	72	24
Average		-	-	**60**	**54**	**22**
Std Dev		-	-	**9**	**9**	**4**
Section 2	11	3.39a	0.67	12	10	4
	12	3.39b	0.78	13	16	7
	13	3.39c	0.89	9	9	4
	14	3.39d	1	13	15	10
	15	3.39e	1.11	17	12	3
	16	3.39f	1.22	12	10	7
	17	3.39g	1.33	15	13	14
	18	3.39h	1.44	16	18	6
	19	3.39i	1.55	12	8	6
	20	3.39j	1.66	15	9	6
Average		-	-	**12**	**11**	**6**
Std Dev		-	-	**3**	**3**	**3**
Section 3	21	3.40a	0.67	3	2	0
	22	3.40b	0.78	5	2	0
	23	3.40c	0.89	3	1	0
	24	3.40d	1	1	1	0
	25	3.40e	1.12	2	0	0
	26	3.40f	1.22	6	4	0
	27	3.40g	1.33	6	2	0
	28	3.40h	1.44	1	1	0
	29	3.40i	1.55	3	2	0
	30	3.40j	1.66	4	1	0
Average		-	-	**3**	**2**	**0**
Std Dev		-	-	**2**	**1**	**0**

Figure 3.41 depicts the vortical structures for EDDES-M3 simulations across six sequential time-steps. Compared to the first two simulations, the overall number of vortices has risen. Moreover, the improvement of the λ_{ci}^2 technique in capturing more vortices grabs the interest. More vortices are captured with the same threshold value in this finer mesh. Moreover, we can see that the identified vortices using λ_{ci}^2 cannot distinguish the interacted vortices very well and are connected in most regions.

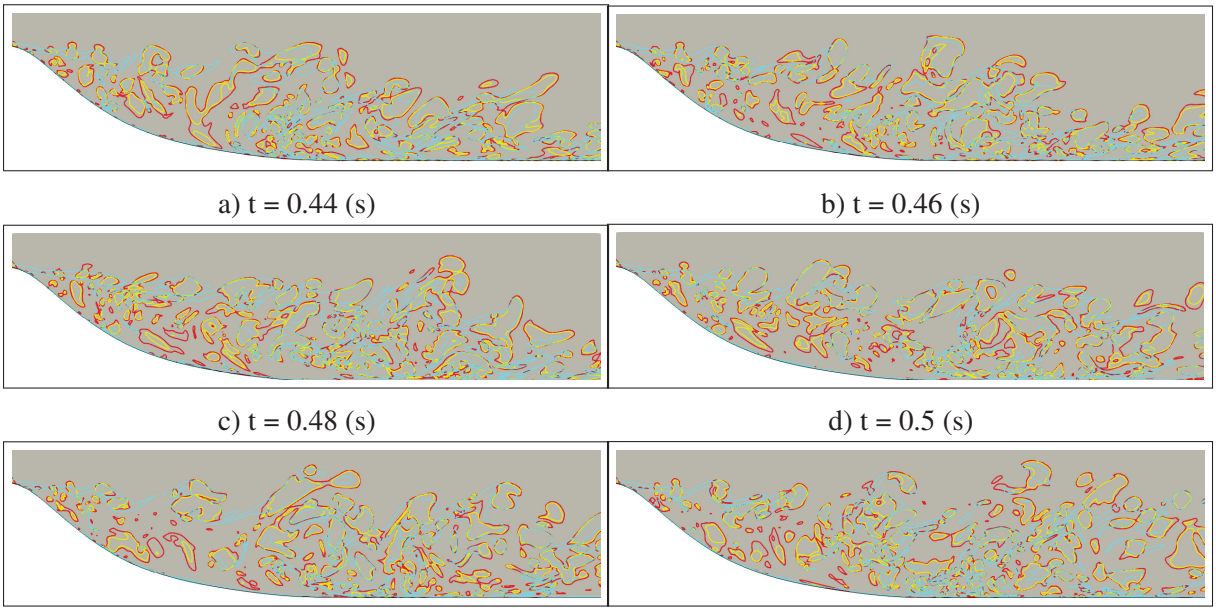

Figure 3.41 EDDES-M3, the first division of the WMH channel after the hump, in the shear layer region, from x/c = 0.65 to 1.25 (red : Q ; yellow : $\lambda 2$; blue : λ_{ci}^2)

The EDDES-M3 simulation second section is seen in Figure 3.42. In this re-attachment region, we observe more vortices than in the first two simulations. The interactions between the vortices continue as they move away from the wall, and as was already mentioned, the λ_2 is better at identifying the boundary between interacted vortices than the Q is. Furthermore, in this simulation we see more identified vortices with the λ_{ci}^2 method.

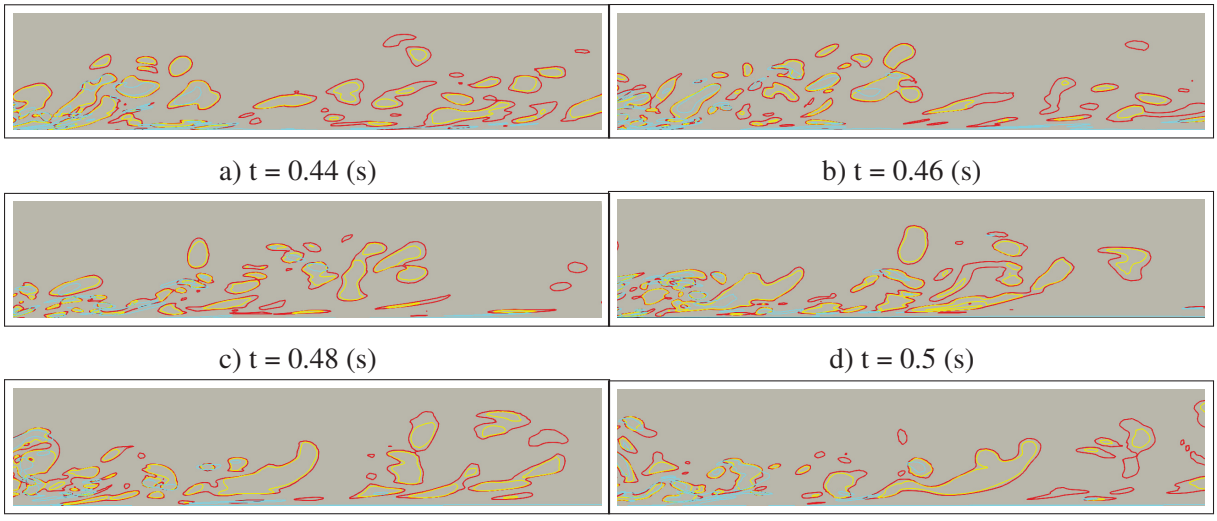

a) t = 0.44 (s) b) t = 0.46 (s)

c) t = 0.48 (s) d) t = 0.5 (s)

e) t = 0.52 (s) f) t = 0.54 (s)

Figure 3.42 EDDES-M3, the second section of the WMH channel after the hump, in the reattachment area, from x/c = 1.25 to 2 (red : Q ; yellow : $\lambda 2$; blue : λ_{ci}^2)

The relaxation region is shown in different time steps for the EDDES-M3 simulations in Figure 3.43. We can notice that the λ_{ci}^2 captures vortices in this area, which were not previously captured in the first two simulations. The number of captured vortices in this section is almost higher by a factor of 5 than in the first two simulations. Moreover, in the second half of this section (from x/c= 3 to 4), only three vortices are captured by Q-criterion in this threshold value in all of our EDDES simulations.

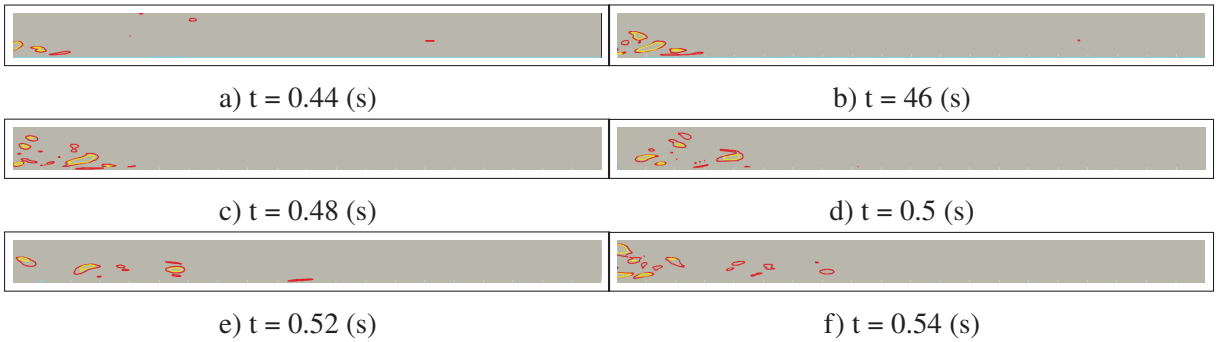

a) t = 0.44 (s) b) t = 46 (s)

c) t = 0.48 (s) d) t = 0.5 (s)

e) t = 0.52 (s) f) t = 0.54 (s)

Figure 3.43 EDDES-M3, the third section of the WMH channel after the hump, in the relaxation region, from x/c = 2 to 4 (red : Q ; yellow : $\lambda 2$; blue : λ_{ci}^2)

Table 3.15 is the last quantification of number of identified vortices in the various sections for the EDDES-M3 simulation. Previously, in the first two simulations, the λ_{ci}^2 identified only few vortices. However, it is now capable of doing so even in the relaxation region. Unexpectedly, we also observe that λ_2 in this simulation has discovered more vortices than Q, especially in the shear layer region. We need more vortices observation and other identifying techniques to conclude about the validity of the detected vortices at different threshold values.

Table 3.15 Quantity of detected vortices for the EDDES-M3 using three different vortex identification techniques

	No	**Fig no**	**Time**	**Q-criterion**	λ_2 **criterion**	λ_{ci}^2
Section 1	1	3.41a	0.44	79	90	61
	2	3.41b	0.46	97	104	67
	3	3.41c	0.48	100	105	74
	4	3.41d	0.5	98	108	78
	5	3.41e	0.52	96	109	59
	6	3.41f	0.54	105	112	71
Average		-	-	**96**	**105**	**68**
Std Dev		-	-	**9**	**8**	**7**
Section 2	7	3.42a	0.44	40	35	20
	8	3.42b	0.46	50	37	22
	9	3.42c	0.48	41	38	18
	10	3.42d	0.5	35	35	26
	11	3.42e	0.52	37	38	15
	12	3.42f	0.54	37	25	15
Average		-	-	**40**	**35**	**19**
Std Dev		-	-	**5**	**5**	**4**
Section 3	13	3.43a	0.44	7	3	1
	14	3.43b	0.46	8	4	0
	15	3.43c	0.48	16	5	0
	16	3.43d	0.5	14	4	1
	17	3.43e	0.52	9	3	1
	18	3.43f	0.54	15	5	0
Average		-	-	**13**	**4**	**1**
Std Dev		-	-	**4**	**1**	**1**

In the final step, we have compiled the average number of identified vortices and their standard deviation from each section of the WMH across all our EDDES simulations into histograms. Figure 3.44 shows the histograms of average number of identified vortices using our different identification techniques.

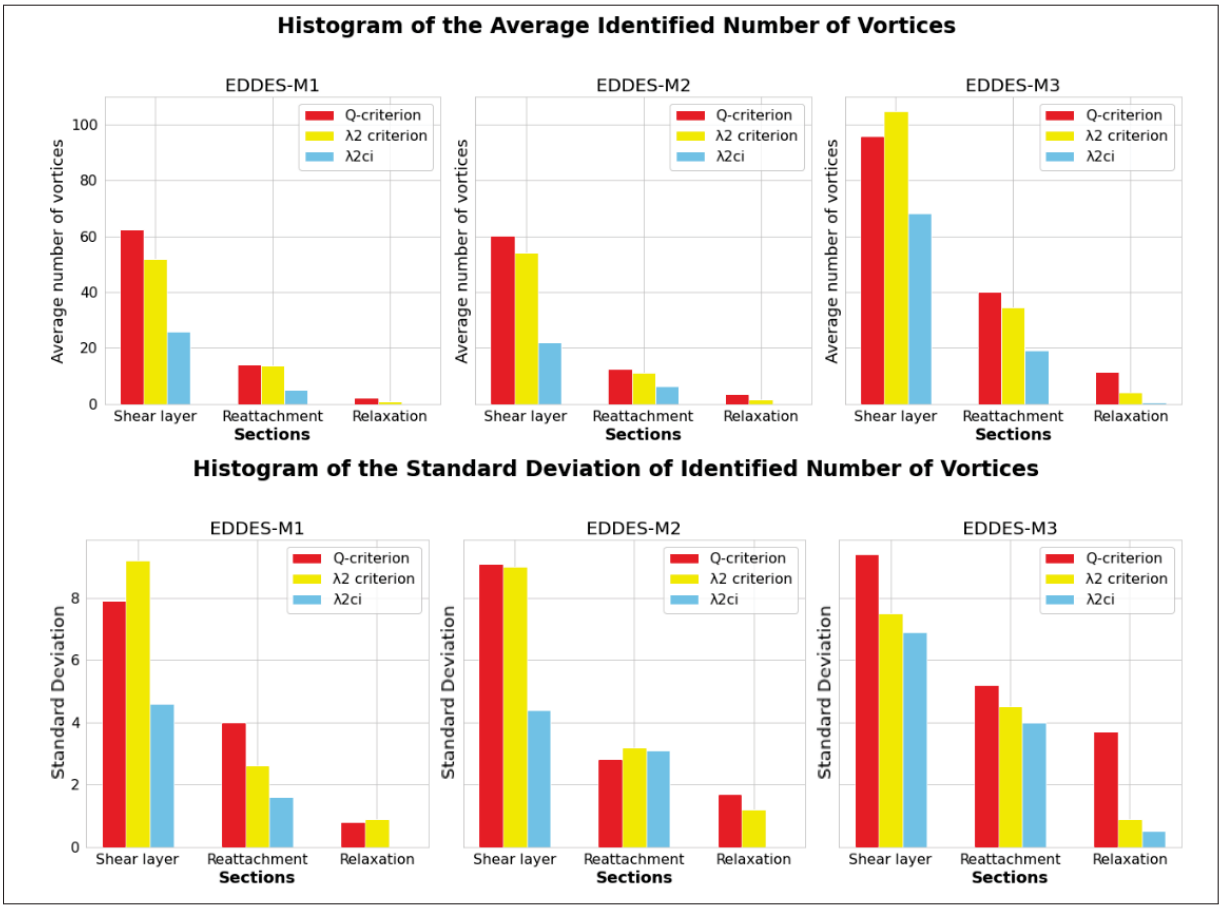

Figure 3.44 Comparison of the average and standard deviation of vortices identified per section across our three distinct identification technique

Our analysis reveals a noticeable trend in the detection of vortices across all methodologies for each simulation (EDDES-M1, EDDES-M2, EDDES-M3), showing a decrease in the number of vortices from section one to section three. This downward trend is most evident in the Q-criterion method, where section one consistently shows higher vortex counts compared to other sections, regardless of the simulation.

Adding to this, it's also worth considering that the higher count in the first section could be due to the intense turbulence that characterizes the separation region, where vortex generation is typically at its peak. This reflects the fact that in the separation region we have the most turbulent and complex flow patterns. In other words, it indicates that Q-criterion loses the precision of identifying the vortices in the relaxation and reattachment region as it identified more vortices with a closer look at standard deviations from this study. This could further suggest that while Q-criterion excels in regions of high turbulence, its performance may diminish in less turbulent or more stable flow regions, thus impacting its effectiveness across different regions that requires lower threshold value to identify those vortices.

Regarding the average vortex counts, EDDES-M3 significantly captures more vortices than the other two simulations in all three identification techniques. It demonstrates remarkably high counts, especially for the λ_2 criterion and λ_{ci}^2 in section one. This indicates the higher sensitivity and the presence of more complex vortex structures in the EDDES-M3 simulation with a finer mesh. Additionally, the higher vortex count in the EDDES-M3 simulation might also hint at the simulation's ability to resolve smaller-scale or finer vortices, owing to a higher resolution mesh. On the other hand, upon observing the standard deviations, we see relatively higher variations in the vortex count in the initial sections in all simulations. While this variability decreases across the sections, it is notable that it remains relatively high in EDDES-M3, suggesting more complex and diverse vortex structures. These standard deviations might also be indicative of the inherent unsteadiness of the flow, where higher standard deviations imply more fluctuating flow conditions.

To conclude, the λ_2 criterion reveals its strength in the WMH test case, specifically in the complex flow situations shown in the EDDES-M3 simulation. We have also seen earlier and vortex interactions better than other techniques. The effectiveness of the λ_2 criterion in these situations might be attributed to its inherent ability to discern the cores of vortices irrespective of the vortex strength. The ability of the λ_2 criterion to identify these points sets it apart from the other methods, particularly in more complex flow scenarios like in the EDDES-M3 simulation. While each identification technique has its superiority, the λ_2 criterion adeptness at capturing

intricate vortex interactions makes it particularly suited to the task at hand. Its application in the EDDES-M3 simulation leads to a more comprehensive representation of the vortex dynamics in the flow over the WMH, thereby highlighting its potential use in analyzing complex turbulent flows.

In this section, we defined the methodology we took to identify the vortices. After creating sections on the WMH channel, we counted the number of vortices in each section using the three distinct identification methodologies on the EDDES solutions. Finally, we used the average and standard deviation of the number of vortices for further analysis of the vortex identification techniques.

CONCLUSION AND RECOMMENDATIONS

In this work, we highlighted the crucial role of turbulent flow comprehension and its significant importance in real-world scenarios. Our investigation began with a thorough literature review, focusing on the WMH test case that can be interpreted as ice accretion on a wing of an airplane (a common and hazardous aviation phenomenon). Our work utilized the open-source SU2, which holds potential for further advancements and enhancements. Through our analysis, we shed light on the limitations of RANS methodologies in dealing with separated flows, thereby emphasizing the necessity to refine hybrid RANS/LES methods. Our research is one of the first investigations employing these hybrid models in the WMH test case within the context of the SU2 platform. Furthermore, we defined the distinctive features of three widely-recognized Eulerian vortex identification techniques (the Q-criterion, the λ_2 criterion, and Swirling Strength (λ_{ci}^2)). Notably, no prior study has undertaken a comparative examination of these identification techniques applied to the WMH. Consequently, our research fills this gap and provides a new comparison of the vortex identification techniques in such complex turbulent flows in a well-known test-case.

Our investigation into the separation and reattachment locations of the WMH began with five distinctive grids for the RANS approach. We started with a comprehensive analysis of the flow characteristics, such as velocity profiles, pressure, and the skin friction coefficient along the wall and in 2D. Despite the recognized limitations of the RANS methodology, particularly in pinpointing the reattachment location, showed good agreement with the RANS results in the literature, demonstrating a significant degree of validity. Subsequently, to identify a suitable grid for unsteady simulations, we determined the errors in aerodynamic coefficients associated with each grid. Generally, these errors displayed a declining trend with the increase in grid density. Moreover, we conducted a rigorous study to estimate the GCI errors, which showed that further grid refinement is not necessary for RANS solution.

From our RANS grids, we modified three grids for the EDDES simulations, one having twice the spanwise size. We analyzed the different time-averaged periods to omit the transient flow from these unsteady simulations and find the most suitable periods for time averaging. Then, we investigated the aerodynamic coefficients along the wall in various span locations and averaged these locations to get a spatial average. We have compared the outcomes with the experimental and the literature findings. In these findings, we saw that the gray area issue still causes the delay from the transition of RANS to LES in the separation region. This had consequences on the reattachment location occurring later (further downstream) than in the experiment and some of the results from the literature. After careful analysis, we found that one of the potential issues could be the accuracy level of the solver in estimating viscous fluxes. To simplify, it seems like the solver might not be precise enough when it comes to handling these complex calculations, which might explain the longer separation (gray area issue). Interestingly, the EDDES-M2 having more extensive spanwise length and twice sampling sizes for the spatial averaging, had smoother time and space-averaged aerodynamic coefficients compared to the other two simulations.

Finally, in our primary research objective, using our three EDDES simulations, we compared the number of vortices in three critical sections after the hump in the WMH channel. We used the previously mentioned identification methods for the first time on the WMH for a comparative analysis. This exercise permitted us to evaluate the performance of these techniques, which highlights the λ_2 criterion remarkable capability. For this analysis, we have examined the identified vortices and counted the number of each identified vortex for each section. It's worth mentioning that the λ_2 criterion demonstrated superior performance in outlining the boundaries of interacted vortices in the same threshold value than the one already identified for the Q-criterion, with more precision compared with the other two techniques.

Despite its strengths, we also recognized some limitations with the λ_{ci}^2 criterion. This method captures fewer vortices and indicates a larger vortex region along the wall. This suggests a less discriminating capability for detecting individual vortex structures, especially in the vicinity of the wall where the flow complexity is high within the selected threshold value. Therefore, analyzing different threshold values can be an area for future improvements in this criterion.

Furthermore, we collated these pieces of information into tables and histograms for further breakdown. Our comparative analysis underscored the shortcomings of the Q-criterion technique in identifying excessive vortices, particularly those in the reattachment and relaxation regions. Moreover, the Q-criterion technique consistently failed to capture individual vortices. Additionally, the impact of mesh density on vortex identification was evident, while the finer grid (EDDES-M3) revealed a higher number of vortices and more complex flow structures.

For further investigations, it is recommended to incorporate higher-order accuracy algorithms within the SU2 framework for the approximation of viscous fluxes. A potential area for future research might also be the development of a new vortex detection method that combines the strengths of existing criteria while addressing their limitations. This enhancement could improve precision and provide a deeper understanding of the gray area issue, which concerns the late transition between RANS and LES in hybrid RANS/LES methods.

Furthermore, in future works, the efficiency and precision of λ_2 can be leveraged in automating the process of creating sections and counting the number of vortices at critical stages of the WMH. This could facilitate the vortex identification procedure and possibly establish a universally practical tool for vortex detection in similar flow scenarios. This automation could involve machine learning or other computational techniques to effectively analyze complex turbulent flows and rapidly process extensive data. The potential integration of λ_2 with these techniques underscores an exciting prospect that can open up new possibilities for automation and accuracy in turbulence studies.

Vortex analysis using Lagrangian techniques could also be considered for future studies, as this approach enables the tracking of fluid particles over time, providing a unique perspective on vortex dynamics. This would suggest the potential for future studies to delve deeper into the evolution of vortices over time, which can contribute to a more dynamic understanding of turbulent flows. Given the strength of λ_2 in identifying vortex interactions, combining it with Lagrangian analysis could yield significant insights into vortex dynamics and interaction over time.

BIBLIOGRAPHY

Allmaras, S., Johnson, F. & Spalart, P. (2012). Modifications and clarifications for the implementation of the Spalart-Allmaras turbulence model. *Seventh International Conference on Computational Fluid Dynamics (ICCFD7)*, 1-11.

Armstrong, T. B., Yang, H. Q. & Harris, R. E. (2022). Large Eddy Simulation of NASA Hump Using High-Order Spatial Scheme with Curved Mesh in COFFE. In *AIAA AVIATION 2022 Forum*. doi: 10.2514/6.2022-3625.

Balakumar, P. (2005). Computations of Flow over a Hump Model Using Higher Order Method with Turbulence Modeling. *43rd AIAA Aerospace Sciences Meeting and Exhibit*. doi: 10.2514/6.2005-1270.

Bardina, J., Huang, P. & Coakley, T. (1997). Turbulence modeling validation. *28th Fluid Dynamics Conference*.

Bendjebbas, H., Abdellah-ElHadj, A. & Abbas, M. (2016). Full-scale, wind tunnel and CFD analysis methods of wind loads on heliostats: A review. *Renewable and Sustainable Energy Reviews*, 54, 452–472. doi: 10.1016/j.rser.2015.10.031.

Blazek, J. (2015). *Computational Fluid Dynamics : Principles and Applications*. Elsevier Ltd, third edition.

Borgmann, D., Pande, A., Little, J. C. & Woszidlo, R. (2017). Experimental Study of Discrete Jet Forcing for Flow Separation Control on a Wall Mounted Hump. In *55th AIAA Aerospace Sciences Meeting* (pp. 1). doi: 10.2514/6.2017-1450.

Bozinoski, R. & Davis, R. L. (2012). A DES Procedure Applied to a Wall-Mounted Hump. *International Journal of Aerospace Engineering*, 2012, 1–11. doi: 10.1155/2012/149461.

Breuer, M., Jovičić, N. & Mazaev, K. (2003). Comparison of DES, RANS and LES for the separated flow around a flat plate at high incidence. *International Journal for Numerical Methods in Fluids*, 41(4), 357 – 388. doi: 10.1002/fld.445.

Cabral, B. & Leedom, L. C. (1993). Imaging Vector Fields Using Line Integral Convolution. *Proceedings of the 20th Annual Conference on Computer Graphics and Interactive Techniques*, (SIGGRAPH '93), 263–270. doi: 10.1145/166117.166151.

Canivete Cuissa, J. R. & Steiner, O. (2022). Innovative and automated method for vortex identification - I. Description of the SWIRL algorithm. *A&A*, 668, A118. doi: 10.1051/0004-6361/202243740.

Chakraborty, P., Balachandar, S. & Adrian, R. J. (2005). On the relationships between local vortex identification schemes. *Journal of Fluid Mechanics*, 535, 189–214. doi: 10.1017/S0022112005004726.

Chong, M. S., Perry, A. E. & Cantwell, B. J. (1990). A general classification of three-dimensional flow fields. *Physics of Fluids A: Fluid Dynamics*, 2(5), 765–777. doi: 10.1063/1.857730.

Chávez-Modena, M., Martínez, J., Cabello, J. & Ferrer, E. (2020). Simulations of aerodynamic separated flows using the lattice boltzmann solver XFlow. *Energies*, 13(19). doi: 10.3390/en13195146.

Constantinescu, G., Chapelet, M. & Squires, K. (2003). Turbulence modeling applied to flow over a sphere. *AIAA Journal*, 41(9), 1733 – 1742. doi: 10.2514/2.7291.

Corson, D., Jaiman, R. & Shakib, F. (2009). Industrial application of RANS modelling: capabilities and needs. *International Journal of Computational Fluid Dynamics*, 23(4), 337–347. doi: 10.1080/10618560902776810.

Cui, J. & Agarwal, R. (2005). CFD Validation of Turbulent Separation Control on a 2D Hump (NASA Langley Workshop Validation: Case 3). *35th AIAA Fluid Dynamics Conference and Exhibit*. doi: 10.2514/6.2005-5013.

Cyklis, P. & Młynarczyk, P. (2016). The Influence of the Spatial Discretization Methods on the Nozzle Impulse Flow Simulation Results. *Procedia Engineering*, 157, 396–403. doi: 10.1016/j.proeng.2016.08.382.

Deck, S. (2012). Recent improvements in the Zonal Detached Eddy Simulation (ZDES) formulation. *Theoretical and Computational Fluid Dynamics*, 26(6), 523–550. doi: 10.1007/s00162-011-0240-z.

Deck, S. & Renard, N. (2020). Towards an enhanced protection of attached boundary layers in hybrid RANS/LES methods. *Journal of Computational Physics*, 400. doi: 10.1016/j.jcp.2019.108970.

Devaux, Y., Thomas, L., Calluaud, D. & Pineau, G. (2020). Isolated columnar vortex generation: influence of momentum impulsion characteristics and wall roughness. *Fluid Dynamics Research*, 52(2), 025511. doi: 10.1088/1873-7005/ab7ebf.

DeVries, B., Iannelli, J., Trefftz, C., O'Hearn, K. A. & Wolffe, G. (2013). Parallel Implementations of FGMRES for Solving Large, Sparse Non-symmetric Linear Systems. *Procedia Computer Science*, 18, 491–500. doi: https://doi.org/10.1016/j.procs.2013.05.213.

Dietiker, J.-F. & Hoffmann, K. A. (2009). Predicting Wall Pressure Fluctuation over a Backward-Facing Step Using Detached Eddy Simulation. *Journal of Aircraft*, 46(6), 2115-2120. doi: 10.2514/1.43912.

Dilip, D. & Tafti, D. (2014). Wall Modeled Large Eddy Simulation of Flow Over a Wall-Mounted Hump. *Volume 1A, Symposia: Advances in Fluids Engineering Education; Turbomachinery Flow Predictions and Optimization; Applications in CFD; Bio-Inspired Fluid Mechanics; Droplet-Surface Interactions; CFD Verification and Validation; Development and Applications of Immersed Boundary Methods; DNS, LES, and Hybrid RANS/LES Methods*, pp. V01AT09A010. doi: 10.1115/FEDSM2014-21517.

Dong, Y., Yan, Y. & Liu, C. (2016). New visualization method for vortex structure in turbulence by lambda2 and vortex filaments. *Applied Mathematical Modelling*, 40(1), 500–509. doi: https://doi.org/10.1016/j.apm.2015.04.059.

Eaton, J. K. & Johnston, J. P. (1981). A Review of Research on Subsonic Turbulent Flow Reattachment. *AIAA Journal*, 19(9), 1093-1100. doi: 10.2514/3.60048.

Economon, T. D., Palacios, F., Copeland, S. R., Lukaczyk, T. W. & Alonso, J. J. (2016). SU2: An Open-Source Suite for Multiphysics Simulation and Design. *AIAA Journal*, 54(3), 828–846. doi: 10.2514/1.J053813.

Fagbade, A. & Heinz, S. (2022). Application of Mode-Controlled Hybrid RANS-LES to the NASA Wall-Mounted Hump Flow. In *AIAA SCITECH 2022 Forum*. doi: 10.2514/6.2022-0180.

Fasel, H. F. & Postl, D. (2006). INTERACTION OF SEPARATION AND TRANSITION IN BOUNDARY LAYERS: DIRECT NUMERICAL SIMULATIONS. In Govindarajan, R. (Ed.), *IUTAM Symposium on Laminar-Turbulent Transition* (vol. 78, pp. 71–88). Dordrecht: Kluwer Academic Publishers. doi: 10.1007/1-4020-4159-4_7.

Fatahian, H., Salarian, H., Eshagh Nimvari, M. & Khaleghinia, J. (2020). Effect of Gurney flap on flow separation and aerodynamic performance of an airfoil under rain and icing conditions. *Acta Mechanica Sinica*, 36(3), 659–677. doi: 10.1007/s10409-020-00938-3.

Franck, J. & Colonius, T. (2008). Large-Eddy Simulation of Separation Control for Compressible Flow Over a Wall-Mounted Hump. In *46th AIAA Aerospace Sciences Meeting and Exhibit*. doi: 10.2514/6.2008-555.

Fröhlich, J. & von Terzi, D. (2008). Hybrid LES/RANS methods for the simulation of turbulent flows. *Progress in Aerospace Sciences*, 44(5), 349-377. doi: https://doi.org/10.1016/j.paerosci.2008.05.001.

Gao, J. & Li, X. (2017). Implementation of Delayed Detached Eddy Simulation method to a high order spectral difference solver. *Computers and Fluids*, 154, 90 – 101. doi: 10.1016/j.compfluid.2017.05.035.

Gomar, A,. (2022). ANTARES: Python post processing library, Ver 1.18.0. CERFACS (fr). Retrieved from: HTTP://www.cerfacs.fr/antares.

Graftieaux, L., Michard, M. & Grosjean, N. (2001). Combining PIV, POD and vortex identification algorithms for the study of unsteady turbulent swirling flows. *Measurement Science and Technology*, 12(9), 1422–1429. doi: 10.1088/0957-0233/12/9/307.

Greenblatt, D., Paschal, K. B., Yao, C.-S., Harris, J., Schaeffler, N. W. & Washburn, A. E. (2006). Experimental Investigation of Separation Control Part 1: Baseline and Steady Suction. *AIAA Journal*, 44(12), 2820–2830. doi: 10.2514/1.13817.

Gritskevich, M. S., Garbaruk, A. V., Schütze, J. & Menter, F. R. (2012). Development of DDES and IDDES formulations for the k-ω shear stress transport model. *Flow, Turbulence and Combustion*, 88(3), 431 – 449. doi: 10.1007/s10494-011-9378-4.

Guseva, E. K., Garbaruk, A. V. & Strelets, M. K. (2017). Assessment of Delayed DES and Improved Delayed DES Combined with a Shear-Layer-Adapted Subgrid Length-Scale in Separated Flows. *Flow, Turbulence and Combustion*, 98(2), 481–502. doi: 10.1007/s10494-016-9769-7.

Haller, G. & Beron-Vera, F. J. (2013). Coherent Lagrangian vortices: the black holes of turbulence. *Journal of Fluid Mechanics*, 731, R4. doi: 10.1017/jfm.2013.391.

Hao, L., Wei, L. & Shengye, W. (2021). Numerical Investigation of Fixed and Non-fixed Separation with Shear Layer Adapted Delayed Detached Eddy Simulation. *International Journal of Aeronautical and Space Sciences*, 22(3), 531–546. doi: 10.1007/s42405-020-00342-y.

Hasanzadeh Lashkajani, K. (2015). *Reynolds-averaged Navier-Stokes based ice accretion for aircraft wings*. (PhD Thesis, Ecole Polytechnique, Montreal (Canada)).

He, C., Corke, T. & Patel, M. (2007). Numerical and Experimental Analysis of Plasma Flow Control over a Hump Model. *45th AIAA Aerospace Sciences Meeting and Exhibit*. doi: 10.2514/6.2007-935.

Hirsch, C. (2007). The Analysis of Numerical Schemes. In Hirsch, C. (Ed.), *Numerical Computation of Internal and External Flows (Second Edition)* (ed. Second Edition, pp. 279–281). Oxford: Butterworth-Heinemann. doi: https://doi.org/10.1016/B978-075066594-0/50048-5.

Hodson, T. O. (2022). Root-mean-square error (RMSE) or mean absolute error (MAE): when to use them or not. *Geoscientific Model Development*, 15(14), 5481–5487. doi: 10.5194/gmd-15-5481-2022.

Hong, G.-R., Pedrizzetti, G., Tonti, G., Li, P., Wei, Z., Kim, J. K., Baweja, A., Liu, S., Chung, N., Houle, H., Narula, J. & Vannan, M. A. (2008). Characterization and Quantification of Vortex Flow in the Human Left Ventricle by Contrast Echocardiography Using Vector Particle Image Velocimetry. *JACC: Cardiovascular Imaging*, 1(6), 705-717. doi: 10.1016/j.jcmg.2008.06.008.

Hu, Q., Li, Z., Wang, L., Huang, Y., Wang, Y. & Li, L. (2019). Rainfall Spatial Estimations: A Review from Spatial Interpolation to Multi-Source Data Merging. *Water*, 11(3). doi: 10.3390/w11030579.

Huang, Y. (2017). Tracking coherent structures in massively-separated and turbulent flows.

Huang, Y. & Green, M. A. (2015). Detection and tracking of vortex phenomena using Lagrangian coherent structures. *Experiments in Fluids*, 56(7), 147. doi: 10.1007/s00348-015-2001-z.

Hunt, J. C. R. and Wray, A., and Moin, P . (1988). Eddies, streams, and convergence zones in turbulent flows.Technical report, NASA Document.

Im, H.-S. & Zha, G.-C. (2014a). Delayed Detached Eddy Simulation of Airfoil Stall Flows Using High-Order Schemes. *Journal of Fluids Engineering, Transactions of the ASME*, 136(11). doi: 10.1115/1.4027813.

Im, H.-S. & Zha, G.-C. (2014b). Delayed Detached Eddy Simulation of Airfoil Stall Flows Using High-Order Schemes. *Journal of Fluids Engineering*, 136(11). doi: 10.1115/1.4027813.

Iyer, P. S. & Malik, M. R. (2016). Wall–modeled Large Eddy Simulation of Flow Over a Wall–mounted Hump. *46th AIAA Fluid Dynamics Conference*. doi: 10.2514/6.2016-3186.

Jacob, M. C., Louisot, A., Juvé, D. & Guerrand, S. (2001). Experimental Study of Sound Generated by Backward-Facing Steps Under Wall Jet. *AIAA Journal*, 39(7), 1254-1260. doi: 10.2514/2.1467.

Jain, N. & Baeder, J. D. (2015). *Investigation of hybrid RANS-LES methods to understand their predictive capabilities in flows with separation*. doi: 10.2514/6.2015-1978.

Javaherchi, T. (2010). Review of the Spalart-Allmaras Turbulence Model and its Modifications. Tech. Rep., 2.

Jeong, J. & Hussain, F. (1995). On the identification of a vortex. *Journal of Fluid Mechanics*, 285, 69–94. doi: 10.1017/S0022112095000462.

Kalitzin, G., Medic, G., Iaccarino, G. & Durbin, P. (2005). Near-wall behavior of RANS turbulence models and implications for wall functions. *Journal of Computational Physics*, 204(1), 265 – 291. doi: 10.1016/j.jcp.2004.10.018.

Kalsi, H. S. & Tucker, P. G. (2016). A Novel Zonal RANS-DES Method for Prediction of Accelerated and Separated Flow. In *54th AIAA Aerospace Sciences Meeting* (pp. 12). doi: 10.2514/6.2016-1834.

Keep, J. A., Vitale, S., Pini, M. & Burigana, M. (2017). Preliminary verification of the open-source CFD solver SU2 for radial-inflow turbine applications. *Energy Procedia*, 129, 1071-1077. doi: https://doi.org/10.1016/j.egypro.2017.09.130. 4th International Seminar on ORC Power SystemsSeptember 13-15th 2017POLITECNICO DI MILANOBOVISA CAMPUSMILANO, ITALY.

Kiris, C. C., Stich, D., Housman, J. A., Kocheemoolayil, J. G., Barad, M. F. & Cadieux, F. (2018). Application of Lattice Boltzmann and Navier-Stokes Methods to NASA's Wall Mounted Hump. In *2018 Fluid Dynamics Conference*. doi: 10.2514/6.2018-3855.

Kitamura, K. (2016). Assessment of SLAU2 and Other Flux Functions with Slope Limiters in Hypersonic Shock-Interaction Heating. *Computers and Fluids*, 129. doi: 10.1016/j.compfluid.2016.02.006.

Kolář, V. & Šístek, J. (2022). Disappearing vortex problem in vortex identification: Non-existence for selected criteria. *Physics of Fluids*, 34(7). doi: 10.1063/5.0099046. 071704.

Kolář, V. (2007). Vortex identification: New requirements and limitations. *International Journal of Heat and Fluid Flow*, 28(4), 638–652. doi: 10.1016/j.ijheatfluidflow.2007.03.004.

Krishnan, V., Squires, K. D. & Forsythe, J. R. (2006). Prediction of Separated Flow Characteristics over a Hump. *AIAA Journal*, 44(2), 252–262. doi: 10.2514/1.13174.

Krueger, P. S., Hahsler, M., Olinick, E. V., Williams, S. H. & Zharfa, M. (2019). Quantitative classification of vortical flows based on topological features using graph matching. *Proceedings of the Royal Society A: Mathematical, Physical and Engineering Sciences*, 475(2228), 20180897. doi: 10.1098/rspa.2018.0897.

Kundu, P. K., Cohen, I. M. & Dowling, D. R. (2016). About the Authors. In Kundu, P. K., Cohen, I. M. & Dowling, D. R. (Eds.), *Fluid Mechanics (Sixth Edition)* (ed. Sixth Edition). Boston: Academic Press. doi: https://doi.org/10.1016/B978-0-12-405935-1.09001-8.

Landon, R.H. (1982). Compendium of unsteady aerodynamic measurement. *AGARD*, Naca 0012 oscillating and transient pitching, data set 3.

Lee, H. M. & Kwon, O. J. (2019). Numerical Simulation of Horizontal Axis Wind Turbines with Vortex Generators. *International Journal of Aeronautical and Space Sciences*, 20(2), 325-334. doi: 10.1007/s42405-018-0118-z.

Li, B., Wu, J. & Liu, Y. (2021). Numerical Study on Subsonic-Supersonic Laval Nozzle Using MacCormack Scheme. *Journal of Physics: Conference Series*, 2012(1), 012096. doi: 10.1088/1742-6596/2012/1/012096.

Li, Y., Zhang, Y. & Bai, J. (2020). Numerical Simulation of the Aerodynamic Influence of Aircrafts During Aerial Refueling with Engine Jet. *International Journal of Aeronautical and Space Sciences*, 21(1), 15-24. doi: 10.1007/s42405-019-00212-2.

Li, Y. (2018). CFD simulation of Smooth and Roureemh NACA 0012 Airfoils at low Reynolds number. doi: 10.11575/PRISM/34960. Publisher: Schulich School of Engineering.

Lindner, G., Devaux, Y. & Miskovic, S. (2020). VortexFitting: A post-processing fluid mechanics tool for vortex identification. *SoftwareX*, 12, 100604. doi: 10.1016/j.softx.2020.100604.

Liu, C., Yan, Y. & Lu, P. (2014). Physics of turbulence generation and sustenance in a boundary layer. *Computers & Fluids*, 102, 353–384.

Liu, C., Gao, Y., Tian, S. & Dong, X. (2018a). Rortex—A new vortex vector definition and vorticity tensor and vector decompositions. *Physics of Fluids*, 30(3), 035103.

Liu, C., Gao, Y., Tian, S. & Dong, X. (2018b). Rortex—A new vortex vector definition and vorticity tensor and vector decompositions. *Physics of Fluids*, 30(3), 035103. doi: 10.1063/1.5023001.

Menter, F. (1994). Two-equation eddy-viscosity turbulence models for engineering applications. *AIAA Journal*, 32(8), 1598-1605. doi: 10.2514/3.12149.

Menter, F., Schütze, J. & Gritskevich, M. (2012). Global vs. zonal approaches in hybrid RANS-LES turbulence modelling. In *Notes on Numerical Fluid Mechanics and Multidisciplinary Design* (vol. 117, pp. 15-28). doi: 10.1007/978-3-642-31818-4_2.

Menter, F., Hüppe, A., Matyushenko, A. & Kolmogorov, D. (2021). An Overview of Hybrid RANS–LES Models Developed for Industrial CFD. *Applied Sciences*, 11(6), 2459. doi: 10.3390/app11062459.

Merabet, R. (2021). *Aerodynamic Simulations of Helicopter Rotors through the Actuator Line Method*. (Ph.D. thesis).

Molina, E., Spode, C., da Silva, R. G. A., Manosalvas-Kjono, D. E., Nimmagadda, S., Economon, T. D., Alonso, J. J. & Righi, M. (2017). Hybrid RANS/LES Calculations in SU2. In *23rd AIAA Computational Fluid Dynamics Conference*. doi: 10.2514/6.2017-4284.

Molina, E., Silva, D. M., Broeren, A. P., Righi, M. & Alonso, J. J. (2019). Application of DDES to Iced Airfoil in Stanford University Unstructured (SU2). *Progress in Hybrid RANS-LES Modelling*.

Molina, E., Silva, D. M., Broeren, A. P., Righi, M. & Alonso, J. J. (2020). Application of DDES to Iced Airfoil in Stanford University Unstructured (SU2). In Hoarau, Y., Peng, S.-H., Schwamborn, D., Revell, A. & Mockett, C. (Eds.), *Progress in Hybrid RANS-LES Modelling* (vol. 143, pp. 283–293). Cham: Springer International Publishing. doi: 10.1007/978-3-030-27607-2_23.

NASACFDVAL2004. (by Christopher Rumsey). NASA Langley Research Center Turbulence Modeling Resource [Webpage]. Retrieved from: https://turbmodels.larc.nasa.gov/nasahump_val.html.

Noelting, S., Wessels, M., Keating, A., Satti, R., Li, Y. & Shock, R. (2008). Lattice Boltzmann Simulations of the Flow Over a Hump with Flow Control. *Collection of Technical Papers - AIAA Applied Aerodynamics Conference*. doi: 10.2514/6.2008-6721.

Oriji, U. & Tucker, P. (2013). Modular Turbulence Modeling Applied to an Engine Intake. *Journal of Turbomachinery*, 136, 051004-051004. doi: 10.1115/1.4025232.

Patel, P. & Zha, G. (2020). Improved Delayed Detached Eddy Simulation of Separated Flow. In *AIAA AVIATION 2020 FORUM*. doi: 10.2514/6.2020-3013.

Peng, S.-H., Deck, S., van der Ven, H., Knopp, T., Catalano, P., Lozano, C., Zwerger, C., Kok, J., Jirasek, A., Capizzano, F. & Breitsamter, C. (2014). AD/AG49: Scrutinizing Hybrid RANS-LES Methods for Aerodynamic Applications. In *Scrutinizing Hybrid RANS-LES Methods*.

Prandtl, L. (1935). The Mechanics of Viscous Fluids. In *Aerodynamic Theory Vol. III, Berlin, J. Springer, edited by W. F. Durand*.

Probst, A., Schwamborn, D., Garbaruk, A., Guseva, E., Shur, M., Strelets, M. & Travin, A. (2017). Evaluation of grey area mitigation tools within zonal and non-zonal RANS-LES approaches in flows with pressure induced separation. *International Journal of Heat and Fluid Flow*, 68, 237–247. doi: https://doi.org/10.1016/j.ijheatfluidflow.2017.08.008.

Raffel, M., Willert, C. E., Scarano, F., Kähler, C. J., Wereley, S. T. & Kompenhans, J. (2017). *Particle image velocimetry: a practical guide (experimental fluid mechanics); 3rd ed*. Springer. doi: 3319688510.

Rafiee, S. E. & Sadeghiazad, M. M. (2016). Experimental study and 3D CFD analysis on the optimization of throttle angle for a convergent vortex tube. *Journal of Marine Science and Application*, 15(4), 388–404. doi: 10.1007/s11804-016-1387-1.

Rafiee, S. E. & Sadeghiazad, M. (2017). Experimental and 3D CFD analysis on optimization of geometrical parameters of parallel vortex tube cyclone separator. *Aerospace Science and Technology*, 63, 110–122. doi: 10.1016/j.ast.2016.12.014.

Reddy, K., Ryon, J. & Durbin, P. (2014). A DDES model with a Smagorinsky-type eddy viscosity formulation and log-layer mismatch correction. *International Journal of Heat and Fluid Flow*, 50, 103 – 113. doi: 10.1016/j.ijheatfluidflow.2014.06.002.

Roache, P. J. (1994). Perspective: A Method for Uniform Reporting of Grid Refinement Studies. *Journal of Fluids Engineering*, 116(3), 405–413. doi: https://doi.org/10.1115/1.2910291.

Rockwood, M., Huang, Y. & Green, M. A. (2018). FLUIDS 3 , 014702 (2018) Tracking coherent structures in massively-separated and turbulent flows.

Roy, C. J. (2003). Grid Convergence Error Analysis for Mixed-Order Numerical Schemes. P. O. Box 5800, MS 0825 Albuquerque, NM 87185-0825.

Rumsey, C. L., Gatski, T. B., Sellers, W. L., Vasta, V. N. & Viken, S. A. (2006). Summary of the 2004 Computational Fluid Dynamics Validation Workshop on Synthetic Jets. *AIAA Journal*, 44(2), 194–207. doi: 10.2514/1.12957.

Rumsey, C. L. (2007). Reynolds-Averaged Navier-Stokes Analysis of Zero Efflux Flow Control over a Hump Model. *Journal of Aircraft*, 44(2), 444–452. doi: 10.2514/1.23514.

Rumsey,C, L. & Gatski, T. B. (2003). Summary of EASM Turbulence Models in CFL3D with Validation Test Cases,. *AIAA Journal*, NASA/TM-2003-212431(81), 1598-1605.

Sadarjoen, I. A. & Post, F. H. (1999). Geometric Methods for Vortex Extraction. *VisSym99: Joint Eurographics - IEEE TCVG Symposium on Visualization*. doi: 10.2312/vissym19991010.

Sainte-Rose, B., Bertier, N., Deck, S. & Dupoirieux, F. (2009). A DES method applied to a Backward Facing Step reactive flow. *Comptes Rendus - Mecanique*, 337(6-7), 340 – 351. doi: 10.1016/j.crme.2009.06.017.

Satheesh Kumar, A., Singh, A. & Thiagarajan, K. B. (2020). Simulation of backward facing step flow using OpenFOAM®. In *AIP Conference Proceedings 10 January 2020; 2204 (1): 030002*. (vol. 2204, pp. 030002). doi: 10.1063/1.5141565.

Schanz, D., Huhn, F., Gesemann, S., Dierksheide, U., Meerendonk, R., Manovski, P. & Schröder, A. (2016, 01). Towards high-resolution 3D flow field measurements at the cubic meter scale. pp. 0.

Seifert, A. & Pack, L. (2002). Active Flow Separation Control on Wall-Mounted Hump at High Reynolds Numbers. *Aiaa Journal - AIAA J*, 40, 1363-1372. doi: 10.2514/2.1796.

Sekhar, S. K., Mansour, N. N. & Caubilla, D. H. (2015). Implicit LES of turbulent, separated flow: wall-mounted hump configuration. In *53rd AIAA Aerospace Sciences Meeting*. doi: 10.2514/6.2015-1966.

Shan, H., Jiang, L., Liu, C., Love, M. & Maines, B. (2008). Numerical study of passive and active flow separation control over a NACA0012 airfoil. *Computers and Fluids*, 37(8), 975 – 992. doi: 10.1016/j.compfluid.2007.10.010.

Shur, M. L., Spalart, P., Strelets, M. K. & Travin, A. K. (2008). A hybrid RANS-LES approach with delayed-DES and wall-modelled LES capabilities. *International Journal of Heat and Fluid Flow*, 29(6), 1638 – 1649. doi: 10.1016/j.ijheatfluidflow.2008.07.001.

Shur, M. L., Spalart, P., Strelets, M. K. & Travin, A. K. (2015). An Enhanced Version of des with Rapid Transition from RANS to les in Separated Flows. *Flow, Turbulence and Combustion*, 95(4), 709 – 737. Retrieved from: http://dx.doi.org/10.1007/s10494-015-9618-0.

Siggeirsson, E. M. & Andersson, N. (2019). The NASA 2D wall-mounted hump simulated using DDES-SA with the G3D::Flow solver. *AIAA Scitech 2019 Forum*. doi: 10.2514/6.2019-0083.

Slotnick, J., Khodadoust, A., Alonso, J., Darmofal, D., Gropp, W., Lurie, E. & Mavriplis, D. (2014). *CFD vision 2030 study: a path to revolutionary computational aerosciences*. Retrieved from: https://ntrs.nasa.gov/citations/20140003093.

Spalart, P. & Allmaras, S. (1992). A one-equation turbulence model for aerodynamic flows. *30th Aerospace Sciences Meeting and Exhibit*. doi: 10.2514/6.1992-439.

Spalart, P. & Allmaras, S. (1994). A one-equation turbulence model for aerodynamic flows. *La Recherche Aérospatiale*. doi: 10.2514/6.1992-439.

Spalart, P., Deck, S., Shur, M. L., Squires, K. D., Strelets, M. K. & Travin, A. (2006). A New Version of Detached-eddy Simulation, Resistant to Ambiguous Grid Densities. *Theoretical and Computational Fluid Dynamics*, 20(3), 181–195. doi: 10.1007/s00162-006-0015-0.

Spalart, P., Jou, W.-H., Strelets, M. & Allmaras, S. (1997a). Comments on the Feasibility of LES for Wings, and on a Hybrid RANS/LES Approach.

Spalart, P., Jou, W., Strelets, M. & Allmaras, S. (1997b). Comments on the feasibility of LES for wings, and on a hybrid RANS/LES approach. 1st AFOSR Int. *Symp. Eng. Turb. Modelling and Measurements, May*, pp. 24–26.

Spalart,P. Venkatakrishnan, V. (2016). On the role and challenges of CFD in the aerospace industry. *The Aeronautical Journal*, 120(1223), 209–232. doi: 10.1017/aer.2015.10.

SU2-Publications. (by SU2 Group). SU2 Publications [Webpage]. Retrieved from: https://su2code.github.io/publications.html#.

Szymkiewicz, R. (2010). *Numerical Modeling in Open Channel Hydraulics*. Springer Netherlands. Retrieved from: https://books.google.ca/books?id=0mcm3woaVPwC.

Tagawa, G. B., Huck, V., Morency, F. & Beaugendre, H. (2019). Shear-Layer Adapted DDES Analysis of 3D Stalled Flow Over an Iced Airfoil. In *AIAA Aviation 2019 Forum*. doi: 10.2514/6.2019-3308.

Tian, S., Gao, Y., Dong, X. & Liu, C. (2018). Definitions of vortex vector and vortex. *Journal of Fluid Mechanics*, 849, 312–339. doi: 10.1017/jfm.2018.406.

Toro. E. F. (1999). *Riemann solvers and numerical methods for fluid dynamics : a practical introduction.* (ed. Springer-Verlag, Berlin, Allemagne, 2nd edition, 1999.).

Tsoutsanis, P. (2018). Extended bounds limiter for high-order finite-volume schemes on unstructured meshes. *Journal of Computational Physics*, 362, 69–94. doi: 10.1016/j.jcp.2018.02.009.

Uzun, A. & Malik, M. R. (2017). Wall-Resolved Large-Eddy Simulation of Flow Separation Over NASA Wall-Mounted Hump. *55th AIAA Aerospace Sciences Meeting*. doi: 10.2514/6.2017-0538.

Venkatakrishnan, V. (1993). On the accuracy of limiters and convergence to steady state solutions. In *31st Aerospace Sciences Meeting*. doi: 10.2514/6.1993-880.

Wang, F., Gao, A., Wu, S., Zhu, S., Dai, J. & Liao, Q. (2019). Experimental Investigation of Coherent Vortex Structures in a Backward-Facing Step Flow. *Water*, 11(12). doi: 10.3390/w11122629.

Wang, J., Guo, L., Wang, Y., Deng, L., Wang, F. & Li, T. (2020). A Vortex Identification Method Based on Extreme Learning Machine. *International Journal of Aerospace Engineering*, 2020, 8865001. doi: 10.1155/2020/8865001. Publisher: Hindawi.

Wang, Y., Vita, G., Fraga, B., Wang, J. & Hemida, H. (2021). Effect of the Inlet Boundary Conditions on the Flow over Complex Terrain Using Large Eddy Simulation. *Designs*, 5(2), 34. doi: 10.3390/designs5020034.

Yang, Y. & Zha, G. (2016). Simulation of airfoil stall flows using IDDES with high order schemes. doi: 10.2514/6.2016-3185.

Yeshala, N., Min, B.-Y. & Sankar, L. (2008). Drag Reduction Studies Using Active Flow Control. *4th Flow Control Conference*. doi: 10.2514/6.2008-3870.

You, D., Wang, M. & Moin, P. (2006). Large-Eddy Simulation of Flow over a Wall-Mounted Hump with Separation Control. *AIAA Journal*, 44(11), 2571-2577. doi: 10.2514/1.21989.

Yu, Y., Shrestha, P., Alvarez, O., Nottage, C. & Liu, C. (2020). Correlation Analysis among Vorticity, Q method and Liutex [arXiv]. *arXiv*, 13 pp. -. Liutex;correlation analysis;vorticity-based method;vorticity theory;vortex identification method;third-generation method;Lambda-2 methods;.

Zhou, J., Adrian, R. J., Balachandar, S. & Kendall, T. M. (1999). Mechanisms for generating coherent packets of hairpin vortices in channel flow. *Journal of Fluid Mechanics*, 387, 353–396. doi: 10.1017/S002211209900467X.

Šarić, S., Jakirlić, S., Djugum, A. & Tropea, C. (2006). Computational analysis of locally forced flow over a wall-mounted hump at high-Re number. *International Journal of Heat and Fluid Flow*, 27(4), 707–720. doi: 10.1016/j.ijheatfluidflow.2006.02.015.